SELECTED STUDIES OF CELESTIAL DYNAMICS AND HABITABILITY OF EXTRA SOLAR PLANETARY SYSTEMS

by

BILLY LEE QUARLES

Presented to the Faculty of the Graduate School of
The University of Texas at Arlington in Partial Fulfillment
of the Requirements
for the Degree of

DOCTOR OF PHILOSOPHY

THE UNIVERSITY OF TEXAS AT ARLINGTON

August 2012

To my children, Jacob and Eden, and my wife, Teresa.

ACKNOWLEDGEMENTS

I would like to thank my (co)advising professors Dr. Zdzislaw Musielak and Dr. Manfred Cuntz for their guidance and advice through the course of my Ph.D. graduate studies. I wish to thank Dr. Sangwook Park, Dr. Yue Deng, and Dr. Alex Weiss for their interest in my research and for taking time to serve in my committee.

I would also like to express my deep gratitude to my parents, Rick and Yvonne Quarles who gave me the motivation and freedom to pursue my own course. I would like to thank my siblings, James Quarles and Patricia Chawla, for setting an example for me so that I would be able to stand on the shoulders of giants. I am also grateful to my wife, Teresa, for her encouragement and patience especially during the dissertation writing process.

Finally, I thank Jason Eberle and Suman Satyal for their support in coding including "Hello World." I would like to acknowledge the honor I have received in the philosophical insight from Kapil Adhikari and Shree Bhattarai through our many "tea time" conversations. I want to acknowledge all of my friends and acquaintances that I have known throughout my graduate education.

I am grateful to acknowledge that this dissertation is based upon work supported by the U.S. Department of Education GAANN Grant No. P200A090284.

Imagination will often carry us to worlds that never were. But without it we go nowhere. –**Carl Sagan**

July 17, 2012

ABSTRACT

SELECTED STUDIES OF CELESTIAL DYNAMICS AND HABITABILITY OF EXTRA SOLAR PLANETARY SYSTEMS

BILLY LEE QUARLES, Ph.D.

The University of Texas at Arlington, 2012

Supervising Professor: Zdzislaw Musielak

Planetary science in various forms has become interwoven into human culture during all of known human history. The need and desire to expand our horizons has brought humans from basic forms of observation to the development of space satellites that have (in)directly observed other worlds. A major feat of this enterprise during the last half century has been the development of numerical tools and theories to determine the orbital stability of multiple objects orbiting a central body.

In this dissertation I have examined two special cases of the gravitational N body problem (N = 3,4) along with the development of a stability criterion based upon the method of Lyapunov exponents. This Lyapunov criterion has shown the existence of a resonance plateau and instability islands within the coplanar circular restricted three body problem (CRTBP). Additionally, the Lyapunov criterion has been used in the determination of resonances for the case of large mass ratios in the CRTBP. I have demonstrated that the 2:1 resonance occurs most frequently as a primary resonance and 3:1 as a secondary resonance within the framework of the coplanar CRTBP.

My established methods of using the Lyapunov criterion and determination of resonances have been used to address a controversial system ν Octantis to ascertain possible ranges of stability that would account for the present observations of a Jupiter-mass planet. The determined stability limits of the planet in ν Octantis has unveiled the evidence supporting the possibility of a retrograde planet existing in the binary star system and demonstrated the desert of stability when considering a traditional prograde planet.

Orbital stability is but one part in the bigger question of habitability. To this end, I have addressed the concerns of habitability within the newly discovered circumbinary system Kepler-16 for possible habitable planets and moons. This exploration has considered many different orbital, formation, and habitability scenarios for which a habitable world could exist. I have shown that an Earth-mass object could exist as a Trojan or an exomoon within the standard habitable zone. Furthermore, the orbital stability region resumes for planetary orbits superior to 0.95 AU from Kepler-16A which resides in the extended habitable zone. Finally, the habitability of possible Trojan planets and exomoons in HD 23079 has been addressed and I have shown the improbability of an exomoon from taking excursions from the habitable zone as well as a stable orbit for such an object.

My future work will better investigate the possibility of habitable moons in HD 23079. This work will aid in broadening the regions to be considered as habitable since such objects would orbit a Jupiter-like planet within the habitable zone. In addition, I plan to develop theoretical tools to investigate the regions of habitability within multi-stellar environments. I plan to use this new framework to further the investigation of circumbinary planets in Kepler-16, Kepler-34, Kepler-35, and Kepler-38. Data from the Kepler mission will soon be made public and I will search the public data for the existence of habitable objects within these systems.

TABLE OF CONTENTS

LIST OF FIGURES

LIST OF TABLES

CHAPTER 1

INTRODUCTION

1.1 Ancient Planetary Astronomy

Early in human history the search for other places to explore was ever present. Ancient tribes were ill-contented with the constant landscape of Africa which prompted migrations to Asia and eventually Europe. The same has been true when man has looked to the heavens. The desire for exploration and understanding is overwhelming and existing to this day. Many civilizations have looked to find places similar to their previous home for many reasons, such as general expansion of land, resources, technology, and knowledge.

The first recorded history that has survived comes from the ancient Sumerians. These people made many advances in the field of planetary astronomy. The first of which concerned the so-called "planet" that we call today the Moon. Using the Moon, the Sumerians devised a calendar of 12 months consisting of 30 days to give a year length of 360 days. This calendar proved useful for only a few years before the errors in calculation (ie., the lack of 5.2455 days) caused problems in the harvesting, planting, and storing of crops. The lunar calendar persists in many cultures derived from Sumeria which requires constant revision to correct for such errors (Aughton 2008).

Another "planet" became as important as the Moon and this is what we call the Sun. Ancient Egyptians revered this second "planet" and gave it a special place in their own mythology. These two "planets" were in constant conflict with each other as the Sun dominated in the summer and the Moon pushed back to gain the advantage

in the winter. This conflict was necessary for ancient Egyptians to devise their own interpretation of the calendar. They too devised a 12 month calendar that would give 360 days, but after seeing that extra days were required in specific intervals, 5 feast days were added at the end of each year to fill the gap (Aughton 2008). This produced a more accurate calendar to commemorate the epic battle between the planets and result in more predictability in the cycles of the Nile, the source of ancient Egyptian life.

This type of calendar was used in various civilizations for over 3000 years and seeded the culture of determining the movement of the celestial bodies. This knowledge was extremely important in allowing humans to make use of the land and establish the necessary leisure time to observe more of the heavens.

Most of the Western history stems from the ancient Greeks who provided a preliminary definition of "planet" or "wanderer." The Greeks categorized the 7 known planets (including the Sun and Moon as planets) and integrated them farther into the culture than just the planting of crops. The position of the planets were extremely important for the common Greek as well as the ruling class. By the position of the planets Greeks engaged in agriculture, fought wars, built monuments, and made everyday decisions based on the perceived influence of the planets.

The ancient Greeks had observed the motions of the planets long enough to determine the planets displayed some irregular (retrograde) motions. It became the work of Ptolemy of Alexandria to correct for these peculiar motions of the planets similarly to how the calendar had been corrected. Following from the cosmology of Aristotle, Ptolemy (147) was forced to construct the seemingly simple epicycles which consisted of circles upon circles orbiting the Earth (See Figure 1.1). However these simple corrections soon became a major burden for the astrologers who needed the

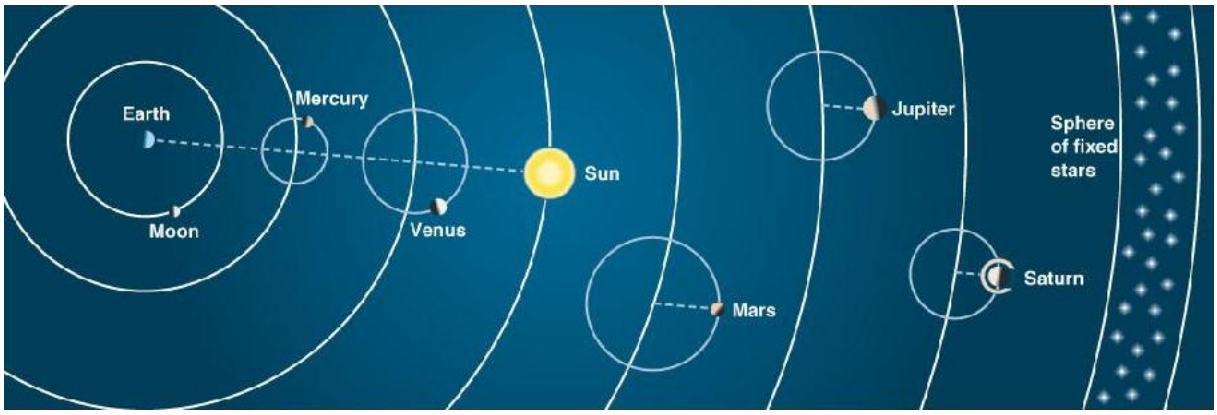

Figure 1.1. Ptolemaic model of the known celestial bodies using epicycles. Image Credit: University of California.

precise planetary locations. The incorrect geocentric view of planetary motion lasted over a millennium due to the inability to disprove the Ptolemaic model.

The study of planetary motion was not limited to Europe. Other civilizations looked to the heavens for guidance from the planets for their own astrologies. Most notably, the Indian astronomer Aryabhata in 500 AD developed ideas concerning a heliocentric model, planets orbiting in ellipses rather than circles, and the periods of the planets in terms of the radius of their orbits. However due to societal restrictions this knowledge was never dispersed among the population thus restricted from flowing to the rest of the ancient world.

In other parts of the world the necessity of knowing the precise locations of planets had become even more commonplace. The Maya who lived in pre-Columbian Central America have shown to have a great knowledge of the planets and were able to compute the locations very precisely. The Maya would use texts similar to a farmers' almanac to determine the amount of luck that the planets would provide in particular years for the purposes of agriculture (North 1995).

1.2 Medieval Planetary Astronomy

Through the Middle Ages planetary astronomy existed only in the domain of the astrologers. Meticulous records were kept only for "predictions" of fortune for the ruling class. Not surprisingly these predictions were now consistent among each other as the penalty for bad news was most assuredly execution. Astrologers were somewhat content with the complicated techniques accounting for epicycles because it almost guaranteed a longer life due to the skills required. However during the beginning of the 16^{th} century AD, a Polish astronomer named Nicolaus Copernicus provided the proof needed to solidify the Heliocentric theory. Copernicus' revolution came as his work has shown that the phenomena of the epicycles could be dismissed if the Sun was chosen to reside at the center of the planet's orbits (See Figure 1.2). It was shown that the inner planets would orbit more quickly than the outer planets and the changing perspective from Earth would make the orbit of Mars only appear to change direction. This concept that the Earth was just an ordinary planet among the other planets became the Copernican principle which will later guide future observations and exploration of objects outside the Earth.

Following Copernicus in the 17^{th} century AD, a German mathematician would follow up on the Copernican revolution. Johannes Kepler would use the observations of a Danish nobleman, Tycho Brahe, to show that the orbits of the planets were not perfect circles. This discovery began the metamorphosis of the Greek/Roman philosophy that the heavens were perfect to a new philosophy rooted in mathematics that sought to better describe the motion of the planets. Most notably, Kepler formulated 3 laws of planetary motion which defined planetary orbits as ellipses, areal velocity is constant, and the periods of the planets could be determined in terms of the radius of their orbits. Although Kepler made this discovery over a millennium after Aryabhata, his work is most known and recognized because of the academic environment of the

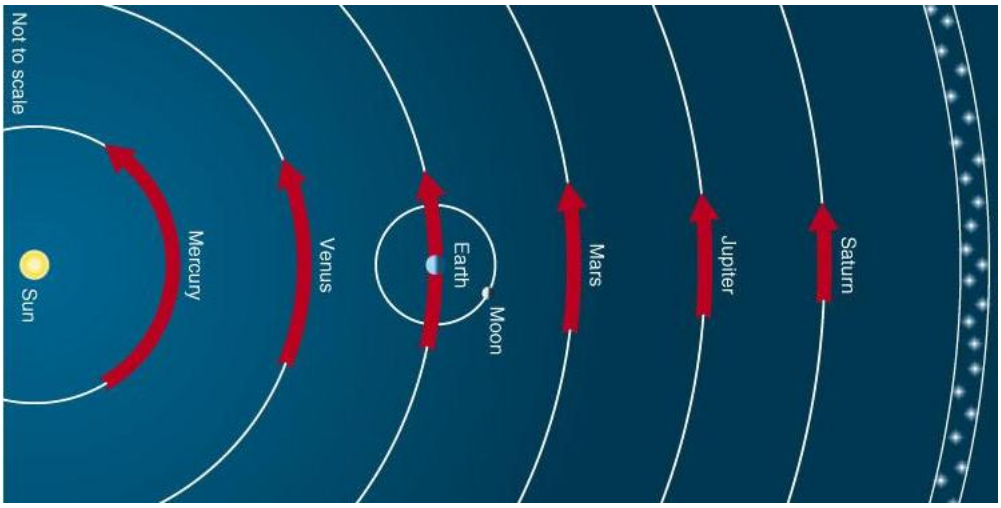

Figure 1.2. Copernican model of the known celestial bodies. Image Credit: University of California.

Renaissance in Europe. This philosophy of knowledge sharing allowed the scientific revolution to grow and become enriched with an ever growing volume of knowledge.

During the same period as Kepler, an Italian astronomer named Galileo Galilei utilized a modern tool to better observe the motions of the planets. He took advantage of an optical instrument called the telescope, which had been developed independently by Hans Lippershey, Zacharias Janssen, and Jacob Metius a year earlier in 1608 (King 1955). Galileo improved upon the design and used the telescope to view many celestial objects with unmatched precision at the time. Galileo demonstrated that other planets could harbor moons and furthered the notion that the Earth's moon was not particularly special. The observation of moons orbiting Jupiter really gave the proof that geocentric astronomers needed to adopt the heliocentric theory. Following Galileo, a British physicist and astronomer sought to explain why the planets move. Sir Isaac Newton developed a theory of science called physics that sought to describe further the motion of the heavenly bodies. This formulation provided a better defined mathematical framework to determine the motion of the planets. Even though

Newton's Law of Universal Gravitation was immensely successful in describing the motion of the planets, problems remained in determining the motion of the Moon through Newton's newly developed mathematical tools. The 3 body problem was one of the many things which Newton spent the rest of his life trying to solve.

On March 13 1781, Sir William Herschel used the telescope to observer an object which many had previously noted as a star, comet, or simply a nebulous object. Herschel believed that he had discovered a comet but could not confirm this hypothesis as he could not resolve a coma or tail for the object. Herschel and others also determined the eccentricity of the orbit using the previously developed laws of Kepler and Newton. The theory determined that the orbit of this unknown object was nearly circular which was peculiar because comets generally have highly eccentric orbits. By 1783, Herschel had made numerous observations, calculations, and discussions with contemporaries before declaring the object a planet that was later named Uranus after the ancient Greek deity of the sky. The importance of Herschel's discovery shows the drive for mankind to explore and understand the Solar System using the tools of physics and mathematics. Prior to Herschel's discovery, Johann Elert Bode had determined a mathematical relationship comparing the indexing of the planets with their semi major axis. This series was later called the Titius-Bode Law. Even though it has been named a physical law, its connection to physics, if any, remains unknown and is widely considered to be a mathematical coincidence.

However the search for more planets in the Solar System continued. The orbits of the known planets were calculated with a high level of accuracy for the time period but irregular changes in the orbit of Uranus prompted further investigation. Mathematicians who specialized in celestial mechanics began trying to solve the riddle of the perturbations by introducing another planet outside the orbit of Uranus. John Couch Adams and Urbain Le Verrier independently took this idea to make a predic-

tion to where this unobserved planet would be to cause the correct perturbations. Then on September 23 1846, Johann Galle made the first observation of the proposed planet within a *degree* of the predicted location which would be later called Neptune after the ancient Roman deity of the sea. This demonstrated the first mathematical determination of a planet by indirect observations of the motion of its neighbor.

1.3 Modern Planetary Astronomy

Shortly after the discovery of Neptune the search for planets extended to the realm of other stars. This idea came from the application of Newton's laws of motion and universal gravitation. The first attempted detection method of extra solar planets (exoplanets) was that of astrometry. The technique of astrometry had been used to detect unseen companion stars in binary star systems. The observed star will experience a force due to the gravity of the unseen companion. So if the proper motion or the motion projected onto the plane of the sky can be measured accurately, then the existence of the unseen companion can be inferred. Figure 1.3 demonstrates how the method of astrometry is performed in observational technique and data.

Captain W.S. Jacob of the East India Company at Madras' Observatory made observations of binary star 70 Ophiuchi using the technique of astrometry. In 1855 he reported that the orbital anomalies made it 'highly probable' that a unseen planetary body existed in the system (Jacob 1855). Also, in the 1890s Thomas J.J. See of the University of Chicago and the United States Naval Observatory determined that a planet should exist with a 36-year period in the 70 Ophiuchi system (See 1896). However both of these observations were met with both skepticism and scrutiny. It remained for the claims to be proven either by theory or by observations using an independent detection method. At the time other detection methods were either

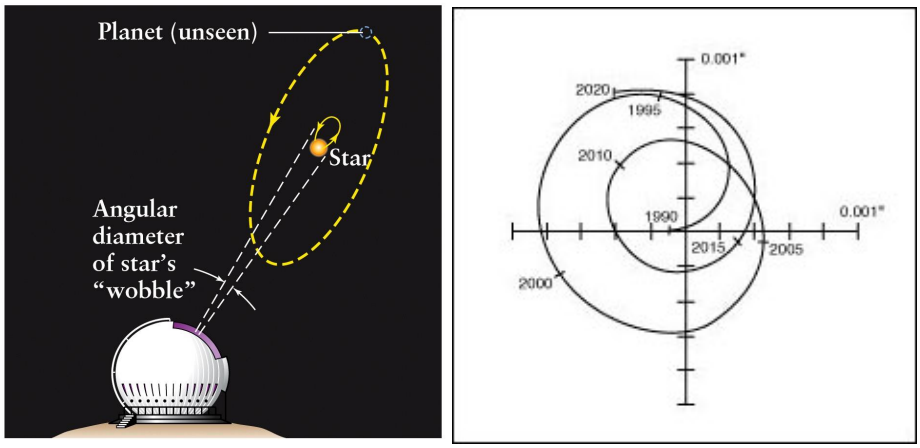

(a) (b)

Figure 1.3. Examples of the method of astrometry. (a) Image Credit: Rich Townsend. (b) Image Credit: NASA JPL.

undeveloped or nonexistent. So the theory was left to prove the credibility of these claims.

Forest Ray Moulton of University of Chicago performed calculations using the framework of the 3-body problem. He determined that the proposed planet would be unstable with the observed system parameters of See (Sherrill 1999). However, despite being discredited, the method of astrometry was still not fully rejected, and in the 1960s Peter van de Kamp made a claim of planets orbiting Barnard's star (van de Kamp 1969), but this claim was also proved to be erroneous. The technological capability was not present with these previous observations and the multiple techniques required to account for systematic errors were not yet developed. It is widely considered that all claims of exoplanets to be erroneous prior to the contemporary age of exoplanet detection.

The first exoplanet detection to come with subsequent confirmation was made by a group of Canadian astronomers in 1988 which consisted of Bruce Campbell, G. A. H. Walker, and Stephenson Yang (CWY88). This group used a different technique

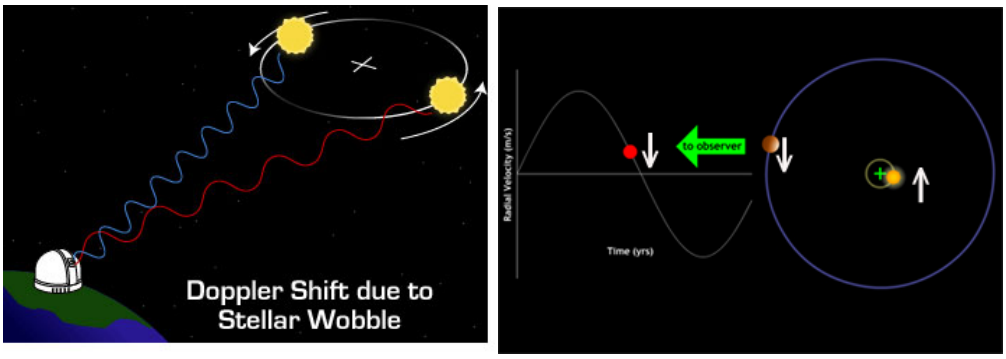

(a) (b)

Figure 1.4. Examples of the Doppler method. (a) Image Credit: NASA JPL. (b) Image Credit: University of Nebraska-Lincoln.

than previous planet-hunters. Using the same idea of reflex motion CWY88 used the spectral lines of the star γ Cephei to determine the radial velocity of the host star and the unseen planetary companion (Campbell et al. 1988). This technique is called the Doppler method because it relies on the Doppler effect to produce changes in the host star's spectrum due to the movement of the source. Figure 1.4 demonstrates how the Doppler method is used to produce a measure of the unseen companion's radial velocity.

After the discovery by CWY88, astronomers remained skeptical about its validity. The large number of erroneous claims from the past had already tainted the pool of confidence in the result. Several years later there would be a revival of the Doppler method due to technological advancements. In the mean time the first confirmed detection of any exoplanets existed around an unlikely source, the millisecond pulsar PSR1257 + 12. The two exoplanets were discovered using a variation of the Doppler method for usage with pulsars (Wolszczan & Frail 1992). The regularity of pulses coming from the object provided a way for measuring the reflex motion of the pulsar due to the gravitational influence of the unseen planets. However, planetary scientists

really desired to find exoplanets around Sun-like stars and the previous observations by CWY88 were on the fringe of instrumental detectability. So by October 6, 1995 technology had advanced enough for the first definitive exoplanet detection orbiting a main-sequence star to be made by Michel Mayor and Didier Queloz of the University of Geneva. Mayor and Queloz observed a Jupiter-like planet orbiting the G-type star 51 Pegasi with a minimum mass of 0.47 M_J and a period of $\sim$ 4.23 days (Mayor & Queloz 1995). This was an astonishing discovery and was confirmed independently by Geoffrey Marcy and Paul Butler on October 12, 1995. The new era of exoplanets and planet hunting had begun.

Several years passed and more "Hot Jupiters" were being discovered with the Doppler method. However the detections only contained single Jupiter-like exoplanets. Our Solar System has 8 planets and the question to ask was "Are there multiple planet systems?" In 1999 Jack J. Lissauer answered this question with observations of υ Andromadae A (Lissauer 1999). He demonstrated that the system contained 3 exoplanets with a 4^{th} being discovered in 2011 (Curiel et al. 2011).

At this time, the Doppler method had proved to be a viable detection method. However, this method has its limitations. The foremost that it gives information relating to only 1 degree of freedom (ie., motion towards and away from the observer). Due to this limitation only the minimum mass or $M \sin i$ can be determined. An alternate detection method was needed to overcome this limit. As a graduate student, David Charbonneau used a technique that was previously developed for eclipsing binary stars. The transit method uses the principle that a planet can produce changes in the light output of its host star through eclipses. These changes are proportional to the size of the planet and a Jupiter-sized planet can potentially block 1% of the light from the star. By making use of previous techniques for binary stars, the inclination can be determined to give the true mass of the planet and the radius of the planet

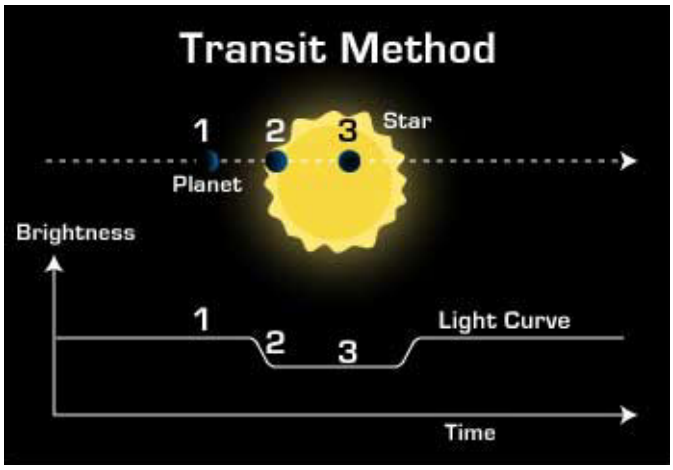

Figure 1.5. Example of the Transit method.

up to the uncertainty of the stellar radius (Charbonneau et al. 2000). Figure 1.5 illustrates how the brightness of a star will change due to a planet eclipsing it.

The Transit method has its own limitations as well. There can be a high occurrence of false positives due to transient phenomena such as starspots, other stellar variability, background stars, and foreground dust clouds. In order to account for the known sources of false positives 3 transits are required to confirm detection. Independent measurements using the Doppler method are highly encourage to increase the robustness of the proposed detected exoplanet. At the writing of this dissertation (April 2012) 763 exoplanets have been confirmed and the rate of detections appear to be exponentially increasing (See Figure 1.6a) with increasing sensitivity due to technological advancements. Also there is a bias towards exoplanets with low eccentricity (Figure 1.6b) which makes models like the circular restricted 3 body problem particularly useful in analyzing such systems.

The Doppler and Transit methods have shown to be the strongest tools for the planet hunter. There are additional methods which include microlensing, pulsar timing, nulling interferometry, and direct imaging. Thus far the detected planets de-

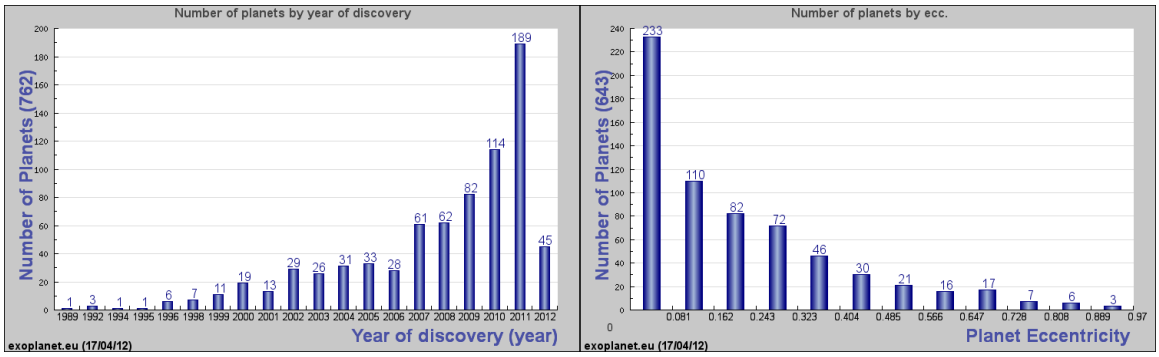

(a) (b)

Figure 1.6. Distribution of planets detected using all available methods. (a) Distribution of planets by year. (b) Distribution of planets by eccentricity.

scribed have been observed from ground-based observations which inherently presents a resolution barrier. This barrier is caused by chaotic turbulence in the Earth's atmosphere also known as "seeing." Although technology in adaptive optics has advanced in the past decade the best resolution measurements and observations come from space-based observatories. On March 7, 2009, the National Aeronautics and Space Administration (NASA) launched a space telescope named Kepler. This telescope utilizes the transit method of detecting planets and exists in an Earth-trailing orbit. The mission lifetime of the telescope was 3.5 years while at the time of writing this thesis has been extended to 7 years. Before Kepler most space based observations of exoplanets were made using the Spitzer space telescope which utilized the Doppler method. Since the coolant on Spitzer was depleted when Kepler was launched, Kepler has become the flagship observatory for exoplanet detections, as well as stellar atmosphere observations. Detections made by the Kepler telescope have motivated much of the work in this thesis. As of June 2012, Kepler has detected 2,231 exoplanetary candidates where 61 have been confirmed by independent observations.

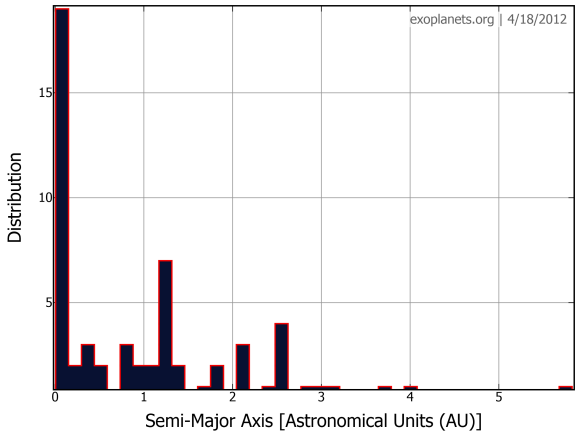

Figure 1.7. Distribution of planets detected existing in binary star systems with respect to the planetary semimajor axis.

1.3.1 Exoplanets in Binary Systems

Detections of exoplanets in binary systems have been elusive and commonplace. The elusive component has been observing binary systems with planets in every configuration possible that can be shown through a theory called the restricted 3 body problem. The detection by CWY88 was made in a binary star system called γ Cephei which is only 45 light years (ly) away. Many other binary systems have been discovered with planets including 55 Cancri and others. Prior to observations made with Kepler, most planets discovered in binaries existed within 5 astronomical units (AU) from the host star and the binary stars were separated by 100s of AU. However, some observations have been made where the binary stars are separated only by 20 and 25 AU (Patience et al. 2002; Eggenberger et al. 2004). Additional theoretical simulations were also performed to suggest that planets could exist within relatively close binary systems (Kley et al. 2001; Quintana et al. 2002, and others). Different planetary formation scenarios are possible based on the binary separation (Figure 1.8) which eluded to the possibility of circumbinary exoplanets.

Only recently observations have shown the existence of circumbinary planets. The Kepler space telescope has shown 3 such systems Kepler-16, Kepler-34, and Kepler-35 (Doyle et al. 2011; Welsh et al. 2012). All of which contain a Saturnian planet with 2 (Kepler-16 & Kepler-35) orbiting their respective binary with near circular orbits. The total number of detections irrespective of binary separation is significant (Figure 1.7) and is expected to grow as Kepler has observed 2,165 eclipsing binary stars. These detections demonstrate in part the motivation of this dissertation to describe the orbits and evaluate the possibility of habitability in these more interesting systems.

1.4 Planetary Orbital Stability

Observations of exoplanets in multiple configurations has brought a renaissance of research to study the dynamics of the restricted 3 body problem. This topic of inquiry was most notably introduced by Sir Isaac Newton in his quest to complete his theory concerning gravitation and the motion of celestial bodies. Newton was able to apply his theory to the major planets of the era but his theory produced inconsistent results when applied to the motion of the Moon. Newton lacked the mathematics and technological requirement of a modern computer to perform the calculations. This problem can be generalized to the "N body problem" where N can be large. This is often performed in the modern era to describe the galactic motion of stars and has been accomplished somewhat successfully (Barnes & Hut 1986; Wisdom & Holman 1992; Aarseth 2003). N body investigators took advantage of the technique of symplectic mapping and hierarchal integration.

One would assume that with the rigorousness that the 2 body problem was solved adding one extra mass would not be very difficult. However in the early 19^{th} century King Oscar II established a prize for solving the N body problem which was

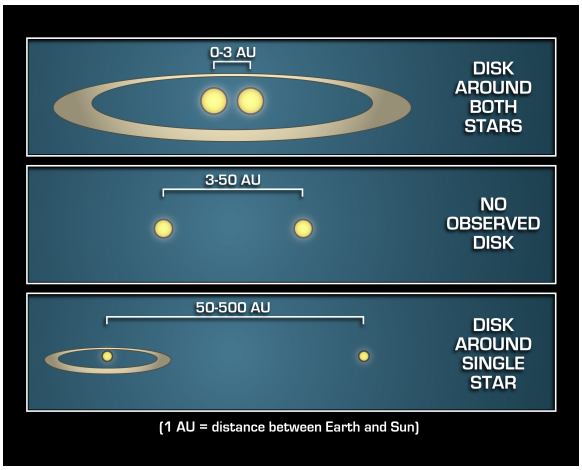

Figure 1.8. Different regimes of planetary formation in binary star systems.

awarded to Henri Poincaré, who actually did not solved the problem and ironically his solution had even an error (Diacu 1996). An infinite series solution was determined for the case of N= 3 by Karl Sundman in 1912, but this series solution converges very slowly. As a result of these analytical shortcomings several approximations were made to simplify the problem.

The assumptions that are relevant to this work are the following:

1. The masses are constant in time with 2 masses (M1,M2) dominating in magnitude over all other masses so that the much smaller masses do not affect the motion of the dominant masses. All other masses will be denoted in decreasing order (ie., M3, M4, . . .).
2. The velocity of all the masses are small enough such that all motions will be considered non-relativistic.
3. The motion of the 2 largest masses (M1,M2) will be a solution to the 2 body problem.
4. The motion of the smaller masses are coplanar with respect to the plane of the 2 largest masses (M1,M2).

The first 3 assumptions limit the discussion to the restricted N body problem. The last assumption limits the discussion to the plane of the binary. The general N body problem in 3 dimensions would be more robust but a strategic decision was made to limit the domain of study due to time and memory constraints, as well as the existence of previous study (Schwarz et al. 2004; Funk et al. 2009, and others). The motion of the 2 main bodies will be considered to be either elliptical or circular as the other cases (ie., hyperbolic and parabolic) do not produce periodic orbits. The mass regimes will be classified in terms of a comparable Solar System body such that stars will be measured in Solar masses ($M_{\odot}$), giant planets will be measured in Jupiter masses (M_J), and terrestrial planets(moons) will be measured in Earth masses ($M_{\oplus}$).

The primary question is what initial conditions in terms of mass, position, velocity, and eccentricity will produce stable, periodic orbits for a proposed planet or moon. A range of stellar masses, planetary(lunar) starting positions, and eccentricities will be considered to address this question in a very general manner.

1.5 Projects

The parameter space to address the N body problem can be quite large and due to time constraints. So the study of the N body problem has been confined to the cases where N = 3 or N = 4. It has also been divided into 3 separate sub-problems. The first problem involves the study of the circular restricted 3 body problem and determining a stability criterion utilizing chaos theory. The second problem uses the determined criterion from the first problem to characterize the possible stability in the system of ν Octantis. Finally, the third problem will use the established criterion to characterize stability of potential and existing objects within the systems of Kepler-16 and HD 23079. The theory pertaining to these sub-problems will be detailed in Chapter 2. The results of the first two problems will be presented and analyzed in

Chapters 3,4, and 5. Then the results concerning habitability will be presented and analyzed in Chapters 6 and 7. Chapter 8 will interpret the results of the various sub-problems and provide an outline of future endeavors.

CHAPTER 2

THEORY

The simplest case of the general N body problem is when N = 2. This is the well known 2 body problem for which analytic solutions are known (Szebehely 1967; Murray & Dermott 1999). These two textbooks will be used here to establish definitions, notations and conventions adopted in this dissertation. In this chapter, basic definitions in three subject areas of theory: celestial mechanics, chaos, and habitable zones will be outlined.

2.1 Celestial Mechanics

2.1.1 Coordinate Systems

The first step in approaching the N body problem is through a choice of coordinate system. In dealing with orbital motion there are only a few free choices. The most common choices fall within two types of coordinate systems, barycentric or astrocentric (Jacobi). The former describes a coordinate system where the center of mass remains fixed and the N bodies are allowed to orbit the center of mass in accordance with Newton's law of universal gravitation. Whereas the latter option allows one to choose the most massive body to remain fixed and motionless. This choice can simplify some problems by reducing the situation to a N-1 body problem.

Considering these choices of coordinate systems this dissertation will focus mainly upon barycentric coordinates unless otherwise noted. However when the number of bodies N is greater than 2, there does exist another choice of coordinates. There can be a sidereal (inertial) or synodic (rotating) coordinate systems (see Figure 2.1.

The usage of each of these coordinate systems varies by application and it will be noted which of these conventions are being used. Sidereal coordinates and barycentric coordinates are interchangeable in there usage as they equally describe the same geometry. Synodic coordinates will be used mainly in application to the circular N body problem where N = 3 and will be denoted with a superscript * symbol (ie., x^*, y^*, z^*).

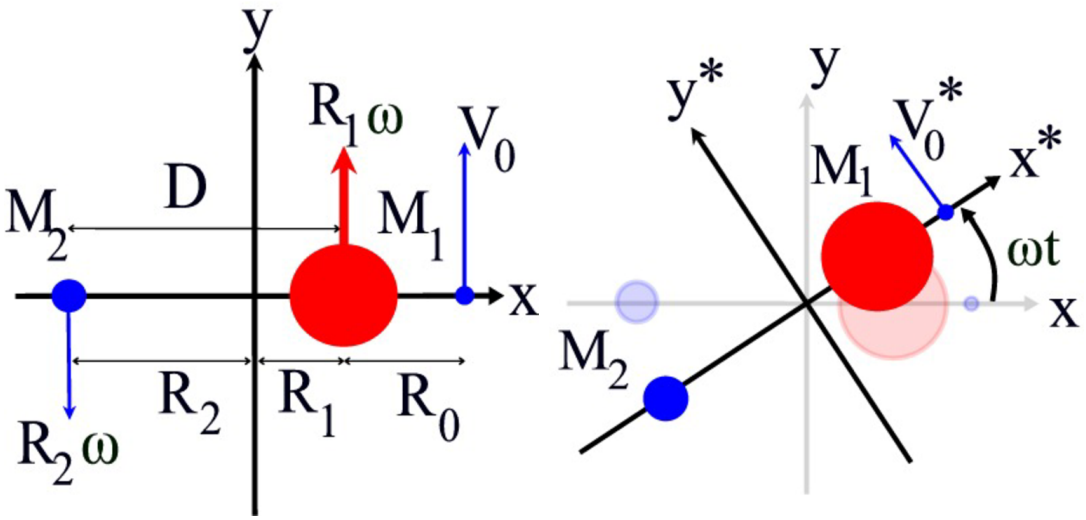

Figure 2.1. Basic setup for the circular restricted three body problem. (a) Initial configuration in sidereal coordinates. (b) Initial configuration in synodic coordinates. All used symbols are described in the main text. Image Credit: Jason Eberle (2010).

2.1.2 Basic Definitions

The massive bodies will be denoted by M_i where the index i will describe the hierarchy of mass with $i = 1$ being the most massive. In the description of the N body problem the total mass of the system will be denoted as M where $M = M_1 + M_2 + \ldots + M_N$. Using this convention mass ratio can thus be defined. Mass

ratio definitions vary between different authors where this dissertation will denote the mass ratio, μ, to correspond with M_2 in the numerator, $\mu = M_2/M$ and the complementary mass ratio, α, to correspond with M_1 in the numerator, $\alpha = M_1/M$. It is assumed in this dissertation that all masses from M_3 to M_N will be sufficiently small so that a relationship can be formed where $\mu + \alpha = 1$. It is important to note that these mass ratios are dimensionless, so that they can be used in equations in place of coordinates requiring the physical coordinates are normalized to also become dimensionless.

Figure 2.1 illustrates the two possible coordinate systems for the circular restricted three-body problem. A barycentric coordinate system is used such that the two most massive bodies can be located by R_1 and R_2 relative to the center of mass (origin). The parameter R_0 locates the smaller mass, M_3, relative to the larger mass, M_1. Since this example is for the circular problem the most massive bodies will orbit in circles with a speed $V_{1,2} = R_{1,2}\omega$ where ω denotes the mean motion (see below).

Normalized units are often used in orbital mechanics to simplify the notation. The following set of equations will demonstrate how a set of Cartesian coordinates can be normalized relative to the initial separation distance, D, between the masses and the orbital velocity in the case of negligible eccentricity with the mean motion $\omega^2 = \frac{GM}{a^3}$ where G, a denote the constant of universal gravitation and semimajor axis between the largest masses (M_1, M_2), respectively, as given by

$$\begin{aligned} \xi &= \frac{x}{D} \quad \eta = \frac{y}{D} \quad \zeta = \frac{z}{D}, \\ \dot{\xi} &= \frac{\dot{x}}{D\omega} \quad \dot{\eta} = \frac{\dot{y}}{D\omega} \quad \dot{\zeta} = \frac{\dot{z}}{D\omega}. \end{aligned} \tag{2.1}$$

The dot (•) notation has been used to denote the derivative with respect to time in Equation 2.1. Additional normalization is required to scale the orbital period, T. This dissertation will adhere to the 2 most common choices. Both choices involve redefining the value of the constant of universal gravitation, G. The first choice will define $G = 4\pi^2$ because this inherently simplifies Newton's definition of Kepler's Third Law (ie., $T^2 = \frac{4\pi^2}{GM}a^3$), which also implies that some unit be chosen as well.

The most intuitive choice is to let M be expressed in terms of $M_\odot$ and a in astronomical units (AU). The AU is equivalent to the mean distance of Earth from the Sun which has a standard value of 1.49597870700 x 10^{11} m (Luzum et al. 2011) as defined by the International Astronomical Union (IAU). For simplicity the time unit will be equal to a Julian Earth year which has a standard value of 365.25 days. Using the units of AU, $M_\odot$, and yr we can define $G = 4\pi^2 \frac{AU^3}{yr^2\, M_\odot}$. An alternate definition would be to change the magnitude of G to unity but leave the units unchanged, however this would change the definition of mass and force the $M_\odot = 4\pi^2$ in order for Kepler's Third Law to remain valid. Specifically this dissertation will use the first convention in the magnitude of $G = 4\pi^2$.

2.1.3 Equations of Motion

From Newton's Laws of motion a general definition of force can be developed. First, considering the static gravitational problem of N masses, a general expression exists to describe the force exerted on the i^{th} mass resulting from the presence of other j masses

$$\mathbf{F}_{ij} = -\frac{GM_iM_j}{r_{ij}^3}(\mathbf{r}_i - \mathbf{r}_j). \tag{2.2}$$

Equation 2.2 illustrates that the force due to gravity on the i^{th} would be directed radially inward as denoted by the difference of the vectors ($\mathbf{r}_i$,$\mathbf{r}_j$) which locate the masses relative to a point of reference.

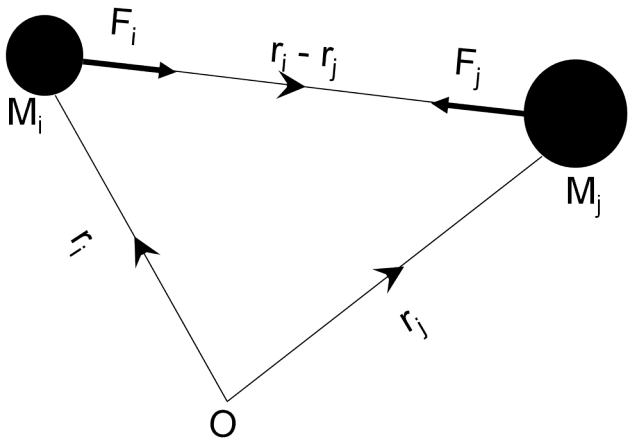

Figure 2.2. Depiction of gravitational forces between the i^{th} and j^{th} masses.

With modern numerical tools a slightly different form is required to advance the static definition to a dynamical one. As a result of Newton's 2$^{\text{nd}}$ Law, the acceleration $\mathbf{a}_{ij}$ is calculated rather than the force. A simple transformation can be obtained to define the acceleration as $\mathbf{a}_{ij} = \mathbf{F}_{ij}/M_i$. This expression is used most commonly to evaluate the N body problem, however there exists another formulation for the case where N = 3.

The circular restricted three body problem (CRTBP) uses a synodic coordinate system (See Figure 2.1b) to reduce the problem to the motion of only 1 body. It is important to note that this is a gross simplification of the general three body problem as it is possible to rotate coordinates of the system using operations from the SO(3) group. Specifically a rotation matrix can be applied with respect to the z-axis. However the equations of motion must be defined in the sidereal coordinate

system (ξ, η, ζ) in order to apply the resulting transformation. Using the vector form of Equation 2.2, the equations of motion of the third mass are

$$\ddot{\xi} = GM\left[\frac{\alpha\left(\xi_1 - \xi\right)}{r_1^3} + \frac{\mu\left(\xi_2 - \xi\right)}{r_2^3}\right], \tag{2.3}$$

$$\ddot{\eta} = GM\left[\frac{\alpha\left(\eta_1 - \eta\right)}{r_1^3} + \frac{\mu\left(\eta_2 - \eta\right)}{r_2^3}\right], \tag{2.4}$$

$$\ddot{\zeta} = GM\left[\frac{\alpha\left(\zeta_1 - \zeta\right)}{r_1^3} + \frac{\mu\left(\zeta_2 - \zeta\right)}{r_2^3}\right], \tag{2.5}$$

where

$$r_1^2 = \left(\xi_1 - \xi\right)^2 + \left(\eta_1 - \eta\right)^2 + \left(\zeta_1 - \zeta\right)^2, \tag{2.6}$$

$$r_2^2 = \left(\xi_2 - \xi\right)^2 + \left(\eta_2 - \eta\right)^2 + \left(\zeta_2 - \zeta\right)^2. \tag{2.7}$$

The necessary rotation matrix, R_{ab}, is given by

$$R_{ab} = \begin{pmatrix} \cos\theta & \sin\theta & 0 \\ -\sin\theta & \cos\theta & 0 \\ 0 & 0 & 1 \end{pmatrix}. \tag{2.8}$$

Equation 2.8 illustrates the general form of the necessary rotation matrix. The CRTBP requires a specific form which involves making the substitution $\theta = \omega\, t$. This substitution is not permitted in the elliptical restricted three body problem (ERTBP). The ERTBP does not permit this due to Kepler's 2$^{\text{nd}}$ Law of planetary motion that changes ω from a constant into a time dependent parameter. The following will show how the equations of motion are determined for the CRTBP and then the appropriate modifications will be made to satisfy the ERTBP.

First, the sidereal coordinates (ξ, η, ζ) will be rotated using Equation 2.8 with the aforementioned transformation.

$$\begin{pmatrix} \xi^* \\ \eta^* \\ \zeta^* \end{pmatrix} = \begin{pmatrix} \cos\omega t & \sin\omega t & 0 \\ -\sin\omega t & \cos\omega t & 0 \\ 0 & 0 & 1 \end{pmatrix} \begin{pmatrix} \xi \\ \eta \\ \zeta \end{pmatrix} \tag{2.9}$$

If we now differentiate Equation 2.9 twice we obtain the following accelerations $(\ddot{\xi}^*, \ddot{\eta}^*, \ddot{\zeta}^*)$.

$$\begin{pmatrix} \ddot{\xi}^* \\ \ddot{\eta}^* \\ \ddot{\zeta}^* \end{pmatrix} = \begin{pmatrix} \cos\omega t & \sin\omega t & 0 \\ -\sin\omega t & \cos\omega t & 0 \\ 0 & 0 & 1 \end{pmatrix} \begin{pmatrix} \ddot{\xi} - 2\omega\dot{\eta} - \omega^2\xi \\ \ddot{\eta} + 2\omega\dot{\xi} - \omega^2\eta \\ \ddot{\zeta} \end{pmatrix} \tag{2.10}$$

Using Equations 2.3, 2.4, and 2.5 substitutions can be made to obtain the following equations of motion in the synodic coordinate system

$$\ddot{\xi}^* - 2\omega\dot{\eta}^* - \omega^2\xi^* = -GM\left[\alpha\frac{\xi^* + GM\mu}{r_1^3} + \mu\frac{\xi^* - GM\alpha}{r_2^3}\right], \tag{2.11}$$

$$\ddot{\eta}^* - 2\omega\dot{\xi}^* - \omega^2\eta^* = -GM\left[\frac{\alpha}{r_1^3} + \frac{\mu}{r_2^3}\right]\eta, \tag{2.12}$$

$$\ddot{\xi}^* = -GM\left[\frac{\alpha}{r_1^3} + \frac{\mu}{r_2^3}\right]\zeta, \tag{2.13}$$

where (r_1, r_2) have been redefined as

$$\begin{aligned} r_1^2 &= (\xi^* + GM\mu)^2 + \eta^{2*} + \zeta^{2*}, \\ r_2^2 &= (\xi^* - GM\alpha)^2 + \eta^{2*} + \zeta^{2*}. \end{aligned} \tag{2.14}$$

It is important to note that the synodic reference frame has introduced the Coriolis's and centrifugal acceleration into the equations of motion. In addition Equations 2.11, 2.12, and 2.13 can be written as the gradient of a psuedopotential U:

$$\begin{aligned} \ddot{\xi}^* - 2\omega\dot{\eta}^* &= \frac{\partial U}{\partial \xi^*}, \\ \ddot{\eta}^* + 2\omega\dot{\xi}^* &= \frac{\partial U}{\partial \eta^*}, \\ \ddot{\zeta}^* &= \frac{\partial U}{\partial \zeta^*}, \end{aligned} \tag{2.15}$$

where $U = U\left(\xi^*, \eta^*, \zeta^*\right)$ is given by

$$U = \frac{\omega^2}{2}\left(\xi^{2*} + \eta^{2*}\right) + GM\left(\frac{\alpha}{r_1} + \frac{\mu}{r_2}\right). \tag{2.16}$$

The equations of motion in the ERTBP are similar to those of the CRTBP but there are some important distinctions to mention. First of which is that the ERTBP has to incorporate true anomaly, f, into the equations of motion because Kepler's 2^{nd} Law forces f to vary with time. This also implies that the synodic coordinate system cannot be rotated at a constant rate. Thus an additional equation of motion must be included to determine f at each instant of time. Additionally eccentricity will effect the equations of motion so that the CRTBP psuedopotential U will become the ERTBP psuedopotential Ω given by

$$\Omega = (1 + e\cos f)^{-1}\left[\frac{1}{2}\left(\xi^{2*} + \eta^{2*} - e\zeta^{2*}\cos f\right) + GM\left(\frac{\alpha}{r_1} + \frac{\mu}{r_2}\right) + \frac{\mu\alpha}{2}\right], \tag{2.17}$$

and

$$\dot{f} = \frac{GM^{\frac{1}{2}}}{[a(1-e^2)]^{\frac{3}{2}}}(1 + e\cos f)^2. \tag{2.18}$$

2.1.4 Orbital Elements

An alternate method of analyzing problems exists within celestial dynamics. When a clear hierarchy of mass can be formed as in the CRTBP and ERTBP it is useful to describe the system in terms of the orbital elements of each body. The orbital elements are also constants of motion for the appropriate 2 body problem. In the 3 body problem orbital elements are defined relative to a Jacobi coordinate system where the most massive body is taken to be the reference. Therefore M_2 and M_3 would have each a set of orbital elements relative to M_1.

For the 2 body problem the orbital elements are semimajor axis (a), inclination (I), eccentricity (e), argument of perihelion (ω), right ascension of the ascending node (Ω), and true anomaly (f).

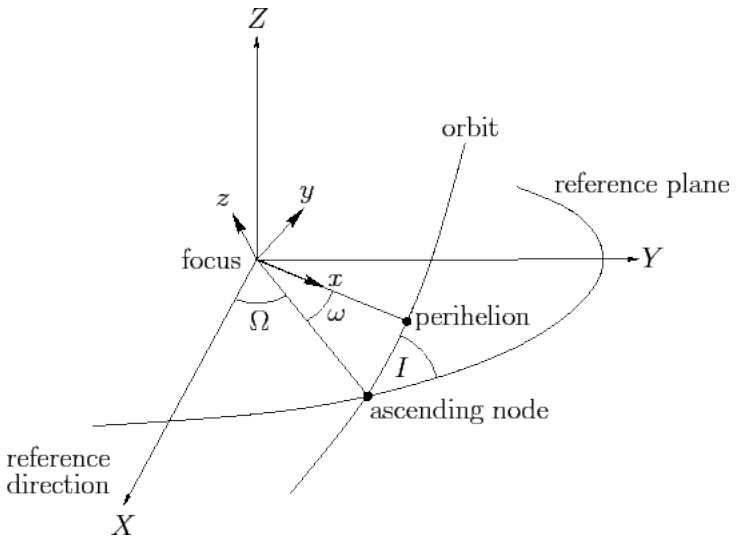

Figure 2.3. Illustration of the orbital elements that exist in a system that is not coplanar. Image Credit: Richard Fitzpatrick.

Figure 2.3 shows the orbital elements that will be non-zero in the case of orbits that are not coplanar. The remaining orbital elements exist regardless of the

reference plane. Using Lagrange's Planetary equations, a system can be simulated with respect to the orbital elements (Murray & Dermott 1999) which is an optional parameter in integration packages such as Mercury and Swifter. This dissertation makes use of how the orbital elements can change with time due to the nonlinearity of the N body problem. As such, the simulations are performed within the previously defined coordinates systems and appropriate conversions are made to the corresponding orbital elements using the orbital state vectors. More details concerning these transformations are given in Appendix A.

2.1.5 Zero Velocity Surface and Functions

The Zero Velocity Surface (ZVS) is used in the CRTBP to define the region of space where the third mass is allowed to exist. For the elliptic case a Zero Velocity Function (ZVF) is employed that is dependent on the true anomaly, f, of the 2 more massive bodies. Both the ZVS and ZVF are determined from the corresponding Jacobi integral.

The Jacobi integral in the CRTBP produces the so-called Jacobi constant, C_J. This comes from multiplying Equation 2.11 by $\dot{\xi}^*$, Equation 2.12 by $\dot{\eta}^*$, Equation 2.13 by $\dot{\zeta}^*$, and summing the results together to get

$$\dot{\xi}^*\ddot{\xi}^* + \dot{\eta}^*\ddot{\eta}^* + \dot{\zeta}^*\ddot{\zeta}^* = \frac{dU}{dt}. \tag{2.19}$$

Equation 2.19 can thus be integrated to give

$$\begin{aligned} \dot{\xi}^{2*} + \dot{\eta}^{2*} + \dot{\zeta}^{2*} &= 2U - C_J, \\ v^2 &= 2U - C_J. \end{aligned} \tag{2.20}$$

Therefore the ZVS can be formally defined as the points which $v = 0$ or $2U = C_J$. To draw the appropriate contours, the value of C_J is determined from the initial conditions and then, the previous condition is applied. Also the quantity C_J becomes a constant of motion for the CRTBP. Regions beyond the ZVS or forbidden regions are not allowed because to enter such regions would imply a purely imaginary velocity which results in an unphysical solution.

The generalized ZVF is an extension of the ZVS that incorporates the parameters for eccentricity and true anomaly. This is determined in a similar manner but with $C_J(f)$ rather than only a constant C_J. It is easily written by replacing the psuedopotential U with Ω as given in Equation 2.17 to produce the relation $C_J(f) = 2\Omega(\xi^*, \eta^*, \zeta^*, f)$. Solving analytically the integrals for $C_J(f)$ can be especially daunting but numerical methods exist and a Hill-stability criterion has been formed based on the numerical result (Szenkovits & Makó 2008).

2.2 Tools from Chaos Theory

Chaos theory has been effectively applied to different astronomical problems, including some problems of orbital mechanics. Many of these applications have been explored in the study of asteroids within the Solar System. This dissertation will utilize certain techniques that have been under development since the 1980s (Benettin et al. 1980; Froeschle 1984; Ferraz-Mello & Dvorak 1987; Dvorak & Karch 1988; Smith & Szebehely 1993; Murray & Holman 2001, and references therein). Specifically, the theory for the calculation of Lyapunov exponents will be described as well as a brief introduction to linear stability theory and perturbation theory.

2.2.1 Fourier Transform

Some of the basic tools for the analysis in chaos theory comes from advancements made prior to its development. One of those great achievements is called the Fourier transform (Fourier 1822). This mathematical tool was developed by Jean Baptiste Fourier to study the time evolution of heat diffusion. However the use of this tool has been extended to much broader applications including the analysis of a time series. The basic definition of the Fourier transform involves a time dependent function $\chi(t)$. This function can exist in another mathematical space called "phase space" where the frequency becomes the independent coordinate. The Fourier transform demonstrates mathematically how to obtain the form of the function in both spaces, position and phase. This relationship is given by

$$\chi(t) = \int_{-\infty}^{\infty} F(f) e^{2i\pi ft} df, \tag{2.21}$$

$$F(f) = \int_{-\infty}^{\infty} \chi(t) e^{-2i\pi ft} dt. \tag{2.22}$$

The Fourier transform (Equation 2.21) and the inverse Fourier transform (Equation 2.22) provide an analytic means of performing analysis upon a source function. As it can take quite a long time to calculate the Fourier transform for a general function, numerical techniques were introduced. The fast Fourier transform (FFT) was introduced in the 1960s and the Cooley-Tukey algorithm is one of the most commonly used (Cooley & Tukey 1965). However, it was later discovered that this algorithm was merely reinvented and originally determined by Johann Carl Friedrich Gauss in 1805 (Heideman et al. 1984). Since numerical techniques evolve over time there is another computational library which has made the FFT the most optimized into the FFT of the west (FFTW). FFTW (Frigo & Johnson 1998) has undergone 3 distinct versions to the current version FFTW3 (Frigo & Johnson 2005). This dissertation

heavily uses this particular tool and the libraries of FFTW in the software package Matlab® (MATLAB 2011).

The importance of the use of the FFT is that it can differentiate a periodic source into three categories: noisy, quasi-periodic, and periodic signals (Tsonis 1992). A noisy signal is indicated by the lack of a specific frequency that would dominate over all other frequency in the time series. A periodic signal will show one distinct frequency that will dominate over all others in an appropriate power spectrum. A quasi-periodic signal can be characterized as the linear combination of many frequencies which is represented in a power spectrum by many frequencies dominating over the background (noise). Since the objects in the N body problem experience periodic influences from their neighbors this tool is appropriate in such research.

2.2.2 Linear Stability

The N body problem exhibits inherent nonlinear behavior, but whether that nonlinear behavior will lead to instability is a topic of current research. The most common first step in trying to determine the stability of a nonlinear system is to approximate the system as linear over a sufficiently small time. This section will outline the basics of linear stability theory to provide the necessary background to discuss future nonlinear analysis methods.

Linear systems in mathematics are generally studied using a set of coupled first order differential equations. Let us consider, for example, a set of two linear, first order homogeneous differential equations:

$$\dot{x_1} = a_{11}x_1 + a_{12}x_2,$$
$$\dot{x_2} = a_{21}x_1 + a_{22}x_2, \tag{2.23}$$

where a_{ij} represent constants. Equation 2.23 can be rewritten into a matrix form, $\dot{\mathbf{x}} = A\mathbf{x}$, where

$$A = \begin{pmatrix} a_{11} & a_{12} \\ a_{12} & a_{22} \end{pmatrix} \qquad \mathbf{x} = \begin{pmatrix} x_1 \\ x_2 \end{pmatrix} \qquad \dot{\mathbf{x}} = \begin{pmatrix} \dot{x}_1 \\ \dot{x_2} \end{pmatrix} \tag{2.24}$$

Considering that the solution to the scalar equation $\dot{x} = ax$ exists, we should assume a similar solution as it matches the form of $\dot{\mathbf{x}}$ which is

$$\mathbf{x}(t) = \mathbf{c}e^{\lambda t}, \tag{2.25}$$

where λ is a scalar and $\mathbf{c}$ is a nonzero vector $\binom{c_1}{c_2}$. Substituting this solution into $\dot{\mathbf{x}}$ the result is obtained as $A\mathbf{c} = \lambda\mathbf{c}$ with the eigenvector λ. A nontrivial solution is desired, thus properties of matrices are used from linear algebra including the Identity matrix I. It is necessary that

$$\text{Det}(A - \lambda\, I) = 0. \tag{2.26}$$

Equation 2.26 can be solved using the appropriate coefficients from A and the eigenvector λ. The solution results in a characteristic equation in terms of λ in the form

$$\lambda^2 + \lambda\, \text{Trace}\, A + \text{Det}\, A = 0. \tag{2.27}$$

The property of Equation 2.27 which is important is the eigenvalues λ_1, λ_2 are either both real or complex which will admit exponential and oscillatory solutions. Also we can solve for the eigenvalues using the general solution to a quadratic equation so that

$$\lambda_{1,2} = \frac{\text{Trace } A - \sqrt{(\text{Trace } A)^2 - 4 \,\text{Det } A}}{2} \tag{2.28}$$

Equation 2.28 provides two important properties that will be used in this dissertation. It can easily be shown that

$$\begin{aligned} \lambda_1 \lambda_2 &= \text{Det } A \\ \lambda_1 + \lambda_2 &= \text{Trace } A \end{aligned} \tag{2.29}$$

The result in Equation 2.29 will hold true for a general homogeneous system of n first order differential equations.

2.2.3 Nonlinear Stability

When dealing with nonlinear systems, an analytic solution is usually not obtainable. In this case the system is expressed in terms of a set of nonlinear functions of the appropriate coordinates. Again we use the form $\dot{\mathbf{x}} = A\mathbf{x}$, however the elements of $\dot{\mathbf{x}}, A$, and $\mathbf{x}$ will be considered to be n dimensional such that

$$A = \begin{pmatrix} a_{11} & a_{12} & \cdots & a_{1n} \\ a_{21} & a_{22} & \cdots & a_{2n} \\ \vdots & \vdots & & \vdots \\ a_{n1} & a_{n2} & \cdots & a_{nn} \end{pmatrix} \tag{2.30}$$

Applying Equation 2.26 to Equation 2.30 and assuming $\mathbf{x}$ to contain n nonlinear functions dependent on n coordinates, it can be shown that the matrix A represents the Jacobian matrix J, ie., $A = J$. Then Equation 2.30 becomes

$$A = \begin{pmatrix} \frac{\partial f_1}{\partial x_1} & \frac{\partial f_1}{\partial x_2} & \cdots & \frac{\partial f_1}{\partial x_n} \\ \frac{\partial f_2}{\partial x_1} & \frac{\partial f_2}{\partial x_2} & \cdots & \frac{\partial f_2}{\partial x_n} \\ \vdots & \vdots & & \vdots \\ \frac{\partial f_n}{\partial x_1} & \frac{\partial f_n}{\partial x_2} & \cdots & \frac{\partial f_n}{\partial x_n} \end{pmatrix} \tag{2.31}$$

Nonlinear systems are usually categorized as being either conservative or dissipative. This is determined by the Hamiltonian and some properties of the Jacobian. First, the category can be determined by inspection of the Hamiltonian for time dependence. Dynamical systems whose Hamiltonian **does not** vary with time are designated as being conservative. Otherwise, the system is considered to be dissipative. The Hamiltonian of the gravitational N body problem is time independent, thus this dissertation will operate within the conservative regime of nonlinear dynamics.

Conservative systems have some useful properties, the most important for this dissertation is the conservation of volumes in phase space. This is shown by considering the N body problem to be like a fluid. Thus using generalized coordinates (q,p), which represent phase space, the density ρ of the fluid at a time t with the fluid moving with a velocity $\mathbf{v}$ obeys the following continuity equation

$$\frac{\partial \rho}{\partial t} + \nabla \cdot (\rho \mathbf{v}) = 0 \tag{2.32}$$

In order to evaluate Equation 2.32, the variable dependence must be determined. The density has the form $\rho = \rho(q, p, t)$ and the velocity has the form $\mathbf{v} = \mathbf{v}(q, p)$ such that the chain rule can be applied

$$\nabla \cdot (\rho \mathbf{v}) = \mathbf{v}(\nabla \cdot \rho) + \rho(\nabla \cdot \mathbf{v}). \tag{2.33}$$

Recalling that for conservative systems $\nabla \cdot \mathbf{v} = 0$, the resulting equation becomes

$$\nabla \cdot (\rho \mathbf{v}) = \mathbf{v}(\nabla \cdot \rho). \tag{2.34}$$

Substituting Equation 2.34 into Equation 2.32 and rewriting in terms of the full time derivative

$$\frac{\mathrm{d}\rho}{\mathrm{d}t} = 0. \tag{2.35}$$

Thus, since $m = \rho V$, where V denotes volume and m is constant with respect to time, therefore $\frac{\mathrm{d}V}{\mathrm{d}t} = 0$. This results demonstrates that the volumes in phase space are conserved which indicates that the Trace $A = 0$. The resulting eigenvalues can be shown to have the property using a generalization of Equation 2.29 to get

$$\lambda_1 + \lambda_2 + \ldots + \lambda_n = 0. \tag{2.36}$$

2.2.4 Lyapunov Exponent

In the analysis of nonlinear phenomena, many different methods exist to gauge the stability within a nonlinear system. One such method involves the calculation and interpretation of the Lyapunov exponents (Lyapunov 1907). This dissertation will use this method to determine the timescale for which a particular system is deterministic

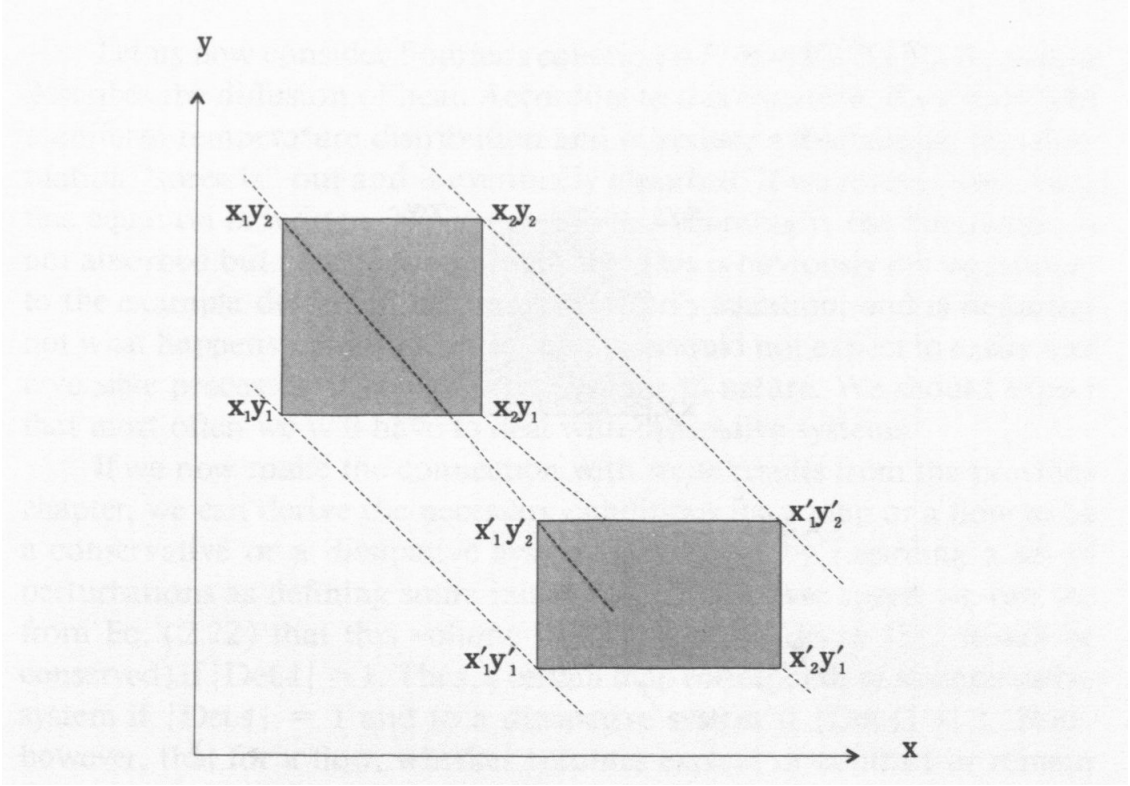

Figure 2.4. Illustration of the conservation of volumes in the phase space (x,y). The volumes may be deformed, but they remain the same. Image Credit: Anastasios Tsonis (1992).

and as a stability criterion. The Lyapunov exponents are a measure of the change in nearby trajectories differentiated by initial conditions (See Figure 2.5). This description is analogous to the eigenvalues given in Equation 2.28 and display the same properties as given in Equation 2.29. The positive Lyapunov exponents measure the rate of divergence of neighboring orbits, whereas negative exponents measure convergence rates between stable manifolds. For dissipative dynamical systems the sum of all Lyapunov exponents is less than 0 (e.g., Musielak & Musielak 2009); however, for Hamiltonian (non-dissipative) systems the sum is equal to 0 (e.g., Hilborn 1994). In addition the inverse of the maximum Lyapunov exponent will provide an estimate of

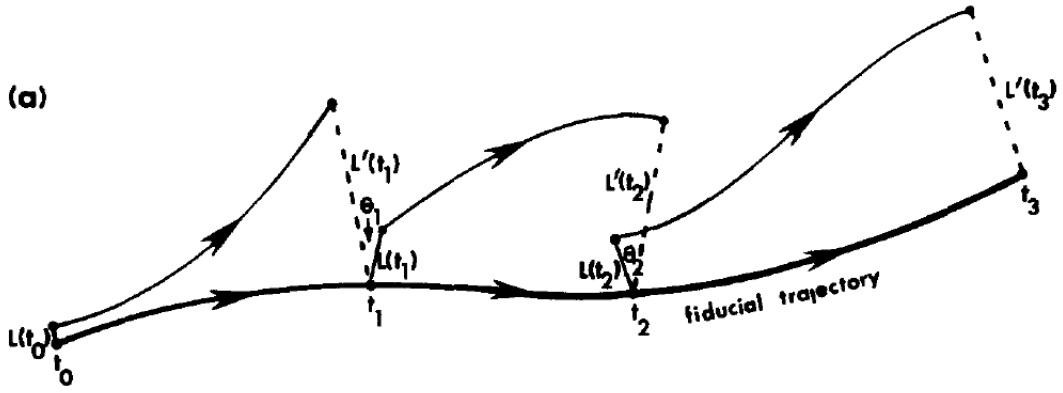

Figure 2.5. Illustration of the variations of nearby trajectories that define the Lyapunov exponents. Image Credit: Wolf et al. (1985).

how long a system will remain deterministic or a measure of predictive time (Musielak & Musielak 2009).

Specific applications of the Lyapunov exponents to the CRTBP have been discussed by many authors, including Gonczi & Froeschle (1981), Jefferys & Yi (1983), Lecar et al. (1992), Milani & Nobili (1992), Smith & Szebehely (1993) and Murray & Holman (2001). In order to use the method of Lyapunov exponents on the gravitational N body problem, the Jacobian A must be defined for such a system. Since there exists two possible types of barycentric coordinate systems (sidereal and synodic), the Jacobian will be defined for both and each one would be used with the appropriate coordinate system. In the case of the synodic barycentric system, the third mass will have its own Jacobian where as the sidereal case each mass will have its own Jacobian.

A dynamical system with n degrees of freedom is represented in $2n$ phase space; thus, to fully determine stability of the system all $2n$ Lyapunov exponents must be calculated. The previously obtained results for the CRTBP clearly show that the Lyapunov exponents can be calculated for the case of the CRTBP, for which we

have $2n = 6$. This requires a state vector, $\mathbf{x}$, for the system containing 6 elements $(\xi, \eta, \zeta, \dot{\xi}, \dot{\eta}, \dot{\zeta})$. It is the convention that positive Lyapunov exponents indicate that both dissipative (e.g., Hilborn 1994) and non-dissipative (e.g., Ozorio de Almeida 1990) systems are chaotic. This dissertation will use the end value of the maximum Lyapunov exponent in a time series to make distinction between chaotic and non-chaotic orbits. The synodic Jacobian uses the equations of motion given in Equation 2.15 where

$$A = \begin{pmatrix} 0 & 0 & 0 & 1 & 0 & 0 \\ 0 & 0 & 0 & 0 & 1 & 0 \\ 0 & 0 & 0 & 0 & 0 & 1 \\ \frac{\partial \ddot{\xi}^*}{\partial \xi^*} & \frac{\partial \ddot{\xi}^*}{\partial \eta^*} & \frac{\partial \ddot{\xi}^*}{\partial \zeta^*} & 0 & 2 & 0 \\ \frac{\partial \ddot{\eta}^*}{\partial \xi^*} & \frac{\partial \ddot{\eta}^*}{\partial \eta^*} & \frac{\partial \ddot{\eta}^*}{\partial \zeta^*} & -2 & 0 & 0 \\ \frac{\partial \ddot{\zeta}^*}{\partial \xi^*} & \frac{\partial \ddot{\zeta}^*}{\partial \eta^*} & \frac{\partial \ddot{\zeta}^*}{\partial \zeta^*} & 0 & 0 & 0 \end{pmatrix}. \tag{2.37}$$

Using the synodic Jacobian is useful to investigate the CRTBP and ERTBP, but lacks a general scope to investigate a N body problem. Thus the Jacobian in the sidereal barycentric coordinates can be used in general studies as

$$A_i = \begin{pmatrix} 0 & 0 & 0 & 1 & 0 & 0 \\ 0 & 0 & 0 & 0 & 1 & 0 \\ 0 & 0 & 0 & 0 & 0 & 1 \\ \frac{\partial \ddot{\xi}_i}{\partial \xi_i} & \frac{\partial \ddot{\xi}_i}{\partial \eta_i} & \frac{\partial \ddot{\xi}_i}{\partial \zeta_i} & 0 & 0 & 0 \\ \frac{\partial \ddot{\eta}_i}{\partial \xi_i} & \frac{\partial \ddot{\eta}_i}{\partial \eta_i} & \frac{\partial \ddot{\eta}_i}{\partial \zeta_i} & 0 & 0 & 0 \\ \frac{\partial \ddot{\zeta}_i}{\partial \xi_i} & \frac{\partial \ddot{\zeta}_i}{\partial \eta_i} & \frac{\partial \ddot{\zeta}_i}{\partial \zeta_i} & 0 & 0 & 0 \end{pmatrix}. \tag{2.38}$$

The sidereal Jacobian, A_i, carries with it an index to denote the Jacobian for the i^{th} mass. Also, it is important to note that Equation 2.38 can be represented by 4 matrices with 3 x 3 elements so that the null matrices (top left and bottom right) can be excluded to reduce the number of calculations. Additionally, Equations 2.3, 2.4, and 2.5 provide the necessary accelerations to evaluate the sidereal Jacobian, A_i. However, the number of calculations will increase as N increases so that the usage of A_i can become computationally expensive.

The details of the calculation of the Lyapunov exponents can be found in Appendix A. The particular algorithm used in the calculations is adapted from an algorithm given by Wolf et al. (1985). This algorithm uses Gram-Schmidt renormalization which can become computationally expensive. Alternate methods using Lyapunov exponents as a basis of analysis have been introduced (Froeschle 1984; Laskar et al. 1992; Lohinger et al. 1993; Lohinger & Froeschle 1993; Froeschlé et al. 1997; Froeschlé & Lega 2000; Fouchard et al. 2002, and references therein). The most commonly used alternative is the fast Lyapunov indicator (FLI) which measures the largest change in the tangent vector $\dot{\mathbf{x}}$. The FLI is calculated via the expression

$$\text{FLI} = \sup_{0<k<T} \log \left\| \dot{\mathbf{x}}_k(t) \right\| . \tag{2.39}$$

Usage of the FLI is much less computationally expensive to the calculation of the Lyapunov exponents via the Wolf method (Wolf et al. 1985) due to the fact that it involves only evaluations and not the integration of the tangent vector, $\dot{\mathbf{x}}$. Other methods include the relative Lyapunov indicator, orthogonal FLI, and the orthogonal FLI_2. This dissertation uses the full Lyapunov exponent spectrum for much of the analysis as it was developed for the simulation methods of Eberle & Cuntz (2010a).

2.2.5 Perturbation Theory

The evaluation of resonant phenomena often requires analysis considering perturbation theory. This section will provide a brief introduction to the theory along with a description of possible numerical applications. Perturbation theory assumes that the accelerations of the lesser massive bodies (M_2, M_3) are dominated by a central or primary body. This implies that the motions of (M_2, M_3) will result in conic sections with small deviations due to their mutual gravitational perturbations (Murray & Dermott 1999). The assumption considers a disturbing function, R, which can be introduced to account for the interaction terms of the perturbation.

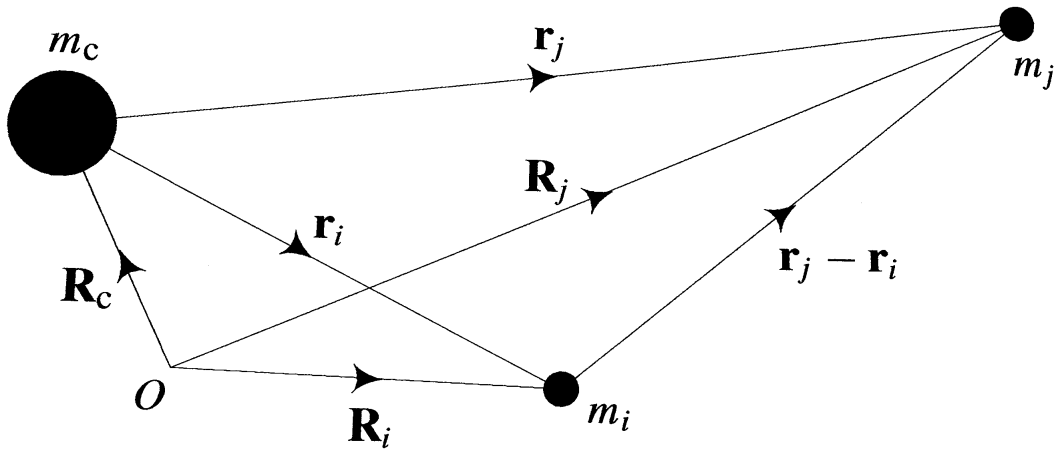

Figure 2.6. The position vectors $\mathbf{r}_i$ and $\mathbf{r}_j$, of two masses m_i and m_j with respect to the central mass m_c. The three masses have position vectors $\mathbf{R}$, $\mathbf{R}'$, and $\mathbf{R}_c$ with respect to an arbitrary, fixed origin O. This figure was adapted from Murray & Dermott (1999).

Comparing Figure 2.1a to 2.6, it can easily be shown that the arbitrary, fixed origin O could be chosen as the barycenter which would make the figures equivalent. Using this equivalence, the disturbing functions R_i and R_j can be shown to be

$$R_i = Gm_j \left(\frac{1}{|\mathbf{r}_j - \mathbf{r}_i|} - \frac{\mathbf{r}_i \cdot \mathbf{r}_j}{r_j^3} \right),$$

and

$$R_j = Gm_i \left(\frac{1}{|\mathbf{r}_j - \mathbf{r}_i|} - \frac{\mathbf{r}_i \cdot \mathbf{r}_j}{r_i^3} \right). \tag{2.40}$$

Equation 2.40 clearly shows each disturbing function to be a first order expansion of the corresponding gravitational potential. Thus the standard practice of an expansion of $|\mathbf{r}_j - \mathbf{r}_i|$ into Legendre polynomials can be performed using the angle ψ that is made with respect to $\mathbf{r}_j$ and $\mathbf{r}_i$ to give

$$\frac{1}{|\mathbf{r}_j - \mathbf{r}_i|} = \frac{1}{r_j} \sum_{l=0}^{\infty} \left(\frac{r_i}{r_j} \right)^l P_l (\cos \psi). \tag{2.41}$$

Equation 2.41 assumes that $r_i < r_j$ and if this condition were to fail the resulting situation would describe a system where the indices i and j are interchanged. Following this point it becomes more useful to express the disturbing function in terms of orbital elements rather than Cartesian coordinates, which gives

$$R_i = Gm_j \sum S(a_i, a_j, e_i, e_j, I_i, I_j) \cos \varphi. \tag{2.42}$$

The expression for R_j would have the same form with a change in the respective indices. Finding the angle φ is at the center of the analysis of resonances, so a procedure to determine this angle is now presented.

The angle φ is also called the resonant angle. This is because a relationship between the mean longitudes (λ), longitudes of pericenter (ϖ), and right ascensions of the ascending node (Ω) can be made using integers k, l, and m. The resonant angle is defined as

$$\varphi = k_j\lambda_j + k_i\lambda_i + l_j\varpi_j + l_i\varpi_i + m_j\Omega_j + m_i\Omega_i \tag{2.43}$$

where $k_j + k_i + l_j + l_i + m_j + m_i = 0$ due to the azimuthal invariance of the central mass' potential.

In practice determining the integers k, l, and m can become difficult using only analytical means. As a result a number of methods exist for determining k, l, and m through the determination of orbital resonances. Orbital resonances are defined to be rational expressions of the frequencies/periods of the smaller masses, m_j and m_i. For example, a 2:1 mean motion resonance (MMR) would describe a case where m_i would orbit m_c two times for every orbit of m_j around m_c and the term mean motion denotes that the resonance is a simple integer ratio (See Figure 2.7).

Hadjidemetriou (1993) used the method of averaging as well as the method of computing periodic orbits numerically. He showed how to utilize these methods to determine MMRs; furthermore, he discussed the advantages and disadvantages of each method as well as the effects of their inherent limitations on the attained results. Another method of finding MMRs is based on the concept of Lyapunov exponent as introduced by Nesvorný & Morbidelli (1998) with its further development by Morbidelli & Nesvorny (1999) and Nesvorný et al. (2002).

This dissertation will use a modified version of the method presented by Nesvorný et al. (2002). This modified method uses the maximum Lyapunov exponent as an indicator to provide information about the position of MMRs with respect to distance from m_c. Furthermore, it uses numerical tools such as FFT to determine the orbital periods of the masses orbiting m_c. Once the type of resonance is identified, it can then be classified as a resonance that leads to periodic, quasi-periodic, or non-periodic behavior.

2.2.6 Chaos in the Solar System

Studies of dynamics within astronomy can inevitably lead to the study of chaos. In terms of the N body problem, all systems where N > 2 can exhibit chaos within an appropriate range of initial conditions. This is evident in studies of the Solar System. Numerous applications to describe the motion of planets, asteroids and artificial satellites in the Solar System are well-known (Dvorak 1984, 1986; Murray & Dermott 1999; Rabl & Dvorak 1988; Smith & Szebehely 1993; Szebehely 1967, and references therein). Additional applications have been made to understand dynamics beyond just orbital but dynamics concerning the obliquity and rotation of different objects within the Solar System as well (Touma & Wisdom 1993; Laskar & Robutel 1993a; Laskar et al. 1993; Lissauer et al. 2011).

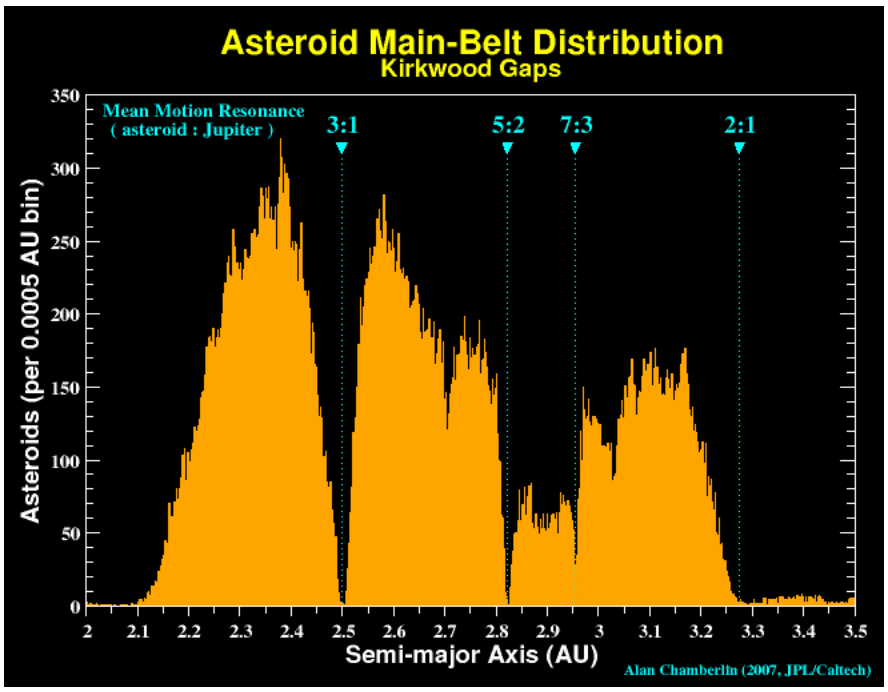

Figure 2.7. Illustration of the distribution of asteroids within the Solar System with respect to orbital semimajor axis. Image Credit: Alan Chamberlin.

The above brief description shows the role played by chaos in planetary systems and in the evolution of planetary atmospheres (Cuntz et al. 2009; Musielak et al. 2010). Altogether the study of chaos in planetary systems is imperative and the necessity for its advancement is great.

2.3 Habitable Zones

The pursuit of life outside Earth has encapsulated the imagination of humanity since antiquity with the invention of the gods. But considerable progress has been made within the past century in placing scientific constraints on the possibility of extra-terrestrial life. In terms of celestial mechanics and astrobiology, a region has been defined to encapsulate the volume of space where potentially life harboring planets may exist. This region has been dubbed the "habitable zone" (Huang 1960) or "ecosphere" (Dole 1964; Shklovskii & Sagan 1966). The limits were defined through the assumption of climatic constraints which varied by the author. Currently the habitable zone (HZ) has been defined as the distance a planet can exist from its host star where it can maintain liquid water on the planetary surface (Kasting et al. 1993). This definition is the most basic and climate models have been studied to adjust the definition based on factors such as atmospheric conditions, cloud cover, and albedo.

The considerations of atmospheric conditions are largely determined through proposed feedback loops which occur within the atmosphere on Earth and include cycles of geology. Because the estimates for life to take hold on a planet is 1 billion years (Gyr) the effects of geology have to be considered. A strong negative feedback mechanism exists through the carbonate-silicate cycle to help stabilize the climate of a planet (Kasting et al. 1993). This cycle naturally occurs when silicate weathering removes carbon from the atmosphere and oceans. Then the carbon is restored

through the subduction of the seafloor and when gaseous CO_2 is released back into the atmosphere via volcanic processes.

It had become apparent that the type of atmospheric constituents and the behavior of the atmosphere would determine habitability. Thus estimates of the HZ were now able to be represented quantitatively. These estimates were formed using the Earth and Sun as test objects and proper scaling would identify conditions different from this ideal case. The inner edge of the HZ was estimated using a model of the effective solar flux, S_{eff}, that is a function of the incident solar flux, F_S, and the net outoging infrared flux, F_{IR}. The effective solar flux is defined as

$$S_{eff} = \frac{F_{IR}}{F_S}. \tag{2.44}$$

Kasting et al. (1993) demonstrates that an inflection point occurs at a critical temperature, $T_{crit} = 647K$. At this point the test Earth would have a $S_{eff} = 1.4$ which is 40% larger than the current value. The region beyond $S_{eff} = 1.4$ constitutes a runaway greenhouse effect. Since flux behaves as an inverse square law (ie., $1/d^2$), the inner boundary relative to the Solar System can be estimated as

$$d = \frac{1AU}{\sqrt{S_{eff}}}. \tag{2.45}$$

The next limit that was defined is called the water loss limit. This indicates what value of S_{eff} is required for a planet to begin to lose its water through photodissociation. Water loss occurs at $S_{eff} = 1.1$ or $d = 0.95$ AU (Kasting et al. 1993). The final limit was determined is called "Early Mars".

Early Mars occurs when the temperature is low enough for CO_2 clouds to form within the atmosphere. In this condition the lower atmosphere can be warmed via greenhouse processes, however the upper atmosphere would most certainly not contain

water vapor as the reflectivity of such clouds would increase the albedo of the test planet. The S_{eff} of an Early Mars-type planet would occur at $d = 1.67$ AU. Kasting et al. (1993) demonstrated through simulations with stars of varying spectral type that the Earth-Sun result would scale as a function of stellar surface temperature. Thus Equation 2.45 should be modified to become

$$d = 1\mathrm{AU}\sqrt{\frac{L/L_{\odot}}{S_{\mathrm{eff}}}}. \tag{2.46}$$

Other boundaries are also given by Kasting et al. (1993). These boundaries include the regions where the 1^{st} CO_2 concentrations would occur as well as the region when a maximum greenhouse effect would keep the liquid water from freezing. Another aspect to consider in HZs is that the host star evolves during its lifetime. Since 1 Gyr is considered to be a sufficient time for life to develop, it also corresponds to a order of evolutionary time of a star, specifically a G2 dwarf similar to the Sun. Since this occurs an alternate region is defined as the continuous habitable zone (CHZ). The CHZ describes a time dependent HZ, but the lifetime of a Sun-like star is 10 Gyr so the time changes are very slow. Simulations concerning HZs in this dissertation occur over timescales of 1 million years (Myr). Hence little emphasis will be placed on this aspect of habitability. Figure 2.8 illustrates the extent of HZs for stars of different temperature and mass.

Underwood et al. (2003) further define the HZ in their investigation of the dynamics of habitability. They consider systems where planets may exit the HZ for brief excursions due to the eccentricity of the planetary orbit. Using the CHZ definition, these configurations may permit habitability after the host star evolves and the HZ shifts outward in response. To this end, the stellar interiors were modeled

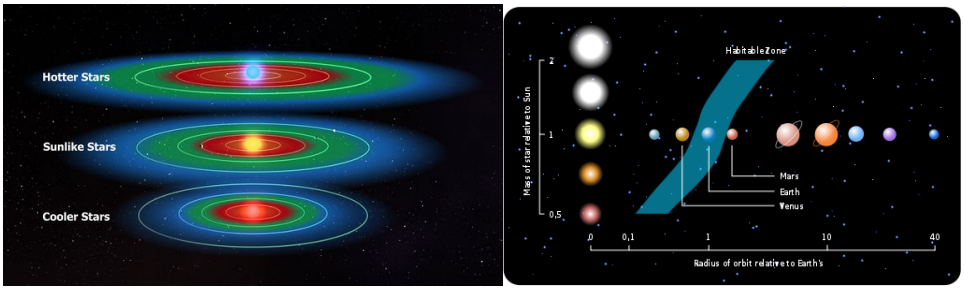

(a) (b)

Figure 2.8. Current depiction of the habitable zone for single star systems. (a) Image Credit: NASA/Kepler Mission/Dana Berry. (b) Image Credit: NASA.

to determine the rate at which the star's temperature would increase due to its own evolution.

Table 2.1. Coefficients for S_{eff} of the form $S_{eff} = AT_e^2 + BT_e + C$ (Underwood et al. 2003).

Boundary Type	A (x 10^{-9})	B (x 10^{-5})	C
Recent Venus	22.86	-13.49	1.786
Runaway Greenhouse	41.90	-21.39	1.268
Water Loss	14.29	-8.429	1.116
1^{st} CO_2 Concentration	5.238	-1.424	0.4410
Maximum Greenhouse	6.190	-1.319	0.2341
Early Mars	5.714	-1.371	0.2125

As a result, the parameter S_{eff} was adjusted by the effective stellar temperature, T_e, to better estimate the effective stellar flux through a power series for each previously defined boundary. It should be noted that this investigation neglected the possibility of cloud cover as suggested by Mischna et al. (2000); Williams & Kasting (1997).

The effect of cloud cover has been investigated by Mischna et al. (2000); Selsis et al. (2007). This effect has been shown to substantially widen the HZ. With 100% cloud cover the inner and outer boundaries of the HZ can be set to 0.46 and 2.4 AU, respectively. Selsis et al. (2007) uses a similar power law approach as shown in Table 2.1 where the coefficient C is modified to account for the proposed cloud cover. However, this dissertation considers this result only briefly as the calculations for Kepler 16 (Doyle et al. 2011) exist primarily within a conservative HZ definition without considering cloud cover.

CHAPTER 3

THE LYAPUNOV EXPONENT CRITERION

In order to address the first project in Section 1.5, I begin to establish a criterion for the stability of planetary orbits in stellar binary systems by using Lyapunov exponents and power spectra for the special case of the CRTBP. The determined criterion augments the earlier results given in the two previous papers of the series, *The instability transition for the restricted 3-body problem*, where stability criteria have been developed based on the Jacobi constant and the hodograph method.

The centerpiece of this method is the concept of Lyapunov exponents, which are incorporated into the analysis of orbital stability by integrating the Jacobian of the CRTBP and orthogonalizing the tangent vectors via a well-established algorithm originally developed by Wolf et al. (1985). The criterion for orbital stability based on the Lyapunov exponents is independently verified by using power spectra. The obtained results are compared to results presented in the two previous papers of this series.

It is then shown that the maximum Lyapunov exponent can be used as an indicator for chaotic behavior of planetary orbits, which is consistent with previous applications of this method, particularly studies for the Solar System. The chaotic behavior can correspond to either orbital stability or instability, and it depends solely on the mass ratio μ of the binary components and the initial distance ratio ρ_0 of the planet relative to the stellar separation distance. Detailed case studies are presented for $\mu = 0.3$ and 0.5. The stability limits are characterized based on the value of the maximum Lyapunov exponent. However, chaos theory as well as the concept of

Lyapunov time prevents us from predicting exactly when the planet is ejected. This method is also able to indicate evidence of of quasi-periodicity and resonance.

For different mass ratios of the stellar components, this dissertation is able to characterize stability limits for the CRTBP based on the value of the maximum Lyapunov exponent. This theoretical result allows a link to be made between the study of planetary orbital stability and chaos theory noting that there is a large body of literature on the properties and significance of Lyapunov exponents (See Section 2.2.4). Although our results are given for the special case of the CRTBP, it is expected that it may be possible to augment the proposed Lyapunov exponent criterion to studies of planets in generalized stellar binary systems, which is strongly motivated by existing observational data as well as results expected from ongoing and future planet search missions.

3.1 Background

A classical problem within the realm of orbital stability studies for theoretical and observed planets in stellar binary systems is the circular restricted 3-body problem (CRTBP) (e.g., Szebehely 1967; Roy 2005). The CRTBP describes the motion of a body of negligible[1] mass moving in the gravitational field of the two more massive bodies considered here to be two stars. The stars move in circular orbits about the center of mass and their motion is not influenced by the third body, the planet. Furthermore, the initial velocity of the planet is assumed in the same direction as the orbital velocity of its host star, which is usually the more massive of the two stars.

The study of planetary orbital stability is timely for various astronomical reasons. First, although most planets are found in wide binaries, various cases of planets

[1]Negligible mass means that although the body's motion is influenced by the gravity of the two massive primaries, its mass is too low to affect the motions of the primaries.

in binaries with separation distances of less than 30 AU have also been identified (e.g., Patience et al. 2002; Eggenberger et al. 2004; Eggenberger & Udry 2010, and references therein) along with newly established circumbinary cases (e.g., Doyle et al. 2011; Welsh et al. 2012). Second, many more cases of planets in stellar binary systems are expected to be discovered noting that binary (and possibly multiple) stellar systems occur in high frequency in the local Galactic neighborhood (Duquennoy & Mayor 1991; Lada 2006; Raghavan et al. 2006). Moreover, orbital stability studies of planets around stars, including binary systems, are highly significant in consideration of ongoing and future planet search missions (e.g., Catanzarite et al. 2006; Cockell et al. 2009).

The CRTBP has been studied in detail by Dvorak (1984), Dvorak (1986), Rabl & Dvorak (1988), Smith & Szebehely (1993), Pilat-Lohinger & Dvorak (2002), and Mardling (2008). It has also been the focus of the previous papers in this series. In Paper I, Eberle et al. (2008) obtained the planetary stability limits using a criterion based on Jacobi's integral, Jacobi's constant, and inherently the zero velocity surfaces. The method, also related to the concept of Hill stability (Roy 2005), showed that orbital stability can be guaranteed only if the initial position of the planet lies within a well-defined limit determined by the mass ratio of the stellar components. Additionally, the stability criterion was found to be also related to the borders of the "zero velocity contour" (ZVC) and its topology assessed by using a synodic coordinate system regarding the two stellar components.

In Paper II, Eberle & Cuntz (2010b) followed another theoretical concept based on the hodograph eccentricity criterion. This method relies on an approach given by differential geometry that analyzes the curvature of the planetary orbit in the synodic coordinate system. The centerpiece of this method is the evaluation of the effective time-dependent eccentricity of the orbit based on the hodograph in rotating

coordinates as well as the calculation of the mean and median values of the eccentricity distribution. This approach has been successful in mapping quasi-periodicity and multi-periodicity for planets in binary systems. It has also been tested by comparing its theoretical predictions with work by Holman & Wiegert (1999) and Musielak et al. (2005) in regard to the extent of the region of orbital stability in binary systems of different mass ratios.

Previously, the work by Eberle & Cuntz (2010b) dealt with the assessment of short-time orbital stability, encompassing timescales of 10^3 yrs or less. One of the findings was the identification of a quasi-periodic region in the stellar mass and distance (μ, ρ_0) parameter space (see Section 3.2). Due to the relatively short timescales considered in the previous study, there is a strong motivation to revisit the onset of orbital instability using longer timescales and different types of methods. The focus of this part of the dissertation is the analysis of orbital stability by Lyapunov exponents, which are among the most commonly used numerical tools to investigate chaotic behavior of different dynamical systems (e.g., Hilborn 1994). The exponents have already repeatedly been used in orbital mechanics studies of, e.g., the Solar System (e.g., Lissauer 1999; Murray & Holman 2001). For example, Lissauer (1999) discussed the long-term stability of the eight Solar System planets, while also considering previous studies. He concluded that the Solar System is most likely astronomically stable, in the view of the limited life time of the Sun; however, the orbits of Pluto and of many asteroids may become unstable soon after the Sun becomes a white dwarf.

The numerical procedure of computing the Lyapunov exponents has been developed by Wolf et al. (1985) based on previous work by Benettin et al. (1980). Hence, the main objective of this part of the dissertation is to establish the Lyapunov exponent criterion and verify it by performing the power spectra analysis (e.g., Hilborn

1994) as well as by comparing the obtained results to those presented in Paper I and II. Our newly established criterion is then used to investigate stability of planetary orbits in stellar binary systems (approximated here as the CRTBP) of different masses and distance ratios.

3.2 Basic equations

In the following, I consider the so-called coplanar CRTBP (e.g., Szebehely 1967; Roy 2005), which I will define as follows. Two stars are in circular motion about their common center of mass and their masses are much larger than the mass of the planet. In this case, the planetary mass is assumed to be 1×10^{-6} of the mass of the star it orbits; also note that the planetary motion is constrained to the orbital plane of the two stars. Moreover, it is assumed that the initial velocity of the planet is in the same direction as the orbital velocity of its host star, which is the more massive of the two stars, and that the starting position of the planet is to the right of the primary star (3 o'clock position), along the line joining the binary components.

Following the conventions described by Eberle et al. (2008), I write the equations of motion in terms of the parameters μ and ρ_0 with μ and $\alpha = 1 - \mu$ being related to the ratio of the two stellar masses M_1 and M_2 (see Section 2.1.2). Moreover, R_0 denotes the initial distance of the planet from its host star, the more massive of the two stars with mass M_1, whereas D denotes the distance between the two stars, allowing us to define ρ_0. In addition, I use a rotating reference frame, which also gives rise to Coriolis and centrifugal forces. In order to conform to the prescribed notation

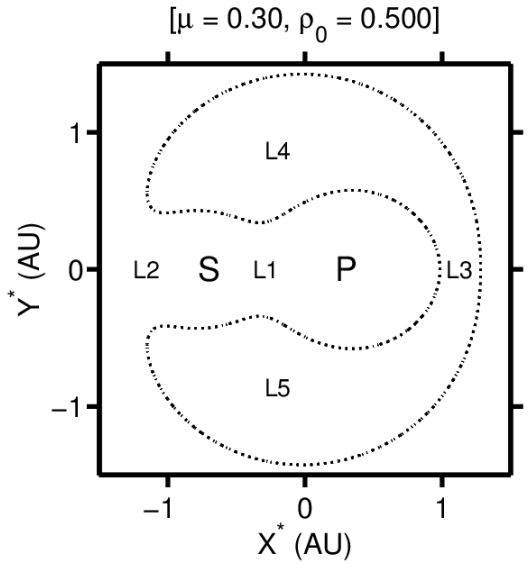

Figure 3.1. Locations of the Lagrange points L1, L2, L3, L4, and L5 as used in the CRTBP. The label P denotes the primary star and the label S denotes the secondary star.

a simple variable substitution is used $(\xi, \eta, \zeta, \dot{\xi}, \dot{\eta}, \dot{\zeta})^* = (x, y, z, u, v, w)^*$, respectively, and thus equations of motion are given as:

$$\dot{x} = u, \tag{3.1}$$

$$\dot{y} = v, \tag{3.2}$$

$$\dot{z} = w, \tag{3.3}$$

$$\dot{u} = 2v + x - \alpha\frac{x-\mu}{r_1^3} - \mu\frac{x+\alpha}{r_2^3}, \tag{3.4}$$

$$\dot{v} = -2u + y - \alpha\frac{y}{r_1^3} - \mu\frac{y}{r_2^3}, \tag{3.5}$$

$$\dot{w} = -\alpha\frac{z}{r_1^3} - \mu\frac{z}{r_2^3}, \tag{3.6}$$

where

$$\mu = \frac{M_2}{M_1 + M_2}, \tag{3.7}$$

$$\alpha = 1 - \mu, \tag{3.8}$$

$$r_1^2 = (x - \mu)^2 + y^2 + z^2, \tag{3.9}$$

$$r_2^2 = (x + \alpha)^2 + y^2 + z^2, \tag{3.10}$$

$$\rho_0 = \frac{R_0}{D}. \tag{3.11}$$

The variables in the above equations describe the position of the planet, which in essence constitutes a test particle, within a synodic coordinate system. Its position is defined in Cartesian coordinates $\{x,\ y,\ z\}$. I denote the time derivative or velocity of a coordinate using the dot notation $\left\{\dot{x} = \frac{\mathrm{dx}}{\mathrm{dt}}\right\}$. I also represent the set of second order differential equations, the equations of motion, by a set of first order differential equations (see Section 2.2.2). The velocity is defined by the coordinates $\{u,\ v,\ w\}$ whose time derivatives are the accelerations. By defining the mass ratio and using normalized coordinates, I can then define the distances $\{r_1,\ r_2\}$ with reference to the location of the stars in the rotating coordinate system. This particular convention assumes that $GM = 1$ such that the above equations can be described in the same manner as Equations 2.11, 2.12, and 2.13.

I enumerate the co-linear Lagrange points (positions of zero potential) in the synodic frame by the order of which the ZVC opens. The point between the stars opens first; therefore, I denote it as L1. The point to the left of the star that does not host the planet opens second; thus, I denote it L2. The point to the right of the star hosting the planet opens third and it is denoted L3. The two Trojan Lagrange points which are of lesser importance to our study are L4 and L5 (see Figure 3.1).

3.2.1 Lyapunov exponents

A fundamental difference between stable and unstable planetary orbits is that two nearby trajectories in phase space will diverge as power law (usually linear) for the former and exponentially for the latter. The parameter that is used to measure this rate of divergence is called Lyapunov exponent as it was originally introduced by Lyapunov (1907); see also Baker & Gollub (1990). For more details concerning Lyapunov exponents and the properties see Section 2.2.4.

Specific applications of the Lyapunov exponents to the circular restricted 3-body problem were discussed by many authors, including Gonczi & Froeschle (1981), Jefferys & Yi (1983), Lecar et al. (1992), Milani & Nobili (1992), Smith & Szebehely (1993), Murray & Holman (2001), and others. Some of these authors also considered the so-called Lyapunov time, which measures the e-folding time for the divergence of the nearby trajectories. It should be noted that the Lyapunov time is not well-defined for the cases when close encounters between a planet and one of the stars occurs or when the planet is ejected from the system (Lissauer 1999). Thus a special caution will be taken with this concept.

The previously obtained results clearly show that the Lyapunov exponents can be calculated for the case of the CRTBP considered in this dissertation, for which the degrees of freedom are $2n = 6$. This requires a state vector for the system containing 6 elements. Details about the nature of the state vector and the calculation Lyapounov exponents are given in Appendix B. From the equations of motion, the Jacobian **J** can be determined, which will be the foundation of how the Lyapunov exponents will be determined (see Section 2.2.3. In addition, the nature of this Jacobian will elude to certain properties of the Lyapunov exponents.

It is well known that the largest Lyapunov exponent is sufficient to determine the magnitude of the chaos in a system (e.g., Wolf et al. 1985). Considering this

fact, the presented study will consider only the effect that the maximum Lyapunov exponent because it will show the greatest effect of chaos on the system. This provides the motivation for examining how large the maximum Lyapunov exponent can be before it would introduce enough chaos to affect the stability of the CRTBP.

3.3 Results and discussion

To investigate the parameter space of the CRTBP, I performed numerical simulations for stellar mass ratios from $\mu = 0.0$ to 0.5 in increments of 0.01. A Yoshida sixth order symplectic integration scheme was used (e.g., Yoshida 1990). As a measure of the precision of the integration scheme, a time step of $\epsilon = 10^{-4}$ years (yrs) is used for the individual cases where in this context yrs is normalized relative to the binary period. However, for producing plots of the entire parameter space a time step of $\epsilon = 10^{-3}$ yrs was adopted as the smaller time step did not noticeably enhance the quality of the plots. The order of error in energy for each time step was 10^{-14} and 10^{-10}, respectively. I performed simulations for different time limits, which range from 10 to 10^5 yrs in increments of powers of 10. I also performed case studies with time limits of 10^6 and 10^7 yrs, although significant changes did not occur at those longer time scales. By using different time scales I was able to estimate when certain phenomena would occur and ascertain how those phenomena will affect other regions over longer periods of time.

I display runs for selected initial conditions (i.e., starting distances ρ_0 of the planet from the stellar primary) corresponding to $\mu = 0.3$ in Figures 3.2 to 3.4 and to $\mu = 0.5$ in Figures 3.5 to 3.7. In Figures 3.2 to 3.7, I first present the planetary orbits in the synodic coordinate system (X^*, Y^*). Secondly in each figure, the Lyapunov spectra of the same simulations are shown using a logarithmic scale for the Y^*-axis. Lastly in each figure, the time series power spectrum of the simulations are shown with

their normalized amplitudes. The power spectra were obtained through the usage of a FFT subroutine in Matlab® that uses the X*-component separation distance as a function of time and converts the output frequencies to periods (see Section 2.2.1 for details). The selected starting distance ratios ρ_0 of the planet are 0.355, 0.474, 0.595 for $\mu = 0.3$ and 0.290, 0.370, 0.400 for $\mu = 0.5$. Note that ρ_0 indicates the relative initial distance of the planet given as R_0/D, with $D = 1$ AU as the distance between the two stars and R_0 as the initial distance of the planet from its host star, the primary star of the binary system.

Using the method of Lyapunov exponents, I was able to verify and extend the methods described by Eberle et al. (2008) and Eberle & Cuntz (2010b). Absolute orbital stability can be more rigorously shown through the Lyapunov exponent method. It occurs when $\rho_0 < \rho_0^{(1)}$, where $\rho_0^{(1)}$ represents the point at which the initial condition result in a ZVC that opens at L1. For larger values of ρ_0, stability is not guaranteed due the behavior discussed by Eberle et al. (2008); this result is also consistent with our Lyapunov exponent criterion for orbital stability.

The main criterion for this orbital stability analysis is the Lyapunov exponent criterion, which is based here on the maximum Lyapunov exponent. From a theoretical point of view, an orbit is stable when all Lyapunov exponents are exactly zero. Obviously, this 'perfect' criterion for orbital stability will be very difficult to reach numerically because it would require an infinite simulation time. Due to finite simulation times, I obtain 3 positive and 3 negative Lyapunov exponents, and their sum becomes close to zero within the limits of our numerical simulations. Hence, in order to determine orbital stability numerically, I must look at the values of the three positive Lyapunov exponents at the beginning and at the end of our simulations. By comparing these values, I will determine whether the exponents decrease with time, and if so what is the rate of their decrease, or stay approximately constant in time.

Table 3.1. Maximum Lyapunov exponent study for the models of $\mu = 0.5$ at different time intervals.

ρ_0	MLE (10^2)	MLE (10^3)	MLE (10^4)	e_{median}	ZVC
0.25	8.7189E−2	1.1353E−2	1.0009E−3	0.20	...
0.29	1.0647E−1	9.5469E−3	9.9141E−4	0.45	L1
0.30	7.6275E+0*	...	...	0.67	L1
0.35	5.2937E+0*	...	...	0.82	L1
0.37	6.1946E+0*	...	...	0.98	L1
0.40	1.0675E−1	9.6613E−3	8.8900E−4	0.71	L1
0.43	2.8614E−1	2.9420E−1*	...	0.87	L1
0.50	7.9684E−1*	...	...	0.089	L1, L2, L3

Note: Elements without data indicate simulations that ended due to the energy criterion, thus representing planetary catastrophes. Elements with an asterisks (*) indicate that the simulation ended before the allotted time. Also, e_{median} represents the median of the eccentricity distribution obtained for the curvature of the planetary orbits in the synodic coordinate system (see Paper II). The last column indicates the Lagrange point(s) where the zero-velocity contour (ZVC) is open (see Paper I).

Using this information, I found the maximum Lyapunov exponent and adopted it as the primary indicator of orbital stability. Then I classify an orbit as stable if the initial value of the maximum Lyapunov exponent is below a certain threshold and if it decreases with a 'reasonable rate' (see below); otherwise, the orbit is classified as unstable. In our plots of Lyapunov spectra (see the second panels in Figures 3.2 to 3.7), I present all three positive Lyapunov exponents to clearly show their values and study how do they change in time.

In addition to the Lyapunov exponent criterion for orbital stability, I also use the so-called orbital energy criterion, which requires that the kinetic energy should not exceed twice that of the potential energy. This is evaluated in our numerical simulations during each time step. A failure of this criterion would imply a break in conservation of the Jacobi constant as detailed by Szebehely (1967) and shown

numerically by Table 3.2. It should also be noted that the cases presented in Table 3.2 are also presented in Figures 3.2 - 3.4.

There are two important points associated with this criterion. First, the systems are Hamiltonian, which means that their energy must be conserved. On the other hand, the fact that the energy conservation of the planet can be broken because I have neglected the effects of the 3$^{\rm rd}$ mass on the larger masses has already been discussed by Szebehely (1967). Second, even if the energy is only approximately conserved in our numerical simulations, I do request that the Jacobi constant remains constant, which is a required stability condition for CRTBP. To be consistent with this criterion (see also Paper I), I stop our numerical simulation once changes (even small) in the Jacobi constant occur; such cases are shown in Tables 3.3 and 3.1. The changes in Jacobi constant occur when the 3$^{\rm rd}$ approaches the ZVC. As a result the orbital velocity of the 3$^{\rm rd}$ mass approaches zero which removes the (u, v, w) terms from the equations of motion. Then the 3$^{\rm rd}$ mass embarks on a close approach with the primary star and previous simulations have shown that the instability begins due to these close approaches leading to ejection from the system.

Table 3.2. Values for the error in the Jacobi constant (JCE) for the models of $\mu = 0.3$ at different time intervals.

ρ_0	JCE($\frac{\tau}{4}$)	JCE($\frac{\tau}{2}$)	JCE($\frac{3\tau}{4}$)	JCE(τ)
0.355	1.0740E−10	2.4747E−10	1.2403E−10	1.8824E−10
0.474	1.4498E−10	9.7917E−11	3.7723E−11	1.0067E−11
0.595	8.9819E−13	5.2923E−13	5.2001E−13	7.1001E−6

Note: τ denotes the respective runtime of the simulation. I have shown the stable cases of $\rho_0 = 0.355$ and $\rho_0 = 0.474$, where $\tau = 10^5$ binary orbits and for the unstable case of $\rho_0 = 0.595$, $\tau = 150.64$ binary orbits.

Alike in the previous paper by Eberle et al. (2008), I have identified the same regions of orbital stability, instability, and domains of quasi-periodic orbital stability. A key difference, however, is that the orbit diagrams depicted in Figures 3.2 to 3.7 have been simulated for 10^5 years, whereas the corresponding figures in the previous paper have been simulated for only 10^3 years. The power spectra are shown to indicate how I determined the region of quasi-periodic orbital stability including the correct magnitude.

Table 3.3. Maximum Lyapunov exponent study for the models of $\mu = 0.3$ at different time intervals.

ρ_0	MLE (10^2)	MLE (10^3)	MLE (10^4)	e_{median}	ZVC
0.20	1.1099E−1	1.1493E−2	1.1446E−3	0.027	...
0.30	1.0322E−1	1.0103E−2	1.0691E−3	0.17	...
0.40	9.8084E−2	1.0050E−2	6.8986E−4	0.58	L1
0.474	7.7766E−2	9.4232E−3	9.2624E−4	0.75	L1, L2
0.50	8.5390E−2	9.2048E−3	7.9830E−4	0.85	L1, L2
0.595	1.5793E−1	1.4175E−1*	...	1.14	L1, L2, L3
0.60	8.9533E−1*	...	...	1.10	L1, L2, L3

Note: Elements without data indicate simulations that ended due to the energy criterion, thus representing planetary catastrophes. Elements with an asterisks (*) indicate that the simulation ended before the allotted time. Also, e_{median} represents the median of the eccentricity distribution obtained for the curvature of the planetary orbits in the synodic coordinate system (see Paper II). The last column indicates the Lagrange point(s) where the zero-velocity contour (ZVC) is open (see Paper I).

I analyze the case studies by classifying Figures 3.2, 3.3, 3.5, and 3.7 as stable candidate configurations. Three of the cases show similar behavior in the maximum Lyapunov exponent as shown in Figures 3.3b, 3.5b, and 3.7b. These Lyapunov spectra have a common trend by starting at a maximum value on the order of 10^{-1} and

converging, albeit slowly, to smaller orders of ten. Figure 3.3 shows a somewhat different behavior compared to the other cases in its class of stable candidates. This case establishes a quasi-periodic orbit, which illustrates a $(3:1)$ resonance in the power spectrum and reveals the same trend of stability in the Lyapunov exponent spectrum. Figure 3.2 shows an additional variance in behavior due to the elevated nature of the maximum Lyapunov exponent. This shows that a limited amount of chaos exists in the system while remaining stable for the full simulation time. Also this case demonstrates a $(3:1)$ resonance in the power spectrum.

In contrast, Figure 3.4 demonstrates a case of instability. The Lyapunov spectrum shows a different nature than that of the preceding cases. Figure 3.4b begins at a maximum value greater than 1 and converges to a value between 10^{-1} and 1. By establishing the preceding cases as stable cases, I can contrast the final values of the corresponding maximum Lyapunov exponents. The unstable case of Figure 3.4b is two orders of magnitude greater than the stable cases given in Figures 3.3b, 3.5b, and 3.7b. However, in comparison with Figure 3.2b there is only a difference of one order of magnitude.

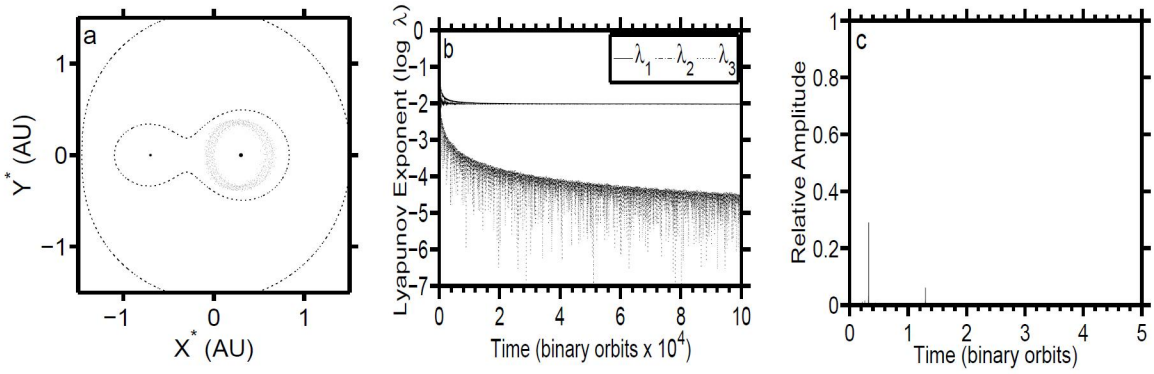

Figure 3.2. Case study for the initial planetary distance ratio $\rho_0 = 0.355$ with planetary orbit in the synodic coordinate system, Lyapunov spectrum, and power spectrum. The stellar mass ratio is $\mu = 0.3$.

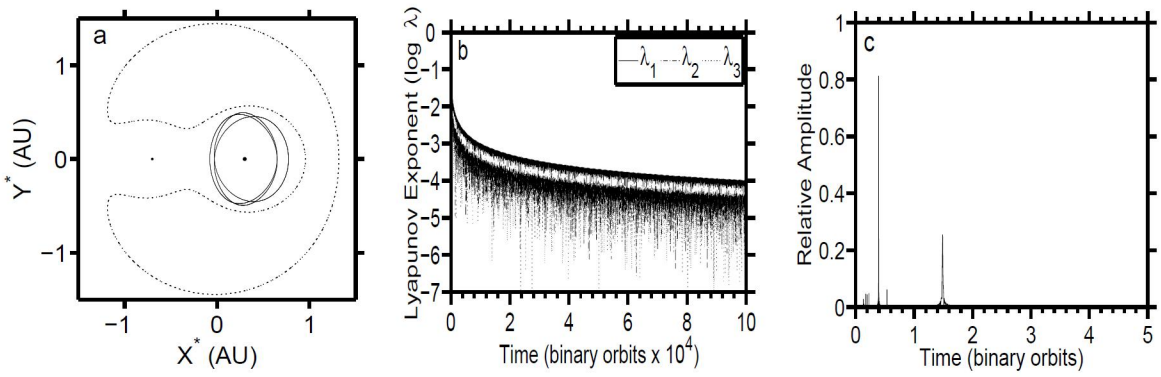

Figure 3.3. Case study for the initial planetary distance ratio $\rho_0 = 0.474$ with planetary orbit in the synodic coordinate system, Lyapunov spectrum, and power spectrum. The stellar mass ratio is $\mu = 0.3$.

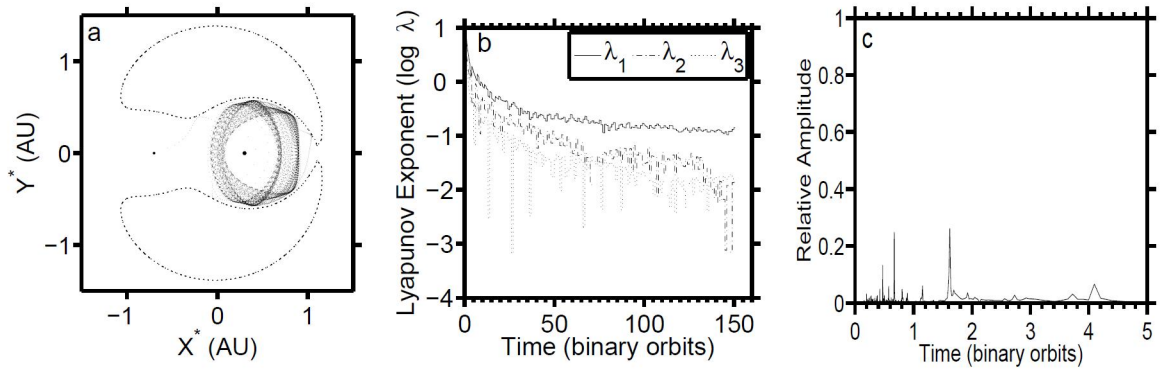

Figure 3.4. Case study for the initial planetary distance ratio $\rho_0 = 0.595$ with planetary orbit in the synodic coordinate system, Lyapunov spectrum, and power spectrum. The stellar mass ratio is $\mu = 0.3$.

Figure 3.6 has been examined in a similar manner. Having already classified Figure 3.5 and 3.7 as stable configurations, I emphasize that they reveal similar trends in the maximum Lyapunov exponent as given by Fig. 3.3. However, Figure 3.6 shows a different orbit diagram and is described by a maximum Lyapunov exponent that gives the outcome of instability. This case conveys a much noisier power spectrum

along with a maximum Lyapunov exponent on the order of 1 or greater. Finer detail is illustrated in Table 3.2 and Table 3.3. Particularly Table 3.3 shows a boundary in the maximum Lyapunov exponent where values near 0.1 and smaller for the first 100 years tend toward stability.

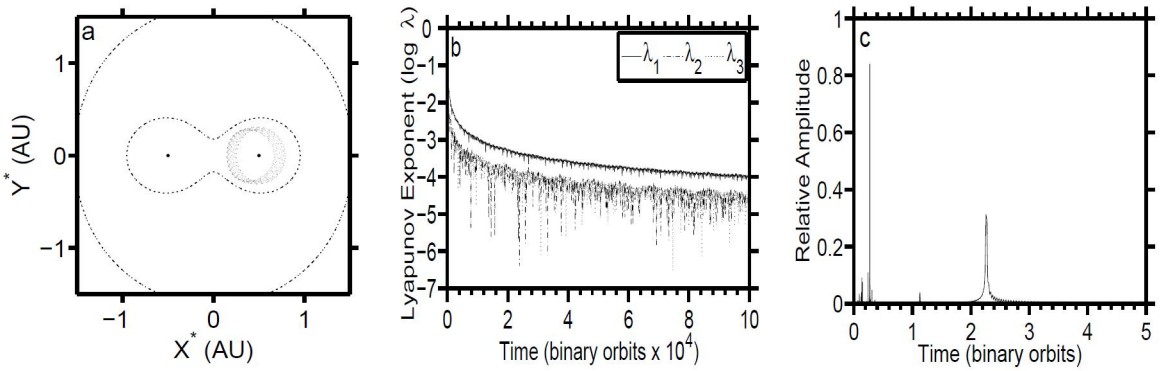

Figure 3.5. Case study for the initial planetary distance ratio $\rho_0 = 0.290$ with planetary orbit in the synodic coordinate system, Lyapunov spectrum, and power spectrum. The stellar mass ratio is $\mu = 0.5$.

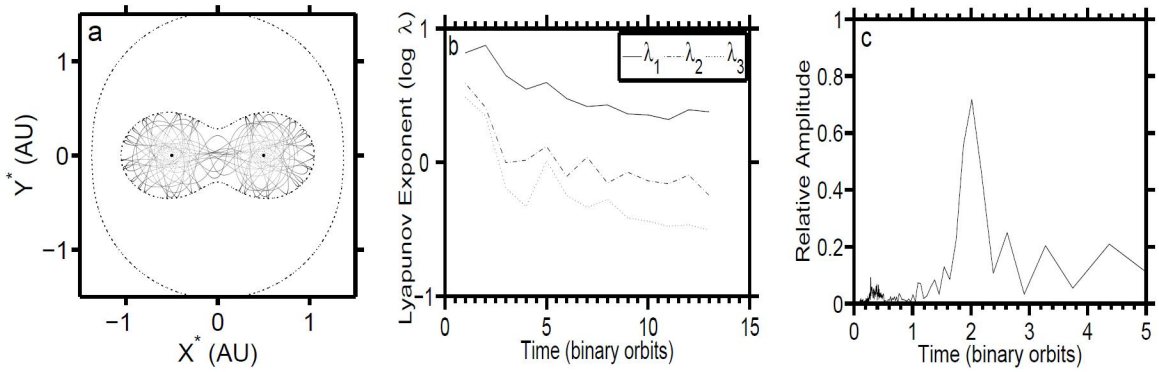

Figure 3.6. Case study for the initial planetary distance ratio $\rho_0 = 0.370$ with planetary orbit in the synodic coordinate system, Lyapunov spectrum, and power spectrum. The stellar mass ratio is $\mu = 0.5$.

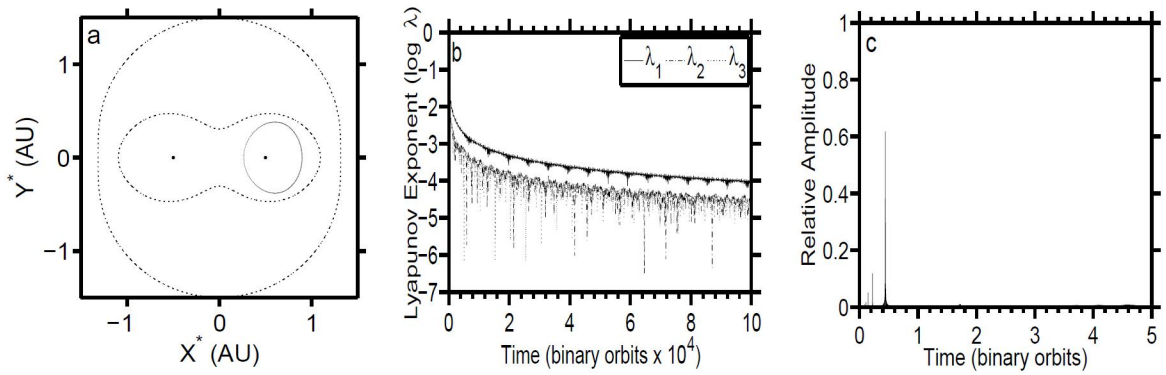

Figure 3.7. Case study for the initial planetary distance ratio $\rho_0 = 0.400$ with planetary orbit in the synodic coordinate system, Lyapunov spectrum, and power spectrum. The stellar mass ratio is $\mu = 0.5$.

Figure 3.8 conveys the bigger picture for the parameter space. It represents contour plots of the maximum Lyapunov exponent with respect to the (μ, ρ_0) parameter space in linear and logarithmic scale. The crosses depict initial conditions for runs that prematurely ended due to the orbital energy criterion. This demonstrates where the regions of instability occur as reflected by the respective color coded scale of the maximum Lyapunov exponent. Comparing Figure 3.8 (left) to the previous result by Eberle et al. (2008), it can be seen that the main regions of stability remain the same. Other noteworthy features include that the instability islands present near $\rho_0 = 0.4$ have grown as the simulation time has been increased as well as the existence of a plateau near $\rho_0 = 0.48$. The color scale in Figure 3.8 (left) has a maximum color of dark red at a maximum Lyapunov exponent of 0.15. Some regions appear to be colored black; however, this does not correspond to the adopted color scale as it is caused by the finite contour line width due to the close proximity of the lines. Therefore, the plateau has a peak value of maximum Lyapunov exponent near 0.15. Considering the diagrams in Figure 3.3, I conclude that a region of quasi-periodicity and resonance exist on this plateau.

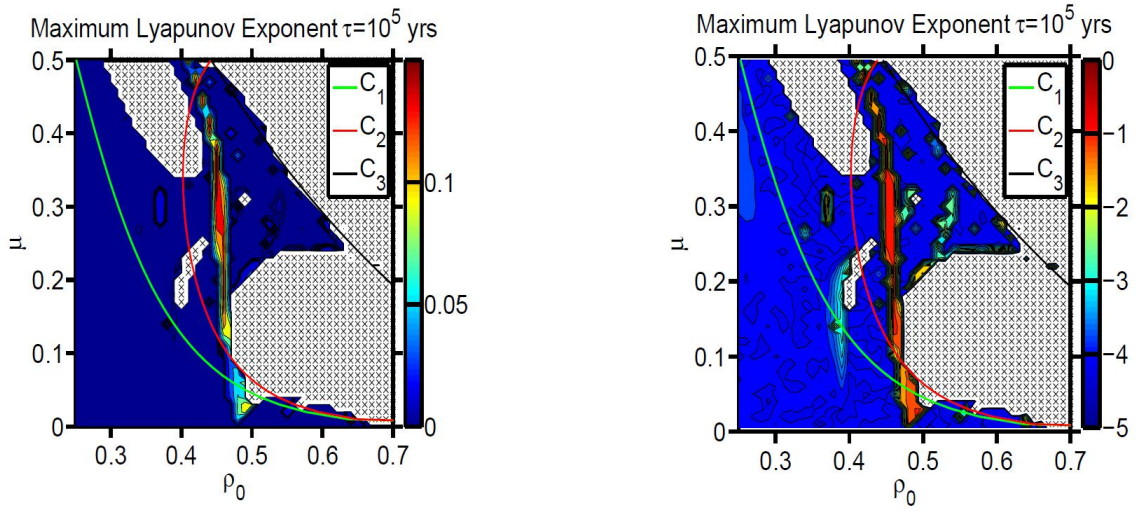

Figure 3.8. The maximum Lyapunov exponent (color coded) is depicted for various mass ratios μ and initial conditions ρ_0 using a *linear* scale (left) or a *logarithmic* scale (right) where $-n$ corresponds to 10^{-n}. The crosses denote cases where the simulation was terminated due to the planet being captured by one of the stars or being ejected from the system. The green, red, and black curves represent the initial conditions that cause the ZVC to intersect L1, L2, and L3, respectively. (Quarles et al. 2011).

Figure 3.8 (right), the contour plot in logarithmic scale, is shown to display some of the finer details pertaining to structure inside the stability regions. The blue-green colored regions demonstrate areas of possible stable chaos that are hidden in Fig. 3.8 (left). Some other smaller contours are also produced in the stability region, but the color coding in general shows little change, which is partially due to the chosen spacing between contours. The average difference in height between these levels is -0.15; on the logarithmic scale, it indicates a change by a factor of 1.41 in the maximum Lyapunov exponent.

Inspecting Figure 3.8 also allows a comparison with previous results, particularly results of Paper I. There it was shown that absolute orbital stability occurs when $\rho_0 < \rho_0^{(1)}$, where $\rho_0^{(1)}$ represents the point at which due to the initial condition the ZVC opens at L1. This condition is represented by the line of C_1 in Figure. 3.8.

It is evident that the Lyapunov exponent criterion is almost perfectly consistent with this condition. Additionally, as discussed in Paper I and references therein, stability cannot be expected if $\rho_0 > \rho_0^{(3)}$ because now the ZVC is open at L1, L2, and L3. This finding is also almost perfectly reflected through the behavior of the maximum Lyapunov exponent as a orbital stability criterion. Both panels of Figure 3.8 show no stability regions on the right side of C_3, which is reflective of the opening of the ZVC at Lagrange points L1, L2, and L3.

3.4 Summary

I present a detailed case study of the CRTBP with analysis through the usage of the Lyapunov exponents. I am able to characterize stability limits based on the value of the maximum Lyapunov exponent at the end of each simulation. Cases where the maximum Lyapunov exponent exceeds a value of 0.15 indicate that the planet will experience an event that causes the orbital velocity to decrease. These events include intersecting a Lagrange point or the ZVC. After such an event, the planet will experience a series of near misses with one of the stars in the binary system leading to overall instability. Chaos theory and the concept of Lyapunov time prevent us from predicting exactly when the planet will be ejected. Using Lyapunov time as a measure of the length of predictive time, I can show that this relationship is proportional to the inverse of the maximum Lyapunov exponent. Using the critical value of 0.15 (Quarles et al. 2011), the unstable systems will lose predictability within $(0.15)^{-1} = 6\frac{2}{3}$ years or less. After that time, it is unknown when the planet will be ejected as this could take many multiples of the Lyapunov time to occur.

The method also shows evidence of a region of quasi-periodicity. This is a region where the maximum Lyapunov exponent remains near the critical value without exceeding that value. This is shown for cases simulated for 10^5 years. Based on this

time scale, I can conclude that our quasi-periodic plateau represents a region of stable or quasi-stable chaos (Quarles et al. 2011). This is due to the Lyapunov times being much less than the simulation run time. The chaos is shown through the value of the maximum Lyapunov exponent, whereas the stability is shown through the motion of the planet over longer time scales. The lack of near miss events and encounters with regions of decreasing velocity prohibit the planet from becoming orbitally unstable.

Comparisons to previously established criteria for stability show that these results are consistent with previously obtained stability limits (e.g., Holman & Wiegert 1999; Musielak et al. 2005; Cuntz et al. 2007; Eberle et al. 2008; Eberle & Cuntz 2010b). In Eberle et al. (2008), Paper I, the onset of instability was related to the topology of the ZVC, whereas in Eberle & Cuntz (2010b), Paper II, it was shown that onset of orbital instability occurs when the median of the effective eccentricity distribution exceeds unity. Both results are consistent with the findings of Paper III, i.e., the inspection of the maximum Lyapunov exponent. However, the latter offers the advantage to link the study of orbital instability for the CRTBP (and any subsequent generalization, if available) to chaos theory, including the evaluation of different types of chaos.

Although these results have been obtained for the special case of the CRTBP, I expect that it may also be possible to augment the findings to planets in generalized stellar binary systems. Desired generalizations should include studies of the ER3BP (e.g., Pilat-Lohinger & Dvorak 2002; Szenkovits & Makó 2008) as well as of planets on inclined orbits (Dvorak et al. 2007), noting that especially the former have important applications to real existing systems in consideration of the identified stellar and planetary orbital parameters (Eggenberger & Udry 2010).

CHAPTER 4

STUDY OF RESONANCES FOR THE RESTRICTED 3-BODY PROBLEM

The aim of this study is to identify and classify mean-motion resonances (MMRs) for the coplanar circular restricted three-body problem (CRTBP) for mass ratios between 0.10 and 0.50. The methods include the usage of maximum Lyapunov exponent, which is used as an indicator for the location of the resonances, the Fast Fourier Transform (FFT) used for determining what kind of resonances are present, and the inspection of the orbital elements to classify the periodicity. Here I show that the 2:1 resonance occurs the most frequently. Among other resonances, the 3:1 resonance is the second most common, and furthermore both 3:2 and 5:3 resonances occur more often than the 4:1 resonance. Moreover, the resonances in the coplanar CRTBP are classified based on the behavior of the orbits. I show that orbital stability is ensured for high values of resonance (i.e., high ratios) where only a single resonance is present. The resonances attained are consistent with the previously established resonances for the Solar System, i.e., specifically, in regards to the asteroid belt. Previous work in this field has employed digital filtering and Lyapunov characteristic exponents to determine stochasticity of the eccentricity, which is found to be consistent with my usage of Lyapunov exponents as an alternate approach based on varying the mass ratio instead of the eccentricity. These results are expected to be of principal interest to future studies, including augmentations to observed or proposed resonances, of extra-solar planets in binary stellar systems.

4.1 Background

The circular restricted three-body problem (CRTBP) has been considered in orbital mechanics for more than two centuries, and its numerous applications to describe the motion of planets, asteroids and artificial satellites in the Solar System are well-known (Szebehely 1967; Dvorak 1984, 1986; Rabl & Dvorak 1988; Smith & Szebehely 1993; Murray & Dermott 1999 and references therein). More recently, the study of the CRTBP has been motivated as a testbed for investigations of the orbital stability of extra-solar planetary systems around single stars as well as planets in stellar binary systems.

Extensive studies of orbital stability in the CRTBP have been performed by many authors, who used tools ranging from the Jacobi constant (e.g., Cuntz, Eberle, & Musielak 2007; Eberle, Cuntz, & Musielak 2008), a hodograph-based method (Eberle & Cuntz 2010b) and Lyapunov exponents (e.g., Gonczi & Froeschle 1981; Jefferys & Yi 1983; Lecar, Franklin, & Murison 1992; Milani & Nobili 1992; Smith & Szebehely 1993; Lissauer 1999; Murray & Holman 2001; Quarles, Eberle, Musielak, & Cuntz 2011). There have also been inquiries into different numerical methods specifically designed to study the orbital stability problem (e.g., Yoshida 1990; Holman & Wiegert 1999; David et al. 2003; Musielak et al. 2005). Some recent studies involve spacecraft trajectories to the Lagrangian point L_3 (Tantardini et al. 2010) and the stability analysis of artificial equilibrium points in the CRTBP (Bombardelli & Peláez 2011).

The origin and nature of mean-motion resonances (MMRs) in the CRTBP, particularly for cases of low mass ratios, have also been studied, and the role of MMRs in orbital stability has been investigated in detail. Hadjidemetriou (1993) identified three (2:1, 3:1 and 4:1) main MMRs in the Sun-Jupiter and asteroid system. Extensive studies of MMRs, with extensions to the elliptic restricted three-body problem (ERTBP), have been performed by Ferraz-Mello (1994); Nesvorný et al. (2002);

Pilat-Lohinger & Dvorak (2002); Haghighipour et al. (2003); Vela-Arevalo & Marsden (2004); Mardling (2008); Szenkovits & Makó (2008). It has been shown that the main difference in orbital stability between stable and unstable systems with MMRs is that the latter involves more than one resonance, and that the existence of two or more resonances leads to their overlap making some orbits unstable (e.g., Mudryk & Wu 2006; Mardling 2008).

This type of work is also motivated by earlier results on various extra-solar star–planet systems. Previously, Marcy et al. (2001) and Lee et al. (2006) discovered two planets in 2:1 orbital resonance about the star GJ 876 and HD 82943, respectively. Other interesting cases include the 3:1 MMR in the five planet system of 55 Cnc, occurring between the inner planets 55 Cnc c and 55 Cnc b (Marcy, Butler, Fischer, Laughlin, Vogt, Henry, & Pourbaix 2002; Ji, Kinoshita, Liu, & Li 2003; Novak, Lai, & Lin 2003) and the 3:2 MMR in the system of HD 45364 (Correia et al. 2009). Furthermore, the two outer planets of 47 UMa are found to be in a 5:2 resonance (Fischer et al. 2002). This system is of particular interest as it is hosting two gas planets with a similar mass ratio than that between Jupiter and Saturn, which are orbiting a star of similar spectral type as the Sun. However, the gas planets in this system are relatively close to the zone of habitability; therefore, they adversely affect the astrobiological significance of the system (Noble, Musielak, & Cuntz 2002; Goździewski 2002; Cuntz, von Bloh, Bounama, & Franck 2003).

To identify MMRs in the CRTBP, particularly for small mass ratios, or in the elliptical restricted three-body problem (ERTBP) several different methods have been developed (see Section 2.2.5). So far, the developed methods have mainly been applied to identify MMRs that affect the structure and evolution of the asteroid belt. This means that the identified MMRs were found for the specific mass ratios of the Solar System primaries (Sun-Jupiter and Jupiter-Saturn). However, there is significant

ongoing work as well as the need for future work pertaining to extra-solar planetary systems, which is self-evident from the recent discoveries by the Kepler space telescope of the circumbinary planets Kepler-16, Kepler-34 and Kepler-35 (Doyle et al. 2011; Welsh et al. 2012).

The main purpose of this investigation is to identify and classify MMRs in the CRTBP for a broad range of mass ratios of the stellar components. Our method of finding resonances is based on the maximum Lyapunov exponent, which is used as an indicator for the location of resonances once the masses of the two massive bodies are specified. Then, a Fast Fourier Transform (FFT) is used to determine what kind of resonances exist. Thereafter, periodicity is determined through the inspection of the orbit diagrams and osculating semi-major axis of representative cases. Future applications of enhanced versions of our results will involve (1) extra-solar planetary systems around single stars (2) exomoons in star–planet systems, and (3) planets in stellar binary systems. Currently, the ideal application of the CRTBP to planets in stellar binary systems remains undetected. Therefore, specific applications are beyond the scope of this work that is fully devoted to the problem of finding and classifying MMRs in the CRTBP. Nonetheless, the present study is an important step toward envisioned future investigations motivated by existing and anticipated discoveries of planets through ongoing and future search missions.

4.2 Theoretical Approach

I consider the CRTBP with objects of masses M_1, M_2 and M_3; note that mass M_3 is assumed to be negligible compared to M_1 and M_2. From a mathematical point of view, the problem is described by equations of motion in synodic coordinates (see Section 3.2 for details).

In this investigation, I study the manifestations of resonances in numerical solutions in the physical plane (x, y) for the Copenhagen case ($\mu = 0.5$) and the special cases $\mu = 0.1$, 0.2, 0.3, and 0.4. I vary the parameter ρ_0, which is defined by the ratio of the initial distance of mass M_3 from the host mass M_1, given as R_0, and the separation distance, D, between the two larger (M_1 and M_2) masses, i.e., $\rho_0 = R_0/D$. As an initial condition, the object of mass M_3 starts at the 3 o'clock position with respect to the massive host star, M_1. I have also assumed a circular initial velocity for M_3. The numerical simulations are performed using a sixth order symplectic integration method with a constant time step of 10^{-3} binary periods per step (Yoshida 1990). Unstable systems are confirmed using a sixteenth order Gragg-Burlisch-Stoer integration method with the aforementioned constant time step as an initial guess (Grazier et al. 1996). Additionally, I use fitting formulas (Holman & Wiegert 1999) to confirm the numerically determined stability limits.

In order to determine resonances, I utilize the method of Lyapunov exponents (e.g., Nesvorný & Morbidelli 1998; Nesvorný et al. 2002). In this method, I consider a constant mass ratio μ, calculate the spectrum of Lyapunov exponents, and monitor the maximum Lyapunov exponent with respect to the parameter ρ_0. Although I calculate the full spectrum of Lyapunov exponents, this discussion will be limited to the maximum Lyapunov exponent for the reasons explained elsewhere (e.g., Quarles et al. 2011, and Section 3.3). The maximum Lyapunov exponent is used as an indicator of the maximum role that a particular resonance will have on the system. This provides a way of inspecting how the maximum Lyapunov exponent changes in response to small variations in the initial condition ρ_0. Additionally, I use the fast Lyapunov indicator (e.g., Froeschlé, Lega, & Gonczi 1997; Lega & Froeschlé 2001) to estimate the extent of weak chaotic or ordered motion.

After choosing a value of μ and performing calculations of the maximum Lyapunov exponent, a FFT is used to produce a periodogram, and then take ratios of the periods in the periodogram to determine what kind of resonances (if any) are present. Using the Lyapunov exponent with a periodogram provides a method of quickly identifying regions of possible resonances rather than invoking a brute force method of performing a FFT over all possible values of ρ_0. The ratios of the periods in the periodogram are taken with respect to the period axis; however, the strength of the peaks are not considered. In the tables, I provide the periods of the three strongest peaks in the periodogram and label them as Peak 1, Peak 2, and Peak 3 in ascending order. Resonance 1 denotes the closest rational expression of the ratio of Peak 2 to Peak 1, whereas Resonance 2 denotes the closest rational expression of Peak 3 to Peak 1. More peaks may be possible in the periodograms; however, the induced instability greatly overwhelms the necessity for investigating them. There are also elements in the tables without data (shown by ellipsis). They indicate simulations where a Peak 3 could not be discriminated against the background; therefore, a value for Resonance 2 could not be determined. In this study I am investigating the range of ρ_0 beginning at $\rho_0 = 0.250$ and ending at $\rho_0 = 0.700$ in increments of 0.001 for a given value of μ.

4.3 Results and Discussion

4.3.1 Case studies

I consider five different cases of fixed mass ratio μ, starting at $\mu = 0.1$ and proceeding in increments of 0.1. Each case presents a different aspect of the problem but together the combined results will help to identify and classify resonances in the coplanar CRTBP for relatively large values of μ. For each case, I start with the

Table 4.1. Resonances for selected values of ρ_0 with an elevated maximum Lyapunov exponent given for $\mu = 0.1$. The different orbital types are classified as Periodic, Quasi-Periodic, and Non-Periodic, and are denoted by P, QP, and NP, respectively.

ρ_0	Peak 1	Peak 2	Peak 3[a]	Resonance 1	Resonance 2[a]	Orbital Type
0.394	0.3494	1.045	...	3:1	...	P
0.457	0.4693	0.8827	1.001	15:8	17:8	P
0.471	0.4832	0.9671	...	2:1	...	P

[a]Note: Elements without data indicate simulations that did not have a Peak 3 in the periodogram; therefore, a value for Resonance 2 could not be determined.

Table 4.2. Same as Table 4.1 but for $\mu = 0.2$.

ρ_0	Peak 1	Peak 2	Peak 3	Resonance 1	Resonance 2	Orbital Type
0.334	0.2715	1.087	...	4:1	...	P
0.391	0.3631	1.143	...	22:7	...	QP
0.399	0.3756	1.127	...	3:1	...	QP
0.450	0.4636	0.7716	1.162	5:3	5:2	QP
0.458	0.4769	0.815	1.151	12:7	12:5	QP
0.482	0.5153	1.031	...	2:1	...	P
0.491	0.3457	0.5186	1.037	3:2	3:1	QP

Table 4.3. Same as Table 4.1 but for $\mu = 0.3$.

ρ_0	Peak 1	Peak 2	Peak 3	Resonance 1	Resonance 2	Orbital Type
0.355	0.3267	1.297	...	4:1	...	QP
0.370	0.3503	1.357	...	31:8	...	QP
0.454	0.4743	1.448	...	3:1	...	QP
0.471	0.4996	1.500	...	3:1	...	P
0.483	0.5121	0.7680	1.537	3:2	3:1	QP
0.488	0.5244	0.8034	1.511	3:2	23:8	NP
0.493	0.5236	0.8278	1.495	14:3	14:5	QP
0.530	0.5906	0.9875	1.472	5:3	5:2	QP
0.537	0.6016	1.017	1.475	5:3	22:9	QP

Table 4.4. Same as Table 4.1 but for $\mu = 0.4$.

ρ_0	Peak 1	Peak 2	Peak 3	Resonance 1	Resonance 2	Orbital Type
0.429	0.4456	1.995	...	9:2	...	QP
0.444	0.4726	1.732	...	11:3	...	QP
0.471	0.5236	1.580	...	3:1	...	QP
0.505	0.2958	0.5918	1.480	2:1	5:1	QP
0.507	0.2976	0.5953	1.473	2:1	5:1	QP
0.518	0.2046	0.3070	0.614	3:2	3:1	QP
0.521	0.2060	0.3090	0.618	3:2	3:1	QP

Table 4.5. Same as Table 4.1 but for $\mu = 0.5$.

ρ_0	Peak 1	Peak 2	Peak 3	Resonance 1	Resonance 2	Orbital Type
0.410	0.232	0.4639	...	2:1	...	P
0.426	0.251	0.5014	1.506	2:1	6:1	QP

parameter ρ_0 at the value 0.250 that is increased in increments of 0.001 up to a final value of $\rho_0 = 0.700$. I then show one plot and one table for each case of μ. In each plot, I distinguish between the stable cases, which continued for the full 10^5 binary orbits of simulation time by a solid line, and the unstable cases by dashed lines; the latter ended early due to the ejection of the planet from the system. Our criteria for ending each simulation are based on checking the error in the Jacobi constant and the value of the maximum Lyapunov exponent where high values of either imply a high probability for m_3 to be ejected from the system (Quarles et al. 2011). We also pursued numerical comparisons with an independent integration method to verify the integrity of the proposed outcome (see Section 4.2). These separate criteria provide a method for checking for instability and stability, as well as a measure for identifying chaos in the system. In the accompanying tables, I provide the values of ρ_0 where the maximum Lyapunov exponent is found to peak.

After the maximum Lyapunov exponent is calculated,the system is transformed pointwise from barycentric coordinates to Jacobi coordinates choosing the more massive body as reference point. I then perform a FFT using the time series data for that specific ρ_0. With this result, I obtain the Fourier spectrum and convert it to a corresponding periodogram. The resonances are determined by taking the ratio of periods for the strongest peaks. In the tables, we provide the computational results for the three strongest peaks, if available, for that value of ρ_0. The resonances are given as a ratio of the period of the small (M_3) mass to the period of the smaller binary (M_2) mass. For example, 4:1 would indicate that the small mass orbits four times in a single orbit of the smaller binary mass.

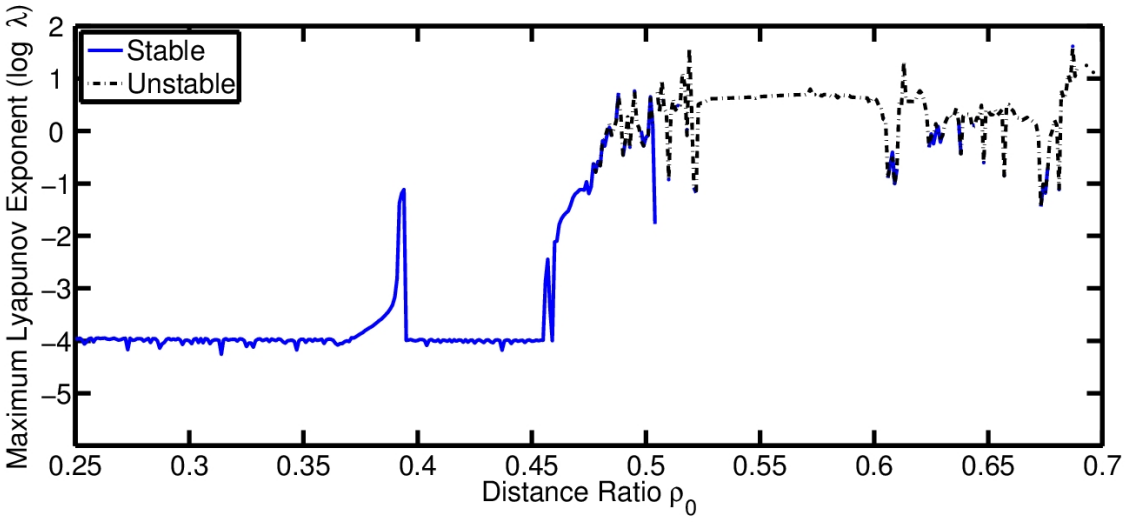

Figure 4.1. Maximum Lyapunov exponent is plotted versus the distance ratio ρ_0 for $\mu = 0.1$. The stable and unstable cases are denoted. (Quarles et al. 2012c).

The first case of $\mu = 0.1$ is depicted in Figure 4.1 with numerical results given in Table 4.1. This case illustrates a baseline of configurations where the second large (m_2) mass is not greatly perturbing the small (m_3) mass from $\rho_0 = 0.250$ to 0.350.

This provides a clear indication of where a possible resonance is not substantial enough to alter the orbit. However, the value of the maximum Lyapunov exponent peaks first at $\rho_0 = 0.394$. This indicates that the second large mass is at a specific geometric position allowing it to greatly perturb the motion of the small mass. The same feature occurs again at $\rho_0 = 0.457$ and 0.471. Note that the resonances associated with each peak in Figure 4.1 are not all the same; see Table 4.1. Moreover, we identify a large region of instability when ρ_0 is further increased, which is consistent with previous investigations (Eberle & Cuntz 2010b; Quarles et al. 2011).

The second case of $\mu = 0.2$ is depicted in Figure 4.2 and the relevant numerical values are presented in Table 4.2. This case differs from the preceding one as now the first resonance peak occurs sooner at $\rho_0 = 0.334$. This is expected because by increasing the value of μ, the perturbing mass has a greater ability to interact with the smaller mass to alter its orbit. There exists a stability region from $\rho_0 = 0.250$ to 0.333. However, the value of the maximum Lyapunov exponent peaks at seven different values of ρ_0, which demonstrates the greater influence of the perturbing mass m_2 compared to the case of $\mu = 0.1$. Also, there are apparent gaps surrounding the instability regions. Actually, they are due to our increment size in ρ_0 and, therefore, these regions should be treated as continuous with appropriate lines transitioning from one region to the next. There is also a resonance plateau in the range of $\rho_0 = 0.45$ to 0.48. This illustrates a region where the phenomena of resonance is widespread; note there is a similar feature in the study of asteroids (i.e., the 3:1 resonance at 2.5 AU or $\rho_0 = 0.48$).

The third case of $\mu = 0.3$ is depicted in Figure 4.3 and the associated numerical results are given in Table 4.3. Here the first resonance peak occurs at $\rho_0 = 0.355$. It also exhibits a well-pronounced region where the resonance is not substantial enough to alter the orbit of the small mass m_3 as shown in Figure 4.3 from $\rho_0 = 0.250$ to

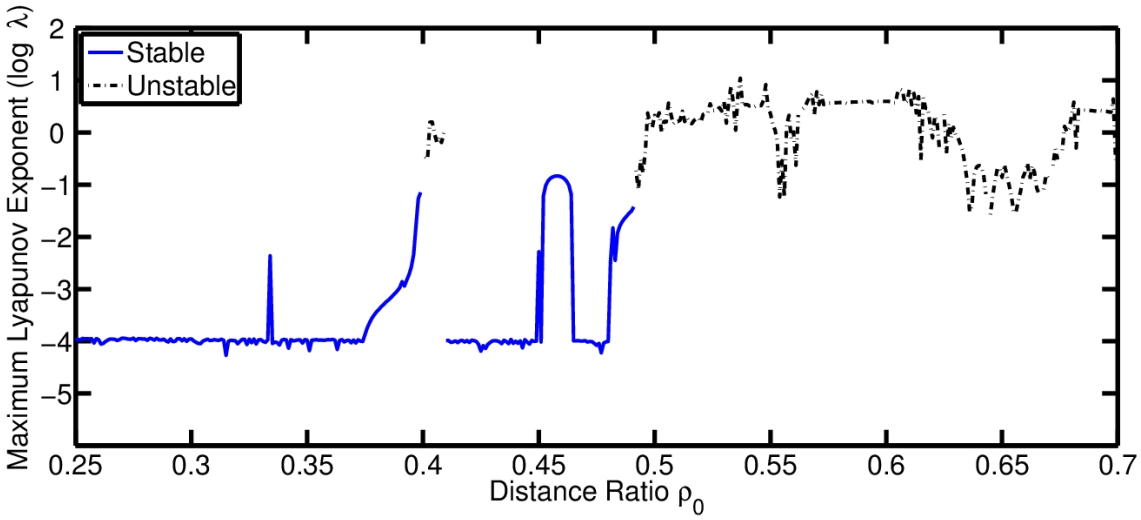

Figure 4.2. Same as Figure 4.1 but for $\mu = 0.2$..

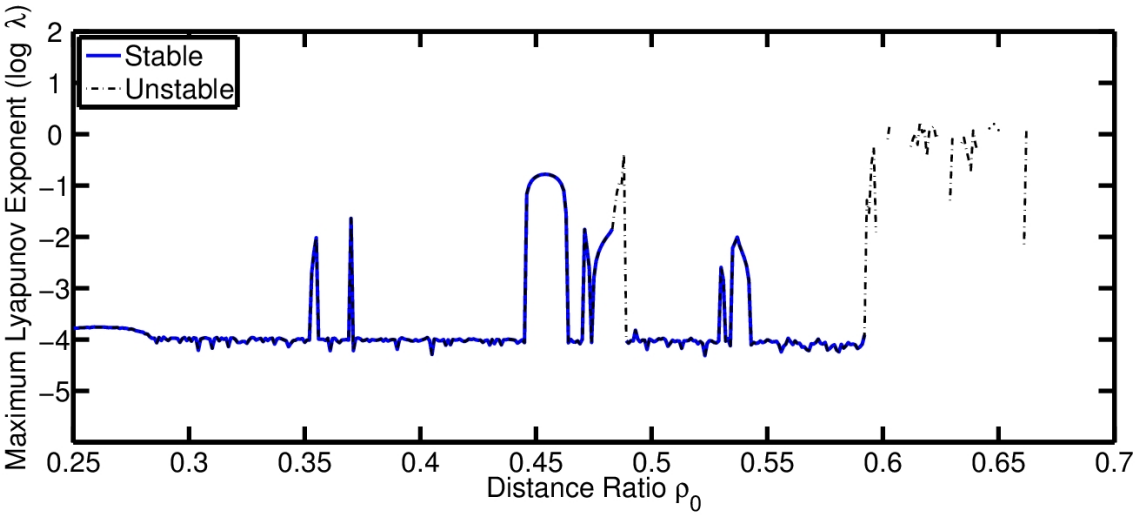

Figure 4.3. Same as Figure 4.1 but for $\mu = 0.3$..

0.354. The value of the maximum Lyapunov exponent peaks at 9 different values of ρ_0 before reaching the stability limit at $\rho_0 = 0.600$ as shown by Eberle et al. (2008). It is important to note that the number of resonance peaks has increased thus far as the value of μ has increased. Also this case includes a peak in the maximum Lyapunov exponent, where the system is unstable at $\rho_0 = 0.488$ leading to planetary ejection.

The transition to this instability is shown by the developing resonances at $\rho_0 = 0.483$ in Table 4.3.

The fourth case of $\mu = 0.4$ is depicted in Figure 4.4 with numerical results given in Table 4.4. This case differs from the preceding trend by the first resonance peak; this peak is delayed and occurs at $\rho_0 = 0.429$ after an instability island. This is due to the perturbing mass gaining an overwhelming amount of gravitational influence over the small mass and creating an instability region from $\rho_0 = 0.350$ to 0.400. Due to this change there are fewer positions for resonance to occur, the resonances become denser with respect to ρ_0, and the value of the maximum Lyapunov exponent peaks at 7 different values of ρ_0.

The final case of $\mu = 0.5$ is depicted in Figure 4.5 and the relevant numerical results are given in Table 4.5. This case differs as the first resonance peak is found to occur sooner at $\rho_0 = 0.410$. The Copenhagen case shows the worst case scenario for the small mass because the tug of war between the large masses becomes the most extreme. As a result there is only two narrow regions of stability. The value of the maximum Lyapunov exponent peaks at only two different values of ρ_0. The first resonance characterizes a stable resonance, whereas the second is a resonance that shows the transition from stability to instability via resonance overlap.

4.3.1.1 Classification of resonances

In Tables 1 to 5, I have identified the existence of 2 possible resonances. I will now discuss them separately starting with the results obtained for Resonance 1. These results show that the 2:1 resonance occurs in all considered cases of μ, except $\mu = 0.3$. It is also shown that the 2:1 resonance is the most common resonance in the coplanar CRTBP in agreement with previous asteroidal investigations. The 3:1 resonance is the second most common resonance as it occurs in all cases except

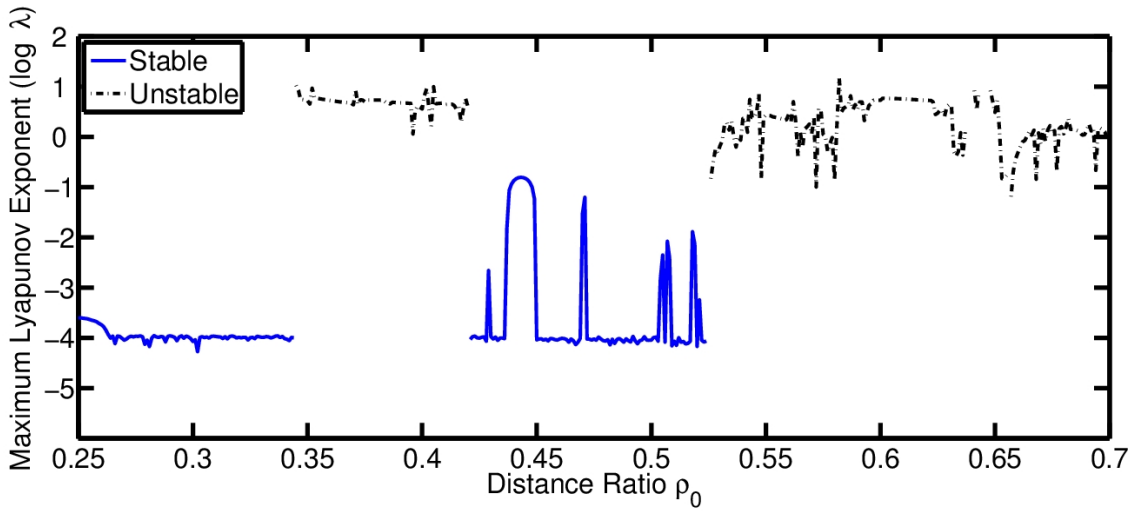

Figure 4.4. Same as Figure 4.1 but for $\mu = 0.4$..

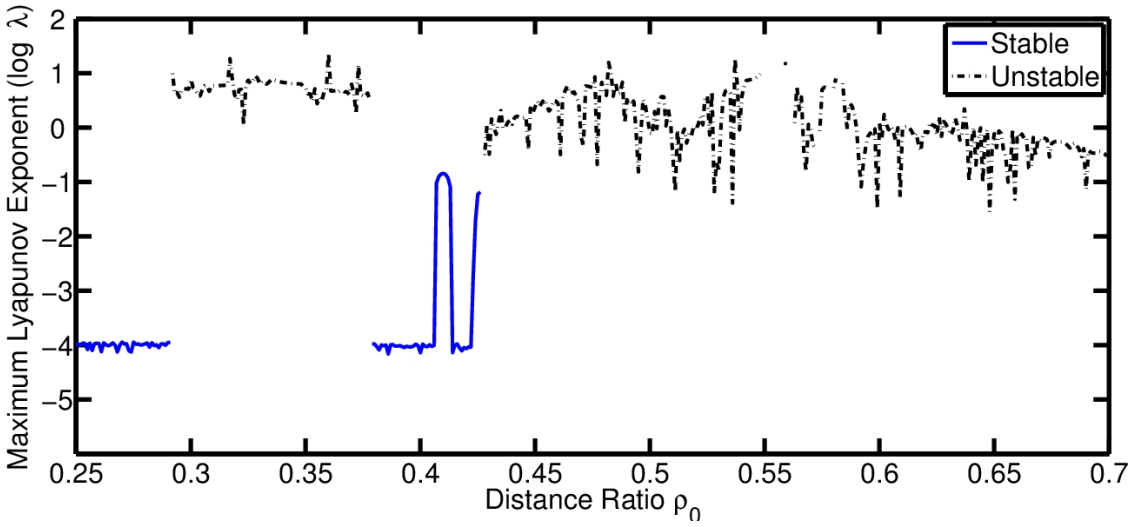

Figure 4.5. Same as Figure 4.1 but for $\mu = 0.5$..

$\mu = 0.5$. A new and interesting result is that both the 3:2 and 5:3 resonances occur more often than the 4:1 resonance, which only occurs for $\mu = 0.2$ and 0.3.

The overall picture obtained from the special cases of the values considered for μ is that the best chance for a resonance occurs at the intermediate value of $\mu = 0.3$. In this case, the systems start with a resonance reflecting a large ratio of the small mass period to the large mass period. Then as the parameter ρ_0 increases, so does

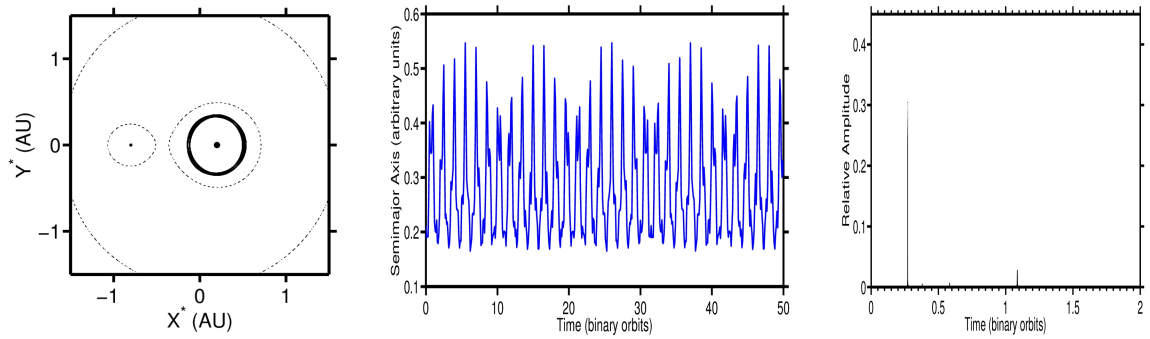

(a) (b) (c)

Figure 4.6. Case study showing the results for $\mu = 0.2$ and $\rho = 0.334$. Panel (a) shows the orbit of a planet in a rotating coordinates system, (b) shows the osculating semi-major axis for the first 50 binary orbits, and (c) shows the Fourier periodogram to determine the possible resonances..

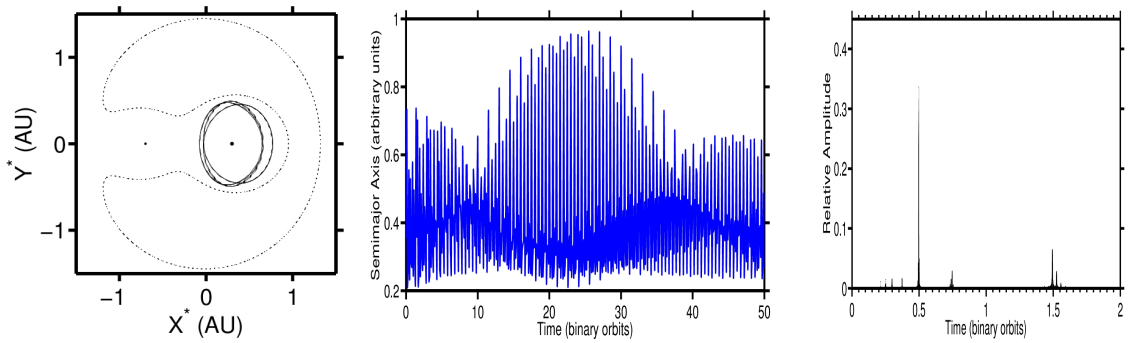

(a) (b) (c)

Figure 4.7. Case study showing the results for $\mu = 0.3$ and $\rho = 0.471$. Panel (a) shows the orbit of a planet in a rotating coordinates system, (b) shows the osculating semi-major axis for the first 50 binary orbits, and (c) shows the Fourier periodogram to determine the possible resonances..

the value of the ratio. After crossing the smoothest peak at $\rho_0 = 0.454$, the secondary resonances are formed; these resonances are labeled as Resonance 2 in Tables 1 to 5 and once they appear their existence may imply instability caused by resonance overlap. Among these resonances, the 3:1 resonance is the most dominant but new resonances such as 5:2 also occur, which is present for $\mu = 0.2$ and 0.3, and 5:1

occurring for $\mu = 0.4$. An interesting result is that only the 3:1 resonance occurs also as a secondary resonance and that none of the other resonances labeled as Resonance 1 also occur as Resonance 2.

Additionally, resonances can be classified based on the behavior of the orbits. In Tables 4.1 to 4.5, I show classifications based on orbit diagrams in rotating coordinates (see Figures 4.6 to 4.9a) and the osculating semi-major axis of the small mass (see Figures 4.6 to 4.9b). The three classes are periodic, quasi-periodic, and non-periodic, denoted by P, QP, and NP, respectively. Periodic orbits are those that are well-defined (i.e., minimal deviation from the path traced by previous orbits). They are closed, show periodic variations in the osculating semi-major axis, and show two dominant peaks in the corresponding periodogram (see Figures 4.6c, 4.7c, and 4.9c). Quasi-periodic orbits are those that precess or fill an annulus with an inner and outer boundary. Moreover, quasi-periodic orbits exhibit a more complicated osculating semi-major axis as well as a periodogram with several peaks (see Figures 4.7b,c). Non-periodic orbits are those that do not show a regular pattern and are thus most likely to be unstable. Also non-periodic cases show the greatest number of peaks in their periodograms. Of the cases presented, a low value of μ yields a greater probability for periodic orbits. As the mass ratio μ increases, the probability for quasi-periodic orbits increases due to increasing influence of the perturbative mass and duration of the perturbation. However, there are some periodic orbits that exist for large values of μ. They occur near the smooth plateau that forms in each of the figures.

4.4 Summary

The resonance case studies of the coplanar CRTBP presented in this dissertation were used to identify and classify resonances in the coplanar CRTBP. My method

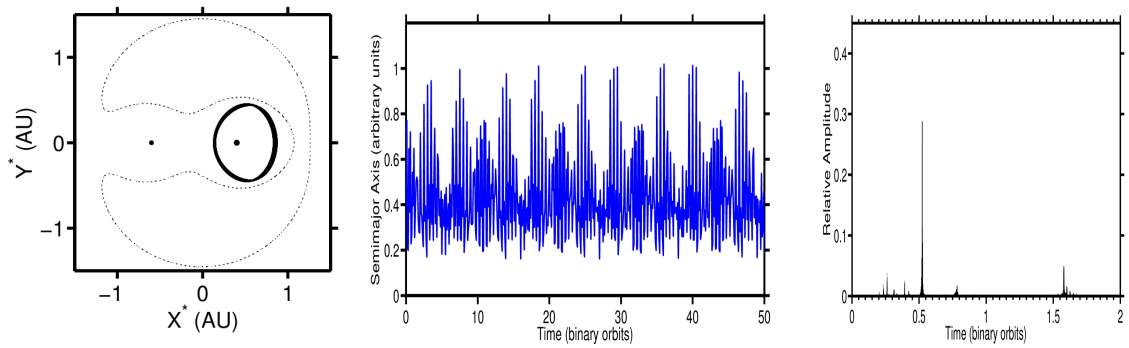

(a) (b) (c)

Figure 4.8. Case study showing the results for $\mu = 0.4$ and $\rho = 0.471$. Panel (a) shows the orbit of a planet in a rotating coordinates system, (b) shows the osculating semi-major axis for the first 50 binary orbits, and (c) shows the Fourier periodogram to determine the possible resonances..

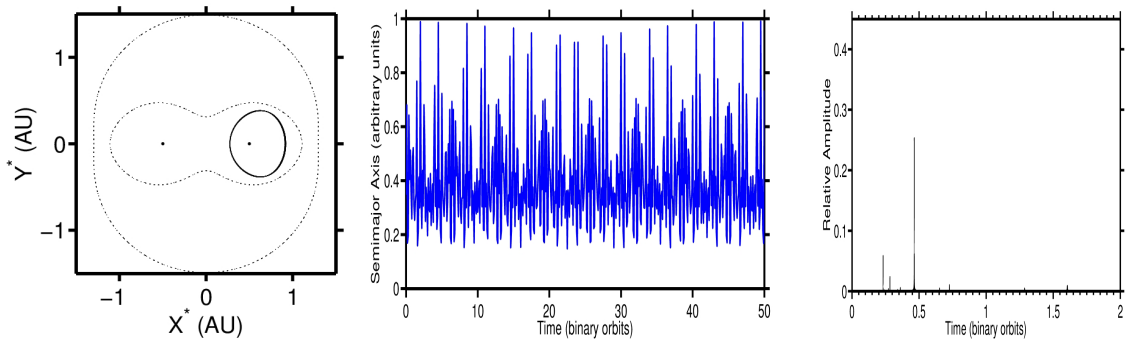

(a) (b) (c)

Figure 4.9. Case study showing the results for $\mu = 0.5$ and $\rho = 0.410$. Panel (a) shows the orbit of a planet in a rotating coordinates system, (b) shows the osculating semi-major axis for the first 50 binary orbits, and (c) shows the Fourier periodogram to determine the possible resonances..

of finding resonances is based on the concept of Lyapunov exponents, or more specifically, it uses the maximum Lyapunov exponent. Based on the latter, I was able to determine where the resonances occurred for a fixed value of mass ratio μ. The conditions for uncovering these resonances were determined by the value of the maximum Lyapunov exponent at the end of each simulation. The fact that the value of the

maximum Lyapunov exponent peaks at specific values of distance ratio ρ_0 provides a strong indicator for the positions of the resonances. Using this method, I have shown that stability is ensured for high values of resonance (i.e., high integer ratios) where only a single resonance is present.

Then I identified the primary and secondary resonances in the coplanar CRTBP as Resonance 1 and 2 (see Tables 1 to 5), have shown that the 2:1 resonance occurs most frequently as Resonance 1 in the considered systems, and have shown that the 3:1 resonance is the next most common (Quarles et al. 2012c). An interesting result is that there are two other resonances, which are 3:2 and 5:3, and that they occur more often than the 4:1 resonance. Among the resonances labeled as Resonance 2, the 3:1 resonance is the most dominant but there are also new resonances such as 5:2 and 5:1. Moreover, I found that the 3:1 resonance is the only one that also occurs as a secondary resonance, and that none of the other resonances identified by us as Resonance 1 also occur as Resonance 2 (Quarles et al. 2012c). The existence of the resonances labeled as Resonance 2 is important as it may imply the onset of instability caused by the resonance overlap.

I have also classified the resonances in the coplanar CRTBP based on the behavior of the orbits. The following three different classes were used: periodic (P), quasi-periodic (QP), and non-periodic (NP); see Eberle & Cuntz (2010b) and Quarles et al. (2011) for previous usages of these classes in conjunction with proposed criteria for the onset of orbital instability. Among the considered cases, a low value for μ and ρ_0 entailed a greater probability for periodic orbits to occur. Then, the probability for quasi-periodic orbits increases as μ increases. However, some periodic orbits were discovered that exist for large values of μ.

The resonances reported in this dissertation are consistent with the previously established resonances for the Solar System, specifically, in the asteroid belt with its

dominant 2:1 resonance (Ferraz-Mello 1994). They used digital filtering and Lyapunov characteristic exponents to determine stochasticity of the eccentricity. This is consistent with my usage of Lyapunov exponents as I took an alternate approach, which is varying the mass ratio instead of the eccentricity. This approach provides general results for the cases where μ is considerably greater than the value of μ in Sun–Jupiter-type systems but where the eccentricity is small. Although my results have been obtained for the special case of the coplanar CRTBP, I expect that it will be possible to augment the findings to planets in general stellar binary systems. Desired generalizations should include studies of the ERTBP (e.g., Pilat-Lohinger & Dvorak 2002; Szenkovits & Makó 2008) as well as applications to planets in previously discovered star–planet systems.

CHAPTER 5

THE STABILITY OF THE SUGGESTED PLANET IN THE ν OCTANTIS SYSTEM

In order to apply my previously determined stability criteria (see Chapters 3 & 4), I provide a detailed theoretical study aimed at the observational finding about the ν Octantis binary system that indicates the possible existence of a Jupiter-type planet in this system. If a prograde planetary orbit is assumed, it has earlier been argued that the planet, if existing, should be located outside the zone of orbital stability. However, a previous study by Eberle & Cuntz (2010a) concludes that the planet is most likely stable if assumed to be in a retrograde orbit with respect to the secondary system component. In the present work, I significantly augment this study by taking into account the observationally deduced uncertainty ranges of the orbital parameters for the stellar components and the suggested planet. Furthermore, this study employs additional mathematical methods, which include monitoring the Jacobi constant, the zero velocity function, and the maximum Lyapunov exponent. I again find that the suggested planet is indeed possible if assumed to be in a retrograde orbit, but it is virtually impossible if assumed in a prograde orbit. Its existence is found to be consistent with the deduced system parameters of the binary components and of the suggested planet, including the associated uncertainty bars given by observations.

5.1 Background

The binary system ν Octantis, consisting of a K1 III star (Houk & Cowley 1975) and a faint secondary component, identified as spectral type K7–M1 V (Ramm

et al. 2009) is located in the southernmost portion of the southern hemisphere, i.e., in close proximity to the Southern Celestial Pole. In 2009, Ramm et al. found new detailed astrometric–spectroscopic orbital solutions, implying the possible existence of a planet[1] around the main stellar component. Thus, ν Octantis A is one of the very few cases where a planet is found to orbit a giant rather than a late-type main-sequence star; the first case of this kind is the planetary-mass companion to the G9 III star HD 104985 (Sato et al. 2003).

The composition of the ν Octantis system leads to many open questions particularly about the orbital stability of the proposed planet. The semimajor axis of the binary system has been deduced as 2.55 ± 0.13 AU with an eccentricity given as 0.2358 ± 0.0003 (Ramm et al. 2009). Furthermore, the semimajor axis of the planet, with an estimated minimum mass $M_p \sin i$ of approximately 2.5 M_J, was derived as 1.2 ± 0.1 AU (see Table 5.1). The distance parameters indicate that the proposed planet is expected be located about halfway between the two stellar components. This is a set-up in stark contrast to other observed binary systems hosting one or more planets (Eggenberger et al. 2004; Raghavan et al. 2006) and, moreover, difficult to reconcile with standard orbital stability scenarios.

A possible solution was proposed by Eberle & Cuntz (2010a). They argued that the planet might most likely be stable if assumed to be in a retrograde orbit relative to the motion of the secondary stellar component. Previous cases of planetary retrograde motion have been discovered, but with respect to the spin direction of the host stars. Examples include (most likely) HAT-P-7b (or Kepler-2b), WASP-8b and WASP-17b that were identified by Winn et al. (2009), Queloz et al. (2010), and Anderson et al. (2010), respectively. These discoveries provide significant challenges to the standard

[1] An alternative explanation involves a hierarchical triple system, invoking a precessional motion of the main stellar component, as proposed by Morais & Correia (2012).

paradigm of planet formation in protoplanetary disks as discussed by Lissauer (1993) and Lin et al. (1996).

The previous theoretical work by Eberle & Cuntz (2010a) explored two cases of orbital stability behavior for ν Octantis based on a fixed mass ratio for the stellar components and a starting distance ratio of $\rho_0 = 0.379$ for the putative planet (see definition below). They found that if the planet is placed in a prograde orbit about the stellar primary, it almost immediately faced orbital instability, as expected. However, if placed in a retrograde orbit, stability is encountered for at least 1×10^7 yr or 3.4×10^6 binary orbits, i.e., the total time of simulation. This outcome is also consistent with the results from an earlier study by Jefferys (1974) based on a Henon stability analysis, which indicates significantly enlarged regions of stability for planets in retrograde orbits.

Nonetheless, there is a significant need for augmenting the earlier study by Eberle & Cuntz (2010a). Notable reasons include: first, Eberle & Cuntz only considered three possible mass ratios and one possible set of values for the semimajor axis and eccentricity for the stellar components, thus disregarding their inherent observational uncertainties. Hence, it is unclear if or how the prograde and retrograde stability regions for the planetary motions will be affected if other acceptable choices of system parameters are made. Second, Eberle & Cuntz chose the 9 o'clock position as the starting position for the planetary component. Thus, it is unclear if or how the timescale of orbital stability will change due to other positional choices in the view of previous studies, which have demonstrated a significant sensitivity in the outcome of stability simulations on the adopted planetary starting angle (e.g., Fatuzzo et al. 2006; Yeager et al. 2011). Third, and foremost, Eberle & Cuntz did not utilize detailed stability criteria for the identification of the onset of orbital instability. Possible mathematical methods for treating the latter include monitoring the Jacobi constant

and the zero velocity function (e.g., Szebehely 1967; Eberle et al. 2008) as well as using the maximum Lyapunov exponent (e.g., Hilborn 1994; Smith & Szebehely 1993; Lissauer 1999; Murray & Holman 2001). In the previous work reported by Cuntz et al. (2007), Eberle et al. (2008) and Quarles et al. (2011), these methods have been extensively used for investigating the orbital stability in the circular restricted 3-body problem. The same methods will be adopted in the present study.

Table 5.1. Stellar and Planetary Parameters of ν Octantis

Parameter	Value	Reference
Spectral type (1)	K1 III	Houk & Cowley (1975)
Spectral type (2)	K7−M1 V	Ramm et al. (2009)
R.A.	21 41 28.6463	ESA (1997)[a,b]
Decl.	−77 23 24.167	ESA (1997)[a,b]
Distance (pc)	21.20 ± 0.87	van Leeuwen (2007)
M_v (1)	2.10 ± 0.13	Ramm et al. (2009)[c]
M_v (2)	$\sim$ 9.9	Drilling & Landolt (2000)
M_1 ($M_\odot$)	1.4 ± 0.3	Ramm et al. (2009)
M_2 ($M_\odot$)	0.5 ± 0.1	Ramm et al. (2009)
$T_{\rm eff,1}$ (K)	4790 ± 105	Allende Prieto & Lambert (1999)
R_1 ($R_\odot$)	5.9 ± 0.4	Allende Prieto & Lambert (1999)
P_b (d)	1050.11 ± 0.13	Ramm et al. (2009)
a_b (AU)	2.55 ± 0.13	Ramm et al. (2009)
e_b	0.2358 ± 0.0003	Ramm et al. (2009)
$M_p \sin i$ (M_J)	2.5 ± ...	Ramm et al. (2009)[d]
a_p (AU)	1.2 ± 0.1	Ramm et al. (2009)[d]
e_p	0.123 ± 0.037	Ramm et al. (2009)[d]

[a] Data from SIMBAD, see `http://simabd.u-strasbg.fr`.
[b] Adopted from the *Hipparcos* catalog.
[c] Derived from the stellar parallax, see Ramm et al. (2009).
[d] Controversial.

5.2 Theoretical Approach

5.2.1 Basic Equations

Using the orbital parameters attained by Ramm et al. (2009), see Table 5.1, I consider the coplanar restricted 3-body problem (RTBP) applied to the system of ν Octantis. Following the standard conventions pertaining to the coplanar RTP, I write the equations of motion in terms of the parameters μ and ρ_0. The parameter μ and the complementary parameter α are defined by the two stellar masses M_1 and M_2 (see Section 2.1.2). The planetary distance ratio ρ_0 (see Section 4.2) depends on R_0 and D, which denote the initial distance of the planet from its host star, the more massive of the two stars with mass M_1, and the initial distance between the two stars, respectively. In addition, I represent the system in a rotating reference frame, which introduces Coriolis and centrifugal forces. The following equations of motion utilize these parameters (Szebehely 1967):

$$\dot{x} = u \tag{5.1}$$

$$\dot{y} = v \tag{5.2}$$

$$\dot{z} = w \tag{5.3}$$

$$\dot{u} = 2v + \Omega(x - \alpha\frac{x-\mu}{r_1^3} - \mu\frac{x+\alpha}{r_2^3}) \tag{5.4}$$

$$\dot{v} = -2u + \Omega(y - \alpha\frac{y}{r_1^3} - \mu\frac{y}{r_2^3}) \tag{5.5}$$

$$\dot{w} = -z + \Omega(z - \alpha\frac{z}{r_1^3} - \mu\frac{z}{r_2^3}) \tag{5.6}$$

where

$$\Omega = (1 + e\cos f)^{-1} \tag{5.7}$$

$$r_1 = \sqrt{(x-\mu)^2 + y^2 + z^2} \tag{5.8}$$

$$r_2 = \sqrt{(x+\alpha)^2 + y^2 + z^2} \tag{5.9}$$

The variables in the above equations describe how the state of a planet, commensurate to a test object, evolves due to the forces present. The state is represented in a normalized Cartesian coordinate system (see Section 3.2 for the appropriate transformation) $\{x,\ y,\ z,\ u,\ v,\ w\}$. I use dot notation to represent the time derivatives of the coordinates $\left\{\dot{x} = \frac{\mathrm{dx}}{\mathrm{dt}}\right\}$. Since the variables $\{u,\ v,\ w\}$ represent the velocities, the time derivatives of these variables represent the accelerations. The variables $\{r_1,\ r_2\}$ denote the distances of the planet from each star in the rotating reference frame. The value of f describes the true anomaly of the mass M_1 and e refers to the eccentricity of the stellar orbits.

5.2.2 Initial Conditions

The coplanar RTBP indicates that the putative planet moves in the same orbital plane as the two stellar components; additionally, its mass is considered negligible[2]. The initial orbital velocity of the planet is calculated assuming a Keplerian circular orbit about its host star. For simplicity we assume the (u, w) components are equal to zero and the magnitude of the velocity to be in the direction of the v component. The mean value of the eccentricity of the binary, e_b, is used due to accuracy of the value given. A Taylor expansion in initial orbital velocity of the binary shows that the

[2]Negligible mass means that although the body's motion is influenced by the gravity of the two massive primaries, its mass is too low to affect the motions of the primaries.

first order correction would only change the initial orbital velocity of the respective stars by a factor of 10^{-8}. The initial eccentricity of the planet, e_p, has been chosen to be equal to zero due to the redundancy it provides in the selection of the initial planetary position. Noting that the inclination angle of the planet, i_p, has not yet been determined, it is taken to be 90° consistent with the requirement of the coplanar RTBP.

To integrate the equations of motion, a sixth order symplectic integration method is used (Yoshida 1990). In the computation of Figures 5.2 and 5.3 a fixed time step of 10^{-3} is assumed. This proved to be appropriate since the average relative error in the Jacobi constant is found to be on the order of 10^{-8}. To increase the precision for the individual cases depicted in Figures 5.5 to 5.9, a fixed time step of 10^{-4} is used, which decreased the average relative error to the order of 10^{-10}. However, this choice entailed a considerable increase of the computation time. Therefore, Figure 5.2 was integrated for 10,000 binary orbits (approximately 29,000 years) and Figure 5.3 was integrated for 1,000 binary orbits (approximately 2,900 years), which this figure is considerably less than utilized in the mainframe of our study in determining the statistical possibility of a prograde planetary configuration. Also, Figures 5.5 to 5.9 were integrated for 80,000 binary orbits (approximately 232,000 years).

In the treatment of this problem, four separate types of initial conditions of the system are considered. They encompass the two different starting positions of the planet with respect to the massive host star, which are: the 3 o'clock and 9 o'clock positions (see Figure 5.1). With each of these starting positions, I considered the possibility of planetary motion in counter-clockwise and clockwise directions relative to the direction of motion of the secondary stellar component; the directions are referred to as prograde and retrograde, respectively. The primary masses are considered to move in ellipses about the center of mass of the system.

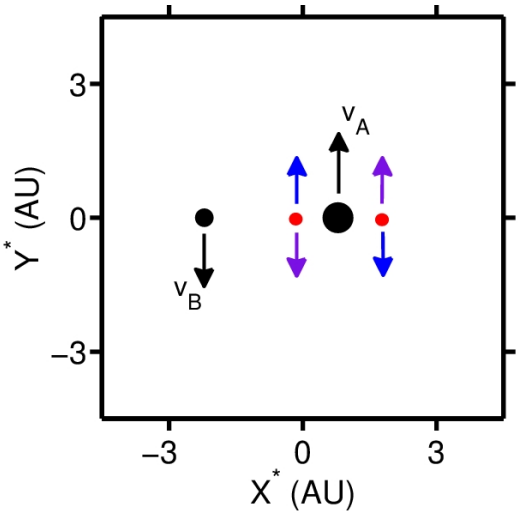

Figure 5.1. Example of the possible initial starting configurations. The directions of the initial velocities of the stellar components (ν Oct A and ν Oct B) are shown with black colored arrows and appropriate labels. The proposed planet is represented by the red colored dots in the 3 o' clock position (right) and the 9 o' clock position (left). The possible directions of the initial velocity for the planetary component are either prograde (purple) or retrograde (blue). These arrows are shown to demonstrate the direction in the initial configurations and are not representative of any other physical attributes of the system .

5.2.3 Statistical Parameter Space

In the this section, I will explore the role(s) of small variations in the system parameters. Notably I will investigate how the stellar mass ratio as well as the semimajor axis and inherently the eccentricity of the stellar components can change the outcome of the orbital stability simulations. Particularly when I consider the statistical probability of prograde orbits for the suggested planet. These variations are due to the observational uncertainties of the respective parameter; see Ramm et al. (2009) and Table 5.1 for details.

Using the definition of the mass ratio μ with $M_1 = 1.4 \pm 0.3\ M_\odot$ and $M_2 = 0.5 \pm 0.1\ M_\odot$. Taking M_1 and M_2 as statistically independent from one another, the bounding values for μ are $[0.220, 0.306]$, i.e., 0.263 ± 0.043. In this case, I assumed

the reported uncertainty bars for the stellar masses to be 1.25 σ, noting that through this choice μ is consistent with the mass ratio $q = 0.38 \pm 0.03$ derived by Ramm et al. (2009) that was used for computing M_2 based on the sum of the two masses. Formulas and methods for the propagation-of-error, which in essence employ a first-order Taylor expansion, have been given by, e.g., Meyer (1975); see also Press et al. (1986) for numerical methods if the error is calculated via a Monte-Carlo simulation.

The parameter ρ_0 gives the definition for the relative initial distance of the planet, expressed in terms of R_0 and D, i.e., the initial distance of the planet from its host star, the more massive of the two stars with mass M_1 and the initial distance between the two stars, respectively. This definition also allows to compute the bounding values for ρ_0. Following the assumption made by Eberle & Cuntz (2010a), the set-up of the binary system will be initialized by assuming the secondary stellar component to be located in the apastron starting position, entailing that D is modified as $D = a_b\,(1 + e_b)$. Thus, the observation uncertainties of a_p, a_b, and e_b will be utilized to compute the bounding values for ρ_0 (see Table 5.1). As result I obtain $[0.344, 0.418]$, i.e., 0.381 ± 0.037. These values will be considered in the subsequent set of detailed orbital stability studies by making appropriate choices for μ and ρ_0 when setting the initial conditions. The outcome of the various simulations will, in particular, allow a detailed statistical analysis of the mathematical probability for the existence of the suggested planet in a prograde orbit; see Section 5.3.3.

5.2.4 Stability Criteria

In my approach I employ two independent criteria. One method deals with identifying events that can cause instability, whereas the other method allows for the determination of stability. First, I monitor the relative error in the Jacobi constant to detect instabilities. By monitoring this constant I can determine when the inte-

grator loses its accuracy or fails completely. It has been shown that this method is particularly sensitive to close approach events of the planet with any of the stellar components. However, it has also previously been demonstrated by Eberle et al. (2008) and Eberle & Cuntz (2010b) that these close approach events are preceded by an encounter with the so-called "zero velocity contour" (ZVC) for the coplanar circular RTBP.

Generalizing this criteria to the elliptic RTP, an analogous "zero velocity function" (ZVF) can be found that is, however, dependent on the initial distance between the stellar components (Szebehely 1967). The ZVF can also be described by a pulsating ZVC; see Szenkovits & Makó (2008) for updated results. Note that the ZVC will be largest when the binary components are at apastron and smallest when they are at periastron. Noting that I have chosen the stars to be at the apastron starting position, the largest ZVC is inherently defined as well. When the planetary body encounters the ZVC, the orbital velocity decreases dramatically, which reduces the $\dot{u}$ and $\dot{v}$-related forces. As a result, the planetary body follows a trajectory that results in a close approach. This behavior provides an indication that the system will eventually become unstable, resulting in an ejection of the planetary body from the system or its collision with one of the stellar components. Specifically this simulation model assumes that all the bodies exist as point masses so that all unstable events will behave as ejections from the system. This was chosen because the details in discerning between ejections or collisions does not enhance the prospects of the stability for the proposed body.

The second criterion utilizes the method of Lyapunov exponents (Lyapunov 1907), which is commonly used in nonlinear dynamics for determining the onset of chaos in different dynamical systems (e.g., Hilborn 1994; Musielak & Musielak 2009). A numerical algorithm that is typically adopted for calculating the spectrum of Lya-

punov exponents was originally developed by Wolf et al. (1985) (see Appendix B for details).

The Lyapunov exponents have extensively been used in studies of orbital stability in different settings pertaining to the Solar System (e.g., Lecar et al. 1992; Milani & Nobili 1992; Lissauer 1999; Murray & Holman 2001). Typically, the maximum Lyapunov exponent (MLE) is adopted as a measure of the rate with which nearby trajectories diverge. The reason is that the MLE offers the unique measure of the largest divergence. I previously used the MLE criterion to provide a cutoff for which stability can be assured given the behavior of the MLE in time. This cutoff value has previously been determined by Quarles et al. (2011); it is given as $\log \lambda_{\max} = -0.82$ on a logarithmic scale of base 10. Recalling that the cutoff in MLE is related inversely to the Lyapunov time, t_L, which gives an estimate of the predictive period for which stability is guaranteed. Then the more negative the logarithmic value of the MLE, the longer the orbital stability will be ensured. Due to the finite time of integration, this estimate is only valid for the integration timescale considered. But the nature of how the MLE changes in time will provide the evidence to whether the MLE is asymptotically decreasing and thereby orbitally stable. Hence this cutoff will be used in the present paper for establishing orbital stability of the suggested planet in the ν Octantis system.

5.3 Results and Discussion

5.3.1 Model Simulations

In the following I report the general behavior of stability for the set of orbital stability simulations pursued in this study. The initial focus is on the MLE. In Figures 5.2 and 5.3, the various values of the MLE as a function of μ and ρ_0 are denoted

Table 5.2. Survival Counts of the Suggested Planet in ν Octantis for 1,000 binary orbits

Configuration		Unstable Count	Stable Count	Stable Percentage
Prograde	3 o'clock	17544	1776	9.2 %
Prograde	9 o'clock	19200	120	0.6 %
Retrograde	3 o'clock	1040	19184	94.9 %
Retrograde	9 o'clock	0	20224	100 %

using a color code. The range of colors shows that dark red represents a relatively high (less negative) logarithmic MLE value, whereas dark blue represents a relatively low (more negative) logarithmic MLE value. The white background represents conditions, which failed to complete the respective allotted run time; see Sect. 5.2.4 for a discussion of possible conditions for terminating a simulation.

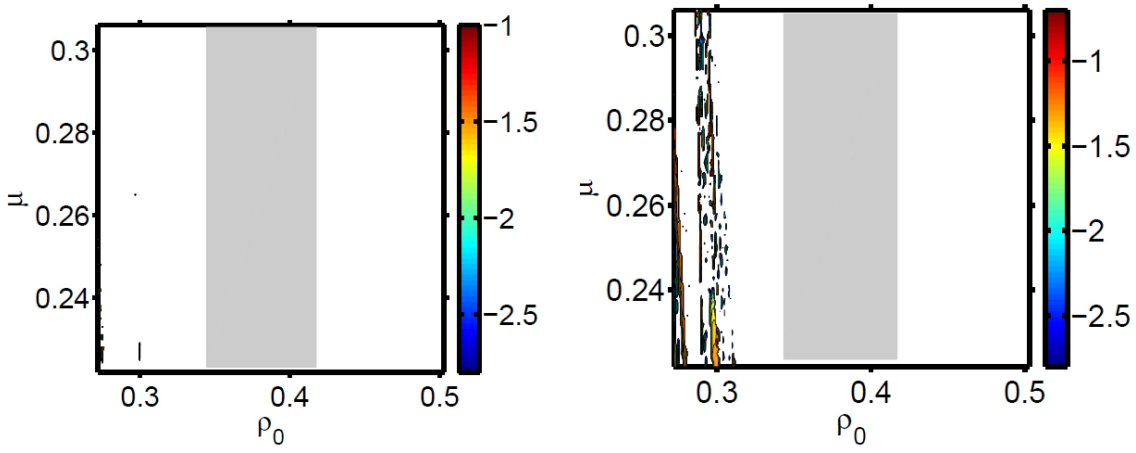

Figure 5.2. Detailed results of simulations in the parameter space for the case of prograde planetary motion. The left and right panel represent the simulations with the planet initially placed at the 9 o'clock and 3 o'clock position, respectively. The grey area represents the statistical 1σ range in ρ_0, which is 0.381 ± 0.037 .

Figure 5.2 shows the result of our simulations for 10,000 binary orbits, i.e., about 29,000 years, in the prograde configuration for starting conditions given by the 3 o'clock or 9 o'clock planetary position. The results were obtained using values of μ between 0.220 and 0.306 in increments of 0.001. Concerning the initial conditions in ρ_0, denoting the relative starting position of the planet, I use values between 0.272 and 0.502 in increments of 0.001. I show the 1σ region in ρ_0 between 0.344 and 0.418 where ν Oct is proposed to exist by a gray shaded region; see Section 5.2.3. Between the two bounding values regarding ρ_0, there does exist a region of stability as well as a marginal stability limit. The limit of marginal stability is consistent with previous findings by Holman & Wiegert (1999) for the case with the planetary eccentricity taken into account. This region of marginal stability is more pronounced in the 3 o'clock starting configuration; it begins at $\rho_0 \approx 0.315$. The marginal stability region decreases as μ increases, which is expected because the perturbing mass is becoming more significant as the mass ratio μ increases. There is a noticeable favoritism towards the 3 o'clock starting position as indicated by the survival counts given in Table 5.2. This outcome is expected as the perturbing mass exerts a lesser force on the planet if initially placed at the 3 o'clock position.

Figure 5.3 shows the result for the retrograde configuration for 1,000 binary orbits considering both the 3 o'clock and 9 o'clock planetary starting positions. Due to the larger number of conditions that survived during this time interval I have reduced the bounds of initial conditions following the bounding values of Eberle & Cuntz (2010a). Here the bounding values for μ are given as 0.2593 and 0.2908 with increments of 0.0001. The increment in μ was reduced to allow better insight into the role of chaos in this type of configuration. The initial conditions of ρ_0 begin with 0.353 and end with 0.416 in increments of 0.001, which allows to cover the most pronounced features of the retrograde configuration.

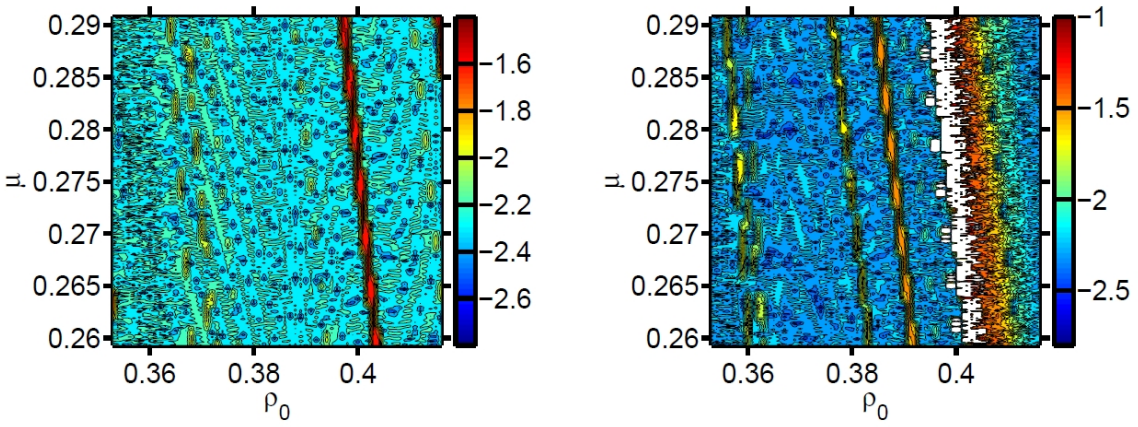

Figure 5.3. Same as Figure 5.2, but now for retrograde planetary motion. (Quarles et al. 2012a).

Figure 5.3 demonstrates a broad region of stability within the selected parameter space. The 9 o'clock starting position has many regions of bounded chaos. These regions of bounded chaos exhibit locally less negative values for MLE, which however do not exceed the previously determined cutoff value of $\log \lambda_{\max} = -0.82$; see Sect. 5.2.4. The nature of these orbits and the connection to the MLE will be discussed in Sect. 5.3.2. The greatest region of bounded chaos is obtained for $\rho_0 \approx 0.41$. This region decreases in ρ_0 as μ increases for the same reason as the change in the marginal stability limit in Figure 5.2. The 3 o'clock starting position shows similar features but there does exist a region of instability with this starting position at $\rho_0 \approx 0.41$. This region coincides with the extended region of bounded chaos in the 9 o'clock starting position. The nature of this region can be deduced from the parameters given by Ramm et al. (2009); see Table 5.1. There exists a 5:2 resonance of the planet with the binary that places the suggested planet moving towards the barycenter at the periastron point of the binary inducing an instability. For the 9

o'clock position the suggested planet would be moving away which would provide a large perturbation but insufficient for producing an instability.

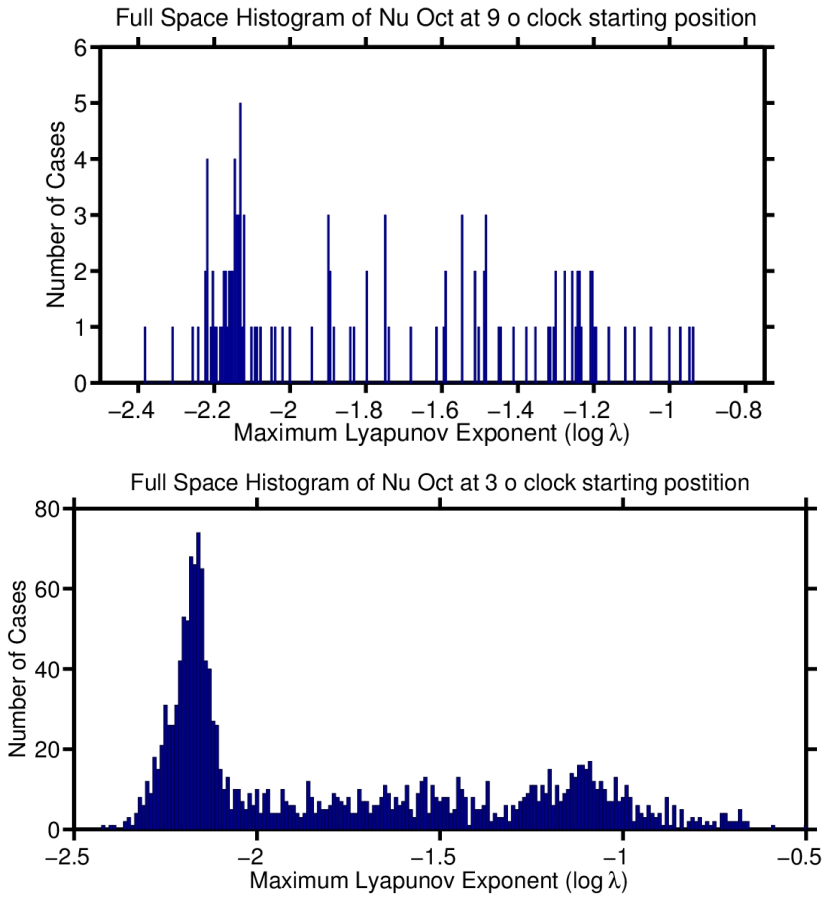

Figure 5.4. Histograms of configurations that survived 1000 binary orbits in prograde motion. Note the significant difference in scale regarding both the x and y-axis.

Figure 5.4 provides the histograms of simulations pertaining to both starting positions for the prograde configuration. These histograms indicate the number of surviving cases related to the array of initial conditions for the parameter space detailed in Figure 5.2. The bin width is 0.01 in the logarithmic MLE scale, corresponding to 1.47×10^{-4} in the linear MLE scale. Although there is not a case that survives 10,000 binary orbits in the 1 σ region, I provide these histograms to demonstrate

what different initial conditions entail near the lower and upper uncertainty limits. Figure 5.2 shows that all the surviving cases cluster towards the lower bound in ρ_0. Furthermore, it is obtained that the 9 o'clock starting position has far fewer surviving initial conditions than the 3 o'clock starting position. This is also reflected in the histograms. The histogram of the 9 o'clock position is sparse; without the aid of the 3 o'clock histogram there would be too few counts to provide substantial information. But inspecting the 3 o'clock histogram reveals that there is a Gaussian-type distribution about the logarithmic MLE value of -2.2. This indicates that for the limited simulation time adopted for this part of our study, there is a very small number of cases indicating stability for the prograde configuration. However, these cases are near the 2σ or 3σ limit concerning the permitted values of the planetary position ρ_0 as discussed in Sect. 5.3.3.

5.3.2 Case Studies

In the following I further probe some orbits of retrograde configurations in more detail; see Figures 5.5 to 5.9 for information. These figures show from left to right the respective orbital diagram in a rotating reference frame, the associated Lyapunov spectrum, and the Fourier periodogram. Through these diagrams I can assess the nature of these orbits to determine stability and measure the chaos within the system.

Figure 5.5 with $(\mu, \rho_0) = (0.2825, 0.400)$ is provided to show a case of instability. In this case I find that the orbit presents itself as a wide annulus and already at first glance appears chaotic. The Lyapunov spectrum reveals that the MLE levels off at $\log \lambda = -1$ fairly quickly, which is near the proposed cutoff value for unstable chaotic behavior. For the timespan between 300 and 800 binary orbits, the MLE fluctuates until it finally pushes upward to $\lambda_{\max}$. The Fourier periodogram shows that this case

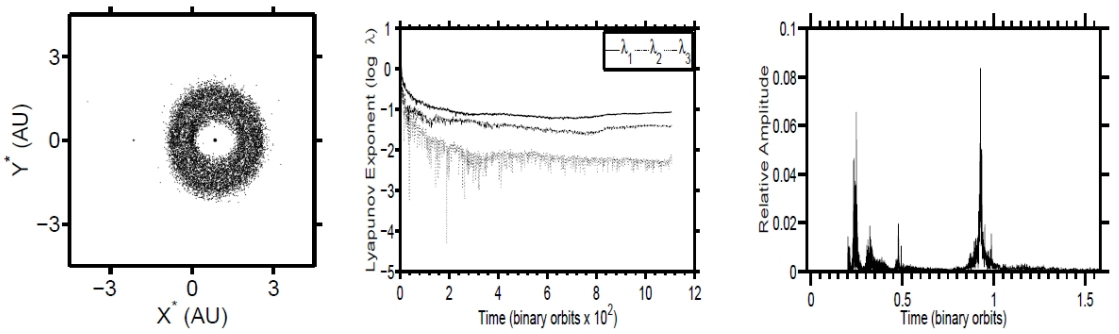

Figure 5.5. Case study of planetary motion with the planet placed in the 3 o'clock position and in retrograde motion. This case displays the conditions for $\mu = 0.2825$ and $\rho_0 = 0.400$.

is truly chaotic due to the amount of noise presented by the periodogram. There are many periods which may promote the outcome of instability via resonance overlap (e.g., Mudryk & Wu 2006; Mardling 2008). The proposed planet is approaching the barycenter when the binary is at its periastron position, which should be considered the main cause of this instability.

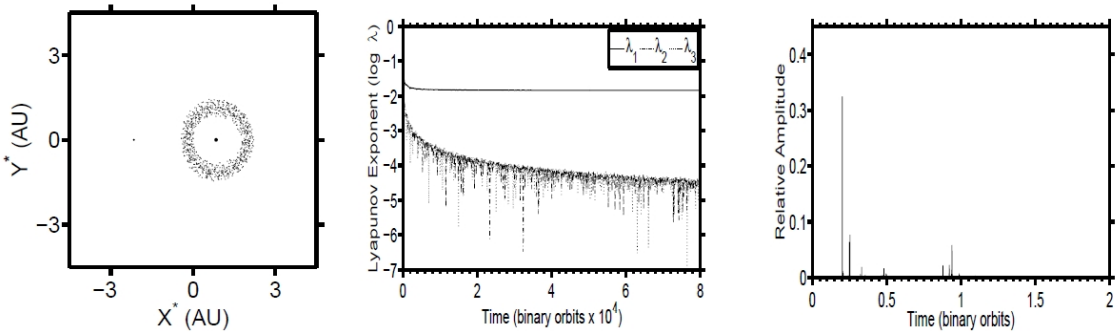

Figure 5.6. Case study of planetary motion with the planet placed in the 3 o'clock position and in retrograde motion. This case displays the conditions for $\mu = 0.2805$ and $\rho_0 = 0.358$.

Figures 5.6 and 5.7 with $(\mu, \rho_0) = (0.2805, 0.358)$ and $(0.2630, 0.374)$, respectively, exhibit similar features between each other in the orbit diagram and peri-

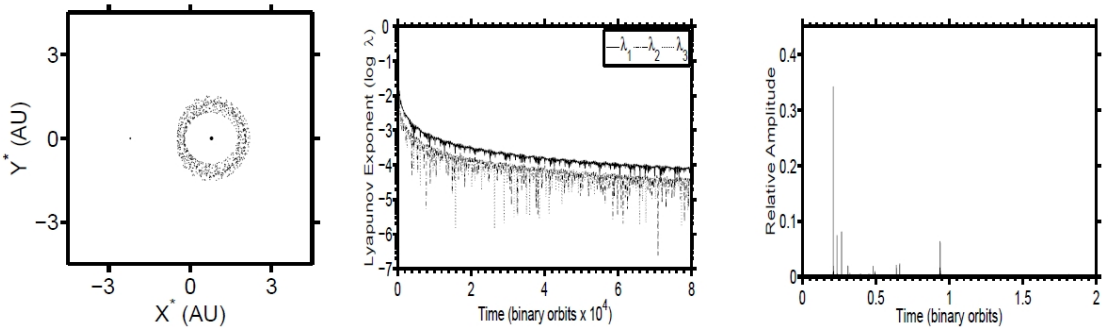

Figure 5.7. Case study of planetary motion with the planet placed in the 3 o'clock position and in retrograde motion. This case displays the conditions for $\mu = 0.2630$ and $\rho_0 = 0.374$.

odogram. However, there is a difference in the respective Lyapunov spectra. Both cases show trends of stability, although Figure 5.6 demonstrates bounded chaos. It presents a different nature than the previous case of instability (see Figure 5.5) as the MLE settles near $\log \lambda = -1.8$ and does not fluctuate enough to reach $\lambda_{\max}$. Both cases given as Figures 5.6 and 5.7 represent orbits that form annuli; however, the annulus widths are less than that of the unstable case depicted in Figure 5.5. They are thus classified as stable with Figure 5.6 being chaotic and Figure 5.7 being non-chaotic.

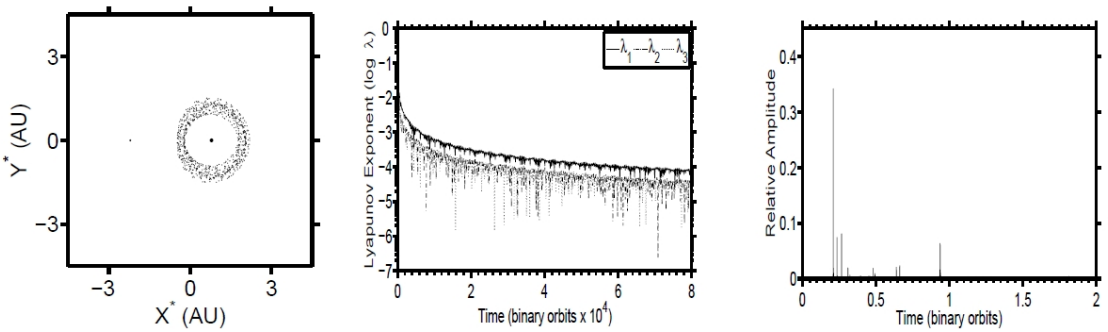

Figure 5.8. Case study of planetary motion with the planet placed in the 9 o'clock position and in retrograde motion. This case displays the conditions for $\mu = 0.2696$ and $\rho_0 = 0.401$.

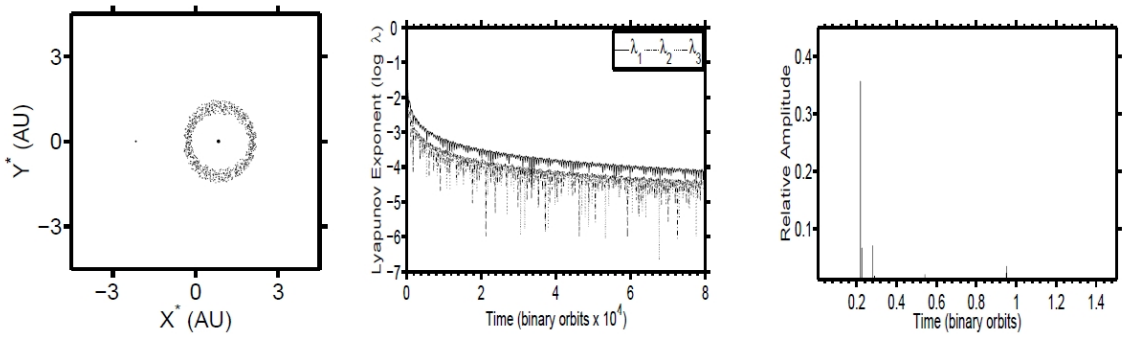

Figure 5.9. Case study of planetary motion with the planet placed in the 9 o'clock position and in retrograde motion. This case displays the conditions for $\mu = 0.2780$ and $\rho_0 = 0.388$.

Figures 5.8 and 5.9 with $(\mu, \rho_0) = (0.2696, 0.401)$ and $(0.2780, 0.388)$, respectively, reveal similar features compared to the previous set of figures regarding all three diagrams. These cases are provided to demonstrate the similarities between the 3 o'clock starting positions depicted in Figures 5.6 and 5.7 and the 9 o'clock starting positions depicted in Figures 5.8 and 5.9. The comparison between Figures 5.6 and 5.8 indicates a similar orbit diagram and periodogram, but the limiting values of the MLE settle at a slightly more negative value in Figure 5.6. Figures 5.7 and 5.9 supply similar orbital diagrams but there are minor differences in the periodograms and Lypaunov spectra. These figures display the same behavior in MLE but there is a difference in the periodic nature of the decrease in MLE, which is also revealed by the difference in the number of peaks in the corresponding periodograms.

5.3.3 Statistical Analysis of Orbital Stability

A significant component of this investigation is to provide a statistical analysis regarding whether or not the suggested planet in the ν Octantis system is able to exist in a prograde or retrograde orbit. Previously, I reported on the general behavior

Table 5.3. Statistical Probability of Prograde Planetary Orbits[a]

Mass Ratio	9 o'clock Position		3 o'clock Position	
μ	σ	Probability (%)	σ	Probability (%)
0.306	...	...	2.30	1.1
0.263	...	...	2.11	1.7
0.220	2.95	0.16	1.89	2.9

[a] Based on 10,000 binary orbits; see Figure 5.2

of orbital stability for the set of simulations with focus on the MLE (see Sect. 5.2.4). In Figures 5.2 and 5.3, the various values of the MLE were given as function of the mass ratio μ and the initial planetary distance parameter ρ_0. The bounding values for μ were given as $[0.220, 0.306]$, i.e., 0.263 ± 0.043, and for ρ_0 as $[0.344, 0.418]$, i.e., 0.381 ± 0.037. I found that based on the MLE as well as a number count of surviving cases (see Sect. 5.3.1) that the existence of the suggested planet in a retrograde orbit is almost certainly possible, whereas in a prograde orbit it is virtually impossible.

For prograde orbits based on the "landscape of survival" (see Figure 5.2), another type of analysis can be given, see Table 5.3. I conclude that for the 9 o'clock planetary starting position and for a relatively high stellar mass ratios, i.e., $\mu \gtrsim 0.25$, the planet must start very close to the star, i.e., that the associated probability for ρ_0 is way outside the statistical 3σ limit. Only for relatively small stellar mass ratios, i.e., $\mu \simeq 0.22$, the planetary starting distance ρ_0 would be barely consistent with the 3σ limit, amounting to a statistical probability of 0.16%. For a 3 o'clock planetary starting position, these probabilities pertaining to the permitted values of ρ_0 are moderately increased. It is found that the associated probabilities for μ given as 0.306, 0.263, and 0.220 are 1.1%, 1.7%, and 2.9%, respectively.

Moreover, it should be noted that this statistical analysis refers to a "landscape of survival" that has been obtained for a timespan of 10,000 binary orbits, corresponding to 29,000 years. An analysis of the evolution of that landscape shows that it tends to dissipate if larger timespans are adopted. Even for timespans of 10,000 binary orbits, there are many parameter combinations (μ, ρ_0) where, concerning prograde orbits, no orbital stability is found even if ρ values are chosen at or beyond the statistical 3σ level.

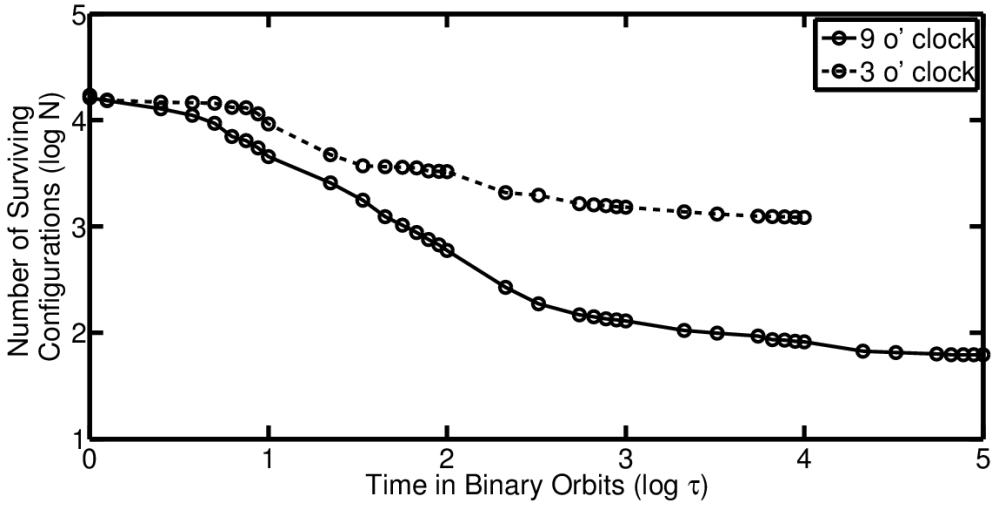

Figure 5.10. Logarithmic representation of the surviving number of configurations as a function of time given in units of completed binary orbits.

Another perspective is offered through Figure 5.10, which provides additional insight into the statistical nature of my simulations. This perspective addresses the view of long term stability. Figure 5.10 depicts two curves representing the number of surviving configurations as a function of time for each starting position in the prograde configuration. The features of this logarithmic plot show that for the first 10 binary orbits there is not a preference towards stability of either starting position.

After 10 binary orbits the 9 o'clock position shows a significantly steeper trend of instability as indicated by the slope of the respective curve. The 3 o'clock position also shows a trend toward instability but it is asymptotically approaching a limit of 10^3 much more smoothly. With these limits, I can estimate the likelihood for a prograde planetary configuration to be extremely small in the framework of long-term simulations. However, for a very large range of (μ, ρ_0) combinations, the stability of retrograde planetary configuration appears almost certainly guaranteed, even for timescales beyond 10^5 binary orbits.

5.4 Summary

This investigation offers detailed insights into the principal possibility of prograde and retrograde orbits for the suggested planet in the ν Octantis system, if confirmed through future observations. A previous study by Eberle & Cuntz (2010a) concluded that the planet is most likely stable if assumed to be in a retrograde orbit with respect to the secondary system component. In the present work, I was able to confirm this theoretical finding, while taking into account the observationally deduced uncertainty ranges of the orbital parameters for the stellar components and the suggested planet as well as different mass ratios of the stellar components.

I also employed additional mathematical methods, particularly the behavior of the maximum Lyapunov exponent (MLE). I found that virtually all cases of prograde orbit became unstable over a short amount of time; the best cases for survival (although barely significant in a statistical framework) were found if a relatively small mass ratio for the two stellar components was assumed and if the initial configuration was set for the planet to start at the 3 o'clock position (Quarles et al. 2012a). This later preference is also consistent with previous general results by Holman & Wiegert (1999) and others. During the time of writing this dissertation, additional study has

been performed using the Arnold web and a much larger computing scheme. Slonina et al. (2012) has shown my results to be consistent with their probe but they could not comment quantitatively on the probability of a retrograde planet within the system.

Thus, my results of the retrograde simulations indicate a high probability for stability within this type of configuration. Moreover, this configuration displays regions in the system where bounded chaos can exist due to the resonances present. Concerning retrograde orbits, there is little preference for the planetary starting position. In summary, I conclude that the ν Octantis star–planet system is an interesting case for future observational and theoretical studies, including additional long-term orbital stability analyses if the suggested planet is confirmed by future follow-up observations.

CHAPTER 6

HABITABILITY OF EARTH-MASS PLANETS AND MOONS IN THE KEPLER-16 SYSTEM

I will demonstrate that habitable Earth-mass planets and moons can exist in the Kepler-16 system, known to host a Saturn-mass planet around a stellar binary, by investigating their orbital stability in the standard and extended habitable zone (HZ). I have determined that Earth-mass planets in satellite-like (S-type) orbits are possible within the standard HZ in direct vicinity of Kepler-16b, thus constituting habitable exomoons. However, Earth-mass planets cannot exist in planetary-like (P-type) orbits around the two stellar components within the standard HZ. Yet, P-type Earth-mass planets can exist superior to the Saturnian planet in the extended HZ pertaining to considerably enhanced back-warming in the planetary atmosphere if facilitated. I will briefly discuss the potential detectability of such habitable Earth-mass moons and planets positioned in satellite and planetary orbits, respectively. The range of inferior and superior P-type orbits in the HZ is between 0.657 to 0.71 AU and 0.95 to 1.02 AU, respectively.

6.1 Background

Kepler-16 constitutes a remarkable binary system containing a circumbinary extra-solar planet as reported by Doyle et al. (2011) and suggested by Slawson et al. (2011). The exoplanet was observed by the NASA Kepler spacecraft using the planetary transit method, which greatly enhances the confidence in the reality of the planet and provides unusually precise information about its physical parameters. There is

a significant previous array of observations of planets in binary and multiple stellar systems (e.g., Patience et al. 2002; Eggenberger et al. 2004; Eggenberger & Udry 2007; Bonavita & Desidera 2007; Mugrauer & Neuhäuser 2009; Raghavan et al. 2010), which also includes a small group of proposed circumbinary planets in contact binaries (with little chance for providing habitable environments) outside the common envelopes of their Roche lobes (Lee et al. 2009; Qian et al. 2010; Beuermann et al. 2010, 2011).

The Kepler-16 system consists of two stars, i.e., the primary with a mass of $M_1 \simeq 0.69\ M_\odot$ and the secondary with $M_2 \simeq 0.20\ M_\odot$, and a giant planet with properties comparable to Saturn. The orbit of the planet is almost circular and encompasses both stars. It takes nearly 229 days for the planet to complete one orbit. The orbits of all three objects are almost precisely confined to one plane (i.e., within 0.5°). Doyle et al. provided detailed information about the orbital and physical parameters of the system; however, they did not address issues concerning the possible habitability of the system. Obviously, it is the ultimate quest of the Kepler Mission to discover Earth-mass planets and moons located in the habitable zones (HZs) of their host stars. Therefore, it is the main objective of this investigation to demonstrate that habitable Earth-mass planets and exomoons in stable orbits are, in principle, possible in the Kepler-16 system. Moreover, such objects can potentially be detected by the currently operating Kepler mission.

6.2 Theoretical Approach

6.2.1 Standard and Extended Habitable Zones

The Kepler-16 system contains two closely orbiting stars ($a_\mathrm{b} = 0.22431$ AU) with the primary (Kepler-16A) producing a substantially larger amount of photo-

metric flux than the secondary (Kepler-16B) (i.e., $F_{\rm B}/F_{\rm A} = 0.01555$). This allows for the calculation of the size of the HZ in this system by solely taking into account the radiation of the primary. I compute the boundaries of the HZ in this system by using the fitting formulas of Underwood et al. (2003) based on the previous work by Kasting et al. (1993) (also using a corrected value for the solar effective temperature), which are categorized by decisive atmospheric conditions of the Earth-mass test planet. Appropriate definitions for the inner and outer boundary of the stellar HZ are based on the runaway and maximum greenhouse effect, respectively, for the planetary atmosphere (see Section 2.3 for details); this standard HZ is found to extend from 0.36 to 0.71 AU for Kepler-16A. This result proves to be also consistent with the more recent work by Selsis et al. (2007) for the case of recent Venus to early Mars-type conditions. In addition, I use the work by Mischna et al. (2000) to calculate the so-called extended HZ, which requires a more extreme planetary atmosphere with significantly enhanced back-warming; its outer boundary extends out to about 2.0 AU in the Solar System (Mischna et al. 2000) and, correspondingly, to 1.02 AU in Kepler-16. With the giant planet (Kepler-16b) positioned at 0.7048 ± 0.0011 AU, it is found to be located very close to the outer edge of the standard HZ, but well within the extended HZ (see Fig. 6.1).

6.2.2 Numerical Methods and System Configurations

The main aim of this research is to investigate numerically the orbital stability of an Earth-mass object (i.e., exoplanet or exomoon) in both the standard and extended HZ of the Kepler-16 system. The numerical methods are based on the Wisdom-Holman mapping technique as well as the Gragg-Burlisch-Stoer algorithm (Grazier et al. 1996). I will integrate the resulting equations of motion forward in time for 1 million years using a fixed/initial (WH/GBS) time step of 10^{-4}. The relative error in

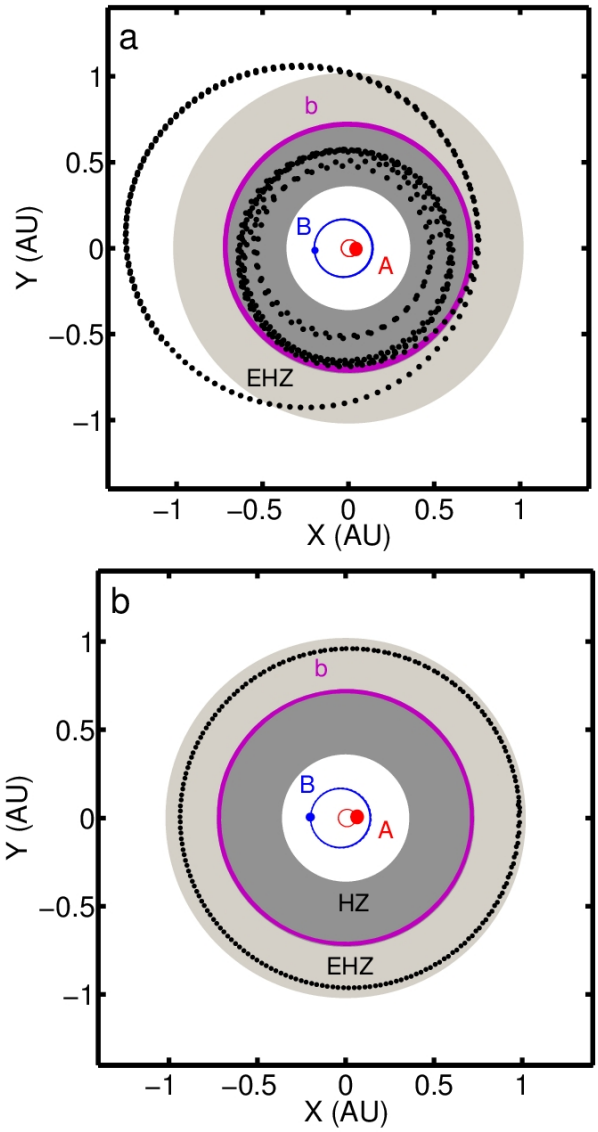

Figure 6.1. (a) Depiction of an unstable P-type Earth-mass planet (*black*) with an initial semi-major axis of $a_0 = 0.504$ AU and an initial eccentricity of $e_0 = 0.06$ to give a starting position at apastron of $x_0 = 0.534$ AU. The stars are given as A (*red*) and B (*blue*). (b) Depiction of a stable P-type Earth-mass planet (*black*) with an initial semi-major axis of $a_0 = 0.951$ AU and an initial eccentricity of $e_0 = 0.03$ to give a starting position at apastron of $x_0 = 0.980$ AU. The dark gray region represents the standard habitable zone (HZ) and the light gray region represents the extended habitable zone (EHZ). The agreement between the orbit of the giant planet Kepler-16b (*purple*) and the outer edge of the standard HZ is coincidental .

energy is calculated to determine when the integration methods fail and the onset of orbital instability occurs. A second check for stability is performed using the method of Lyapunov exponents (see Wolf et al. 1985) with a special emphasis on the maximum Lyapunov exponent (MLE). Our numerical simulations are designated as stable when they terminate with a relative energy error smaller than 10^{-9} and possess a MLE that is asymptotically approaching zero (Quarles et al. 2011).

By adding an Earth-mass object I can consider the Kepler-16 system as a 4-body system; therefore, the Earth-mass object can possibly exist in 6 different orbital configurations. The object can move outside the orbits of the two more massive objects in a planetary (P)-type orbit or around any one of the massive components in a satellite (S)-type orbit. The putative Earth-type object could possibly exist in one of the following classes: 3 S-type orbits (including possible exomoon), 2 P-type orbits, or 1 Trojan exomoon. The S-type configuration would correspond to orbits around Kepler-16A, Kepler-16B, or Kepler-16b, i.e., the Saturnian planet. Due to the general definition of a moon, any S-type orbit revolving around an exoplanet would inherently constitute an exomoon. The P-type orbits would be classified as being either inferior or superior to the Saturnian planet. The Trojan exomoon orbit could exist at either equilateral equilibrium point, L4 or L5.

The numerical setup of the simulations is based on the system parameters presented by Doyle et al. (2011), see Table 6.1, as well as adequate initial conditions. I chose an initial configuration with the more massive stellar component (Kepler-16A) near the center of our barycentric coordinate system. The less massive stellar component (Kepler-16B) is initialized to the left of Kepler-16A at the apastron starting position so that the initial separation of the stars is $a_{\rm b}(1+e_{\rm b}) = 0.260$ AU. Kepler-16b is initialized to the right of the primary at the apastron starting position using the parameters $(a_{\rm p}, e_{\rm p})$ given by Doyle et al. (2011). The Earth-mass object is ini-

tialized to the right of the primary at the apastron starting position. All bodies in this system are given initial velocities in the counter-clockwise direction relative to the center of mass using the known eccentricities of the respective bodies. The initial conditions of the test planet are chosen with respect to the initial starting distance a_0 and eccentricity e_0.

Table 6.1. Stellar and Planetary Parameters of Kepler-16

Parameter	Value[a]
Distance (pc)	~ 61
$F_{\rm B}/F_{\rm A}$	0.01555 ± 0.0001
M_1 ($M_\odot$)	0.6897 ± 0.0035
M_2 ($M_\odot$)	0.20255 ± 0.00066
$T_{\rm eff,1}$ (K)	4450 ± 150
R_1 ($R_\odot$)	0.6489 ± 0.003
$P_{\rm b}$ (d)	41.079220 ± 0.000078
$a_{\rm b}$ (AU)	0.22431 ± 0.00035
$e_{\rm b}$	0.15944 ± 0.00061
$M_{\rm p}$ ($M_{\rm J}$)	0.333 ± 0.016
$a_{\rm p}$ (AU)	0.7048 ± 0.0011
$e_{\rm p}$	0.0069 ± 0.001
$\rho_{\rm p}$ (g cm^{-3})	0.964 ± 0.047

[a] Data as provided by Doyle et al. (2011). All parameters have their usual meaning.

In these simulations I refrain from considering S-type orbits around the stellar components as well as P-type orbits with initial semi-major axes less than the inner boundary of the standard and extended HZ. Since, the aim is to find stable orbits for the test Earth-mass planet within the standard and extended HZ. Therefore, in my computations the parameter a_0 is selected to range from 0.36 to 1.02 AU in increments of 0.001 AU, allowing for the determination of possible P-type planetary orbits as well

as S-type orbits for the exomoon; furthermore, the parameter e_0 is selected to range from 0.0 to 0.5 in increments of 0.01. I also investigate the case of Trojan exomoons with parameters (a_0, e_0) equal to the initial parameters of Kepler-16b, where the exomoon is placed in a position that corresponds to a point preceding Kepler-16b by 60°.

In addition to the full simulations for the 4-body system, I also give an estimate of the outer limit of the S-type orbital stability boundary and the inner limit of the P-type orbital stability boundary using the statistical fitting formulas of Holman & Wiegert (1999). These fitting formulas have been deduced using a range of mass ratios, distance ratios, and eccentricities of binaries regarding the ERTBP. It is important to note that the eccentricity of the test mass is neglected in this study. However, in our application to the elliptical restricted 4-body problem, these fitting formulas will only allow an estimate for test masses of low eccentricity. Since the perturbations due to the giant planet will be small compared to those of the stellar binary components, I implement these formulas neglecting the presence of this planet. This provides a good approximation of the conditions for stability for the S-type orbits around either of the stars, as well as the P-type orbits in close proximity to the inner boundary of the standard HZ. The obtained estimates are then used to guide our numerical study.

6.3 Results and Discussion

Although I refrained from considering S-type orbits around the stellar components through numerical simulation (see Sect. 6.2.2), it is possible to estimate the stability limit of S-type orbits near the stellar components using a statistical fitting formula (Holman & Wiegert 1999). These calculations demonstrate that an Earth-mass planet cannot exist farther than 0.0675 ± 0.0039 AU from the stellar primary

(Kepler-16A) for an S-type orbit due to the perturbations initiated by the stellar secondary (Kepler-16B). This shows that S-type orbits of a habitable Earth-mass planet around either of the stars must be excluded because the stability limit is well within the inner boundary of both the standard and extended HZ (see Sect. 6.2.1). Concerning the P-type orbits inferior to the orbit of the giant planet, my results demonstrate that such orbits are unstable if the semimajor axis is smaller than 0.657 ± 0.011 AU with respect to the stellar primary. However, inferior P-type orbits are still possible if the test Earth-mass planet has a sufficient eccentricity, allowing the giant planet Kepler-16b to capture it as an exomoon.

Since all bodies in my simulations are initialized at their respective apastron starting position, the test planet is also given the appropriate velocity to allow for capture (see Fig. 6.2a). This leaves the principal possibility of a habitable Earth-mass planet in a P-type orbit between 0.657 and 0.71 AU, which means that the planet would be located within the standard HZ. However, short-term secular changes for such orbits allow the giant planet to transfer the Earth-mass planet to an orbit outside the standard HZ within 1,000 years (see Fig. 6.1a), implying that no stable P-type orbits for habitable Earth-mass planets exist inferior to the giant planet. The only stable P-type orbits for Earth-mass planets are those located superior to the giant planet. My results show that these orbits become stable once their semimajor axes are 0.95 AU or higher, which places them within the extended HZ (see Fig. 6.1b).

The last class of orbits include those that could result in an habitable exomoon in either an S-type or Trojan configuration. A stable S-type orbit for such an exomoon can be achieved through two separate scenarios. The first scenario is based on the assumption that the possible exomoon formed together with the giant planet, ignoring migration. The second scenario is based on the assumption that the putative exomoon formed initially in a P-type orbit and was captured by the giant planet as a result of

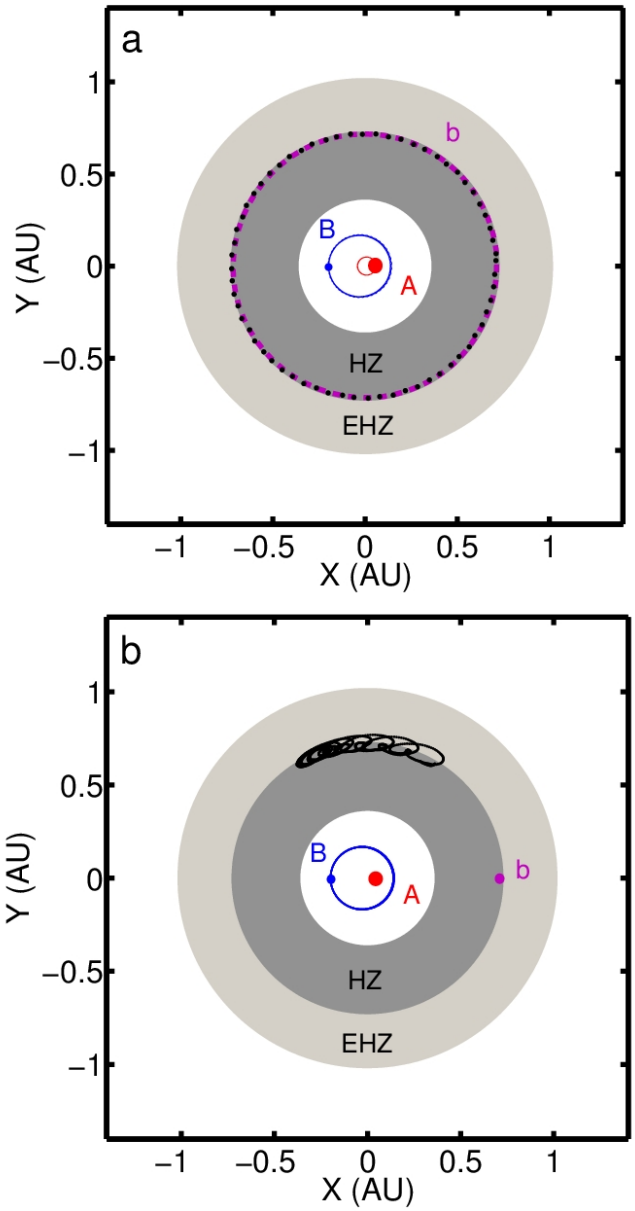

Figure 6.2. (a) Depiction of an S-type *captured* Earth-mass exomoon (*black*) with an initial semi-major axis of $a_0 = 0.619$ AU and an initial eccentricity of $e_0 = 0.13$ to give a starting position at apastron of $x_0 = 0.699$ AU. The stars are given as A (*red*) and B (*blue*). (b) Depiction of a possible Trojan exomoon in a rotating reference frame (*black*) with an initial semi-major axis of $a_0 = 0.7048$ AU and an initial eccentricity of $e_0 = 0.0069$ to give a starting position at apastron of $x_0 = 0.710$ AU. The dark gray region represents the standard habitable zone (HZ) and the light gray region represents the extended habitable zone (EHZ). The agreement between the orbit of the giant planet Kepler-16b (*purple*) and the outer edge of the standard HZ is coincidental. (Quarles et al. 2012b) .

migration. This provides additional justification for considering the eccentricity e_0 as a free parameter because the initial state of the capture remains unknown.

The first scenario which involves the exomoon forming from a secondary circumplanetary disk can be estimated through the concept of Hill stability. Similar to the estimations made by Holman & Wiegert (1999) for the elliptical 3-body problem, there have been simulations to determine an approximate stability limit for exomoons orbiting extrasolar giant planets (Domingos et al. 2006; Kaltenegger 2010). These previous general estimations can be used to guide the investigation of this case. Simulations of this scenario were performed by incrementing the parameter e_0 exactly as before, but the parameter a_0 has been incremented relative to the starting position of the Saturnian planet starting from 0.0001 to 0.0240 AU in increments of 0.0001 AU. The stability boundaries are expected to occur near the Roche limit (inner) and the estimated Hill limit for prograde motion (outer).

The inner boundary is calculated using the given density (see Table 6.1) of the Saturnian planet and that of Earth, i.e., 5.515 g cm^{-3}. The Earth mean density has been chosen because it best represents what would be considered as Earth-like. Alternatively, the density could be varied as a function of a_0, but our usage of the density is limited to the calculation of the Roche limit about the Saturnian planet. Planetary formation calculations for this system should be considered in future studies to constrain the mass and densities of possible moons orbiting Kepler-16b, which are however outside the scope of this research. I also calculated the outer boundary assuming a circular orbit (i.e., $e_0 = 0.0$) because it gives the maximum stability as more eccentric orbits have been shown to decrease the stability region (e.g., Domingos et al. 2006). Thus the inner and outer boundaries are estimated as 0.0004 and 0.0168 AU, respectively.

Through my numerical simulation I have determined the stability boundaries to be commensurate with the previous estimates. The stability analyses of these orbits have undergone similar scrutiny in the relative error in energy and maximum Lyapunov exponent. Although I investigated the possibility of eccentric orbits in this scenario, my results show that the stability decreases dramatically as eccentricity is increased so that most of the stable orbits discovered were nearly circular (see Fig. 6.3a). I point out that this result is also in accordance with the known parameters of the most massive satellites of Jupiter and Saturn. In addition, my results show that instabilities at the outer boundary lead to ejection and are insensitive to the choice of e_0 (see Fig. 6.3b).

The second scenario which involves the exomoon attained through capture may be much less probable. However, I determined that there are P-type orbits, where the proper eccentricity can lead to capture into S-type orbits (see Fig. 6.2a). The results presented in this figure were obtained with $a_0 = 0.619$ AU and the initial starting distance $x_0 = 0.699$ AU, which is superior to the estimated stability limit of 0.657 AU. This places the test planet within the Hill sphere, corresponding to a Hill radius of 0.034 AU from the giant planet, which shows that the influence of the giant planet ranges radially from 0.67 to 0.73 AU with respect to the center of mass. A general trend is that the circular P-type orbits inferior to the giant planet are generally too fast for capture; hence, I considered eccentric orbits. Moreover, the P-type orbits superior to the giant planet are generally too slow for capture resulting in either collision with the giant planet or ejection from the system. However, detailed assessments of the probability of exomoon's capture are beyond the scope of this research.

If migration occurred in this system during its formation, this would be the preferred scenario; it would entail a number of ways for a putative exomoon to avoid

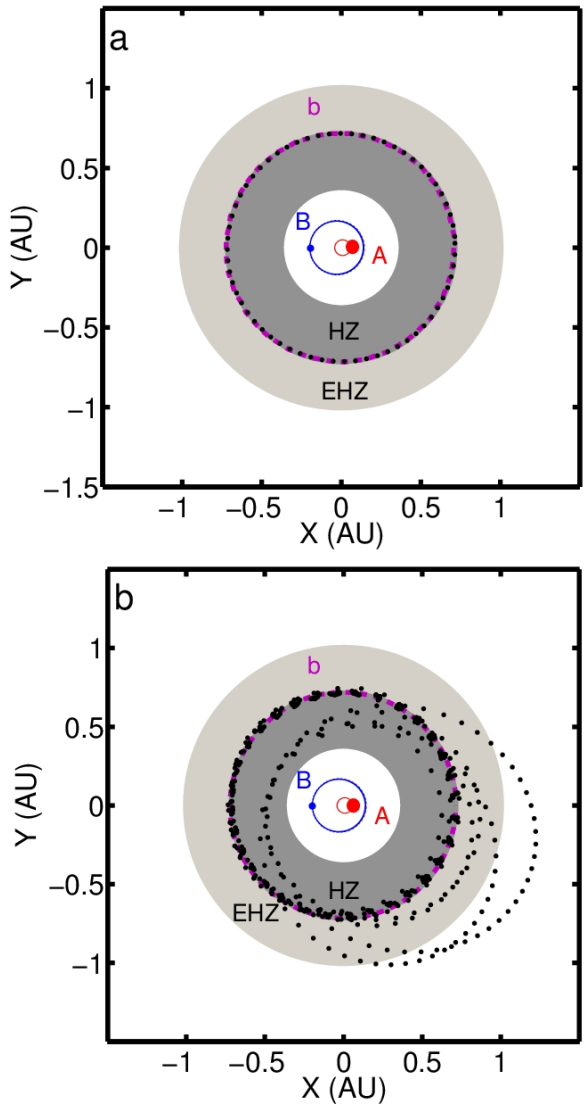

Figure 6.3. (a) Depiction of a stable S-type *coformed* Earth-mass exomoon (*black*) with an initial semi-major axis of $a_0 = 0.715$ AU and an initial eccentricity of $e_0 = 0.0$. The stars are given as A (*red*) and B (*blue*). (b) Depiction of an unstable S-type *coformed* Earth-mass exomoon (*black*) with an initial semi-major axis of $a_0 = 0.721$ AU and an initial eccentricity of $e_0 = 0.0$. The dark gray region represents the standard habitable zone (HZ) and the light gray region represents the extended habitable zone (EHZ). The agreement between the orbit of the giant planet Kepler-16b (*purple*) and the outer edge of the standard HZ is coincidental .

a chaotic orbit (Kipping 2011). The constraints on natural satellite formation in the Solar System were previously investigated by (Canup & Ward 2006), who also determined the available mass in the circumplanetary disk. However, the latter may not be applicable to the more exotic case of the Kepler-16 system since the Saturn-like planet exists in close proximity to the so-called snow line. This makes both scenarios (circumplanetary disk formation and capture) to appear equally likely since the migration distance may have been small. Further planetary formation investigations need to be performed to determine a more unique solution.

Finally, I considered the possibility of a Trojan exomoon. The stability of this possible exomoon is ensured by the fact that the mass ratio ($\mu = M_3/M$ with $M = M_1+M_2+M_3$ and $m_3 = M_{\rm p}$) can be calculated and be used as a stability condition for the approximate 3-body problem. This approximation proves to be valid because the proposed Trojan exomoon would always reside at a semi-major axis commensurate with Kepler-16b at the appropriate distance leading or trailing Kepler-16b (see Section 6.2.2). Considering the case where the binary system can act like a point source at the center of mass, I then find the mass ratio, $\mu = 0.000357$, which is much less than the critical value for Trojans, $\mu_0 = 0.03852\ldots$ (Szebehely 1967). My results obtained for this configuration show that stable Trojans can exist even if the perturbations by Kepler-16B are not completely negligible (see Fig. 6.2b). The influence of Kepler-16B can transfer the proposed Trojan exomoon from its equilibrium point but it is insufficient to create an instability; instead, the Trojan exomoon would precess along the orbit of Kepler-16b.

6.4 Summary

By performing numerical simulations I have explored the possibility of a habitable Earth-mass object in the Kepler-16 system. Although it is beyond the scope

of this dissertation to determine whether such an object exists, I am able to provide information through my orbital stability analyses where to search for it in the realm of further observations. I have considered the standard and extended HZ of the system and investigated 6 different orbital configurations. The obtained results show that S-type planetary orbits about either of the stellar components as well as P-type planetary orbits inferior to Kepler-16b's orbit exhibit short-term orbital instabilities. These instabilities would inhibit any form of habitability due to the ejection, collision, or the occurrence of highly eccentric orbits for any possible object (if it had formed). My main result about habitable Earth-mass planets in this system is that the only stable P-type orbits for such planets are those located superior to Kepler-16b's orbit (Quarles et al. 2012b). Specifically, these orbits become stable once the semimajor axis is 0.95 AU or higher, which places them within the extended HZ. The range of habitable inferior and superior P-type orbits in the HZ is between 0.657 to 0.71 AU and 0.95 to 1.02 AU, respectively.

The numerical simulations of S-type orbits for an Earth-mass moon captured by the giant planet or formed through a circumplanetary disk show that such orbits are stable and moreover located in the standard HZ. A highly relevant aspect of the existence of an exomoon orbiting Kepler-16b is that it may help explain the variation between the observed eccentricity and its previously reported value from numerical study (Doyle et al. 2011). Similar to the effects of Earth's Moon, the exomoon could exert possible tidal forces, through a stabilizing torque and angular momentum exchanges, freezing the eccentricity of Kepler-16b at the observationally determined value of 0.0069. As the observations may just be a snapshot in time, other hypotheses concerning the Kozai Mechanism, driving of eccentricity through planet-planet interactions, or possible exomoons, can be considered equally likely and cannot be uniquely identified until further investigations of the system have been performed

(Laskar & Robutel 1993b; Barnes & Greenberg 2008). Since the exomoon would lie on the outer edge of the HZ, tidal heating could also play a role in increasing the prospects of habitability (Barnes et al. 2009; Dressing et al. 2010). I also considered the possibility of a Trojan exomoon present at one of the equilateral Lagrange points. This is an intriguing case as the exomoon would precess and display a variety of different orbits about L4 or L5, which are all located within the standard HZ (Quarles et al. 2012b). Hence, the existence of habitable exomoons around Kepler-16b is an exciting scenario for facilitating habitability in the Kepler-16 system.

Finally, I want to point out that an Earth-mass planet or moon can potentially be detected by the current Kepler mission. Our suggestion is based on the work by Kipping et al. who provided evidence that Kepler's instruments should indeed be capable of detecting such objects, specifically, the possible exomoon. In general, Kepler should be able to detect exomoons as small as 0.2 $M_{\oplus}$ if observers look for the transit timing effects discussed by Kipping et al. (2009). In addition, the realm of circumbinary planets similar to Kepler-16b may prove to be an adequate region for discovering exomoons as it would be possible to obtain the necessary statistical constraints of detection. The 220-day period the Saturnian planet makes it possible to observe 6 transits within 3.6 years of observation, which is well within the extended mission life time of the Kepler spacecraft. It is also noteworthy that the distance to the Kepler-16 is only about 61 parsec, which places the system well within the distance range (0.68 – 386 pc) for detecting Earth-mass planets and exomoons around K and M-type stars.

CHAPTER 7

HABITABILITY OF EARTH-MASS TROJAN PLANETS AND MOONS IN THE HD 23079 SYSTEM

I investigate the possibility of habitable Trojan planets in the HD 23079 star-planet system. Since this reseach is part of a collaboration, I will only discuss what is necessary to convey the main argument of the research with emphasis on my contribution (see Eberle et al. (2011) for a more detailed discussion). This system consists of a solar-type star and a Jupiter-type planet, which orbits the star near the outer edge of the stellar habitable zone in an orbit of low eccentricity. It is determined that in agreement with previous studies Earth-mass habitable Trojan planets are possible in this system, although the success of staying within the zone of habitability is significantly affected by the orbital parameters of the giant planet and by the initial condition of the theoretical Earth-mass planet. In one of the simulations, the Earth-mass planet is captured by the giant planet and thus becomes a habitable moon.

7.1 Background

The existence of planets in orbit about solar-type stars is now a well-established observational result. Obviously, the ultimate quest of these studies is to discover Earth-like planets located in the habitable zones (HZs) of their host stars. So far, a small number of super-Earth planets with masses of up to about 12 $M_{\oplus}$ (e.g., Udry et al. 2007; Vogt et al. 2010) have been found, typically located around M-type dwarf stars. Nevertheless, the existence of Earth-mass planets, including those hosted by solar-type stars, is strongly implied by various observational findings including the

occurrence and mass distribution of close-in super-Earths, Neptunes, and Jupiters (Howard et al. 2010). Measurements by the authors indicate an increasing planet occurrence with decreasing planetary mass M_p akin to $M_p^{-0.48}$, implying that 23% of stars harbor a close-in Earth-mass planet (ranging from 0.5 to 2.0 $M_\oplus$); see also Marcy & Butler (2000) for earlier results. Very recent support for the existence of Earth-type planets outside the Solar System is lent by the discovery of Kepler-10b, Kepler's first rocky planet with an estimated mass of 4.6 Earth masses (Batalha et al. 2011).

Long-term orbital stability of Earth-like planets in stellar HZs is necessary for the evolution of any form of life, particularly intelligent life. There is a large array of studies focusing on the orbital stability of hypothetical Earth-mass planets in stellar HZs concerning different types of host stars and star-planet configurations. Examples include studies by Gehman et al. (1996), Jones et al. (2001, 2005, 2006), Jones & Sleep (2010), Noble et al. (2002), Menou & Tabachnik (2003), Cuntz et al. (2003), von Bloh et al. (2003), and Asghari et al. (2004). Particular types of systems are those where a Jupiter-type planet orbits a star in the stellar HZ, therefore jeopardizing the possibility of habitable terrestrial planets in that system. This is actually the situation of HD 23079.

Previously, Noble et al. (2002) investigated the orbital stability of terrestrial planets inside the HZs of 47 UMa and HD 210277. The center stars of these systems are very similar to the Sun concerning mass, spectral type, and effective temperature. Orbital stability was attained for the inner part of the HZ of 47 UMa; however, no orbital stability was found for hypothetical Earth-mass planets in the HZ of HD 210277. In this case, a Jupiter-type planet crosses the stellar HZ, thus effectively thwarting habitability for this system. Very recent examples were also given by Yeager et al. (2011) who studied the star-planet systems HD 20782 and HD 188015. In both cases,

the giant planet significantly interferes with any Earth-mass planet in the stellar HZ assumed to have formed there for the sake of study. In all cases, the Earth-mass planet was ejected from the stellar HZ in a very short time.

However, if a giant planet is orbiting the star in the stellar HZ, there is still the principal possibility of habitable Trojan planets in those systems as pointed out by, e.g., Dvorak et al. (2004) and Schwarz et al. (2007). A Trojan planet is one located around one of the Lagrangian points L4 and L5 of the giant planet. These points lie on the giant planets orbit, ahead (L4) and behind (L5) the planet, each forming an equilateral triangle with the planet and its star. Thus, Trojan planets are also in a 1:1 resonance with the giant planet. Dvorak et al. (2004) investigated the stability regions of hypothetical terrestrial planets around L4 and L5 in specific systems, including HD 23079, in the framework of the restricted three body problem. They obtained relationships between the size of the stability regions and the orbital parameters of the giant planets, particularly its eccentricity. Studies about Neptune Trojans were given by, e.g., Dvorak et al. (2007).

A study by Schwarz et al. (2007) identified several exoplanetary systems that can harbor Trojan planets with stable orbits in the stellar HZs. Concerning HD 23079, this study concluded that a Trojan planet will only spend 35% of its time in the stellar HZ, assumed to extend from 0.85 to 1.60 AU. In my study, however, I will consider a zone of habitability based on the generalized estimate by Underwood et al. (2003), implying habitability between 0.99 and 1.97 AU (see below). This means that the habitable area, which is the area of the stellar HZ annulus, is increased by 58% compared to that considered by Schwarz et al. (2007). In the present study, I will conclude that habitable Trojan planets are indeed possible in the system of HD 23079, although their existence is significantly affected by, e.g., the orbital parameters of the giant planet.

7.2 Theoretical Approach

7.2.1 Stellar and Planetary Parameters

HD 23079 has been monitored as part of the Anglo-Australian Planet Search (AAPS) program (Tinney et al. 2002) that is able to perform extrasolar planet detection and measurements with a long-term, systematic radial velocity precision of 3 m s^{-1} or better. HD 23079 was identified to host a Jupiter-type planet in a relatively large and nearly circular orbit. HD 23079 is an inactive main-sequence star; Gray et al. (2006) classified it as F9.5 V (see Table 7.1; all parameters have their usual meaning), an updated result compared to Houk & Cowley (1975) who found that HD 23079 is intermediate between an F8 and G0 star. Its stellar spectral type corresponds to a mass of $M = 1.10 \pm 0.15\ M_{\odot}$. The stellar effective temperature and radius are given as $T_{\rm eff} = 6030 \pm 52$ K and $R = 1.106 \pm 0.022\ R_{\odot}$, respectively (Ribas et al. 2003). Thus, HD 23079 is fairly similar to the Sun, though slightly hotter and slightly more massive. The detected planet (HD 23079 b) has a minimum mass of $M_p \sin i = 2.45 \pm 0.21\ M_J$. Furthermore, it has a semimajor axis of $a_p = 1.596 \pm 0.093$ AU and an eccentricity of $e_p = 0.102 \pm 0.031$ (Butler et al. 2006), corresponding to an orbital period of $P = 730.6 \pm 5.7$ days. The original results by Tinney et al. (2002) indicated very similar planetary parameters.

The orbital parameters of HD 23079 b are relatively similar to those of Mars, implying that HD 23079 b is orbiting its host star in or near the outskirts of the stellar HZ; see discussion below. The existence of HD 23079 b, a planet even more massive than Jupiter, makes it difficult for a terrestrial planet to orbit HD 23079 at a similar distance without being heavily affected by the giant planet; see results from previous case studies by Noble et al. (2002) and Yeager et al. (2011) who focused on the dynamics of HD 20782, HD 188015, and HD 210277. Concerning HD 23079, a

Table 7.1. Stellar and Planetary Parameters of HD 23079

Parameter	Value	Reference
Parameter	Value	Reference
Spectral Type	F9.5 V	Gray et al. (2006)
RA	3 39 43.0952	ESA (1997)[a,b]
DEC	− 52 54 57.017	ESA (1997)[a,b]
$T_{\rm eff}$ (K)	6030 ± 52	Ribas et al. (2003)
R ($R_\odot$)	1.106 ± 0.022	Ribas et al. (2003)
M ($M_\odot$)	1.10 ± 0.15	[c]
M_V	4.42 ± 0.05	ESA (1997)[a,b,d]
$M_{\rm bol}$	4.25 ± 0.05	ESA (1997)[a,b,d]
Distance (pc)	34.60 ± 0.67	ESA (1997)[a,b,d]
$M_p{\rm sin}i$ (M_J)	2.45 ± 0.21	Butler et al. (2006)
P (days)	730.6 ± 5.7	Butler et al. (2006)
a_p (AU)	1.596 ± 0.093	Butler et al. (2006)
e_p	0.102 ± 0.031	Butler et al. (2006)

[a] data from SIMBAD, see `http://simbad.u-strasbg.fr`
[b] adopted from the *Hipparcos* catalogue
[c] based on spectral type
[d] based on parallax 28.90 ± 0.56 mas

previous investigation pertaining to habitable terrestrial Trojan planets was given by Dvorak et al. (2004).

7.2.2 Method of Integration

For the simulations of the HD 23079 system, we consider both the observed giant planet and a hypothetical terrestrial planet of one Earth-mass, i.e., 3.005×10^{-6} $M_\odot$, which allows us to execute a grid of model simulations. The method of integration uses a fourth-order Runge-Kutta integration scheme (Garcia 2000). The code has been extensively tested against known analytical solutions, including the two-body and restricted three-body problem (see Noble et al. 2002; Cuntz et al. 2007; Eberle et al. 2008, for detailed results). In the framework of our simulations that we limit to

10^6 yrs, we apply a time-step of 10^{-4} yrs for the integration scheme that is found to be fully appropriate. In that regard, we pursued test studies comparing the planetary orbits based on three different integration time-steps, which are: 10^{-3}, 10^{-4} and 10^{-5} yrs. In particular, we evaluated ΔR_{ij}, i.e., the magnitude of the difference between the position of the planet when different step sizes of 10^{-i} and 10^{-j} were used. We found that there is no significant change in outcome between models with time-steps of 10^{-4} and 10^{-5} yrs.

The initial conditions (i.e., starting velocities) for the orbits of the Earth-mass planets were chosen such that the planet was assumed to start at the midpoint of the stellar HZ (1.4779 AU) and to be in a circular orbit about the star, although it is evident that it will be significantly affected immediately by gravitational pull of the giant planet, which will prevent the planet from continuing a circular motion. For each set of models, defined by sets of values for the semimajor axis a_p and eccentricity e_p, given as 1.503, 1.596, 1.689 AU and 0.071, 0.102, 0.133, respectively, 8 different configurations are considered. They are defined by the 8 different starting (arguments of pericenter) angles for the Earth-mass planet, which are varied in increments of 45° noting that 0° corresponds to the 3 o'clock position. Moreover, the starting position of the Jupiter-type planet (HD 23079 b), for which we assume its minimum mass value of 2.45 M_J, was varied between its periastron and its apastron position. Therefore, a total of 144 initial configurations has been considered. Note that the Jupiter-type planet was always started at the 3 o'clock position, which after adjusting the orbital layout of the giant planet always coincided with its periastron (see Figure 7.1) or apastron position depending on the type of model.

7.2.3 Stellar Habitable Zone

The extent of the HZ of HD 23079 has been calculated following the formalism by Underwood et al. (2003) based on previous work by Kasting et al. (1993). Underwood et al. (2003) supplied a polynomial fit depending on the stellar luminosity and the stellar effective temperature that allows to calculate the extent of the conservative and the generalized HZ. Noting that HD 23079 is more luminous than the Sun, it is expected that its HZ is more extended than the solar HZ, for which the inner and outer limit of the generalized HZ were given as 0.84 and 1.67 AU, respectively (Kasting et al. 1993). The generalized HZ is defined as bordered by the runaway greenhouse effect (inner limit), where water vapor enhances the greenhouse effect thus leading to runaway surface warming, and by the maximum greenhouse effect (outer limit), where a surface temperature of 273 K can still be maintained by a cloud-free CO_2 atmosphere. The inner limit of the conservative HZ is defined by the onset of water loss, i.e., the atmosphere is warm enough to allow for a wet stratosphere from where water is gradually lost by photodissociation and subsequent hydrogen loss to space (see Section 2.3 for more details). Furthermore, the outer limit of the conservative HZ is defined by the first CO_2 condensation attained by the onset of formation of CO_2 clouds at a temperature of 273 K.

For HD 23079, the limits of the conservative HZ are given as 1.1378 and 1.6362 AU, whereas the limits of generalized HZ are given as 0.9896 and 1.9662 AU (see Figure 7.1). The limits of the generalized HZ are those employed in our numerical planetary studies[1]. The underlying definition of habitability is based on the assumption that liquid surface water is a prerequisite for life, a key concept that is also the basis of ongoing and future searches for extrasolar habitable planets (e.g.,

[1]The physical limits of habitability are much less stringent than implied by the numerical precision of these values; nevertheless, these values were used for checking if the Earth-mass planet has left the stellar HZ.

Catanzarite et al. 2006; Cockell et al. 2009). The numerical evaluation of these limits is based on an Earth-type planet with a $CO_2/H_2O/N_2$ atmosphere. Specifically, the inner limit of habitability is set by the loss of water from the upper planetary atmosphere through photodissociation and subsequent escape of hydrogen to space associated with a run-away greenhouse effect. The outer limit of habitability is given by the maximum greenhouse effect (Kasting et al. 1993; Underwood et al. 2003), by which a surface temperature of 273 K can be maintained by a cloud-free CO_2 atmosphere.

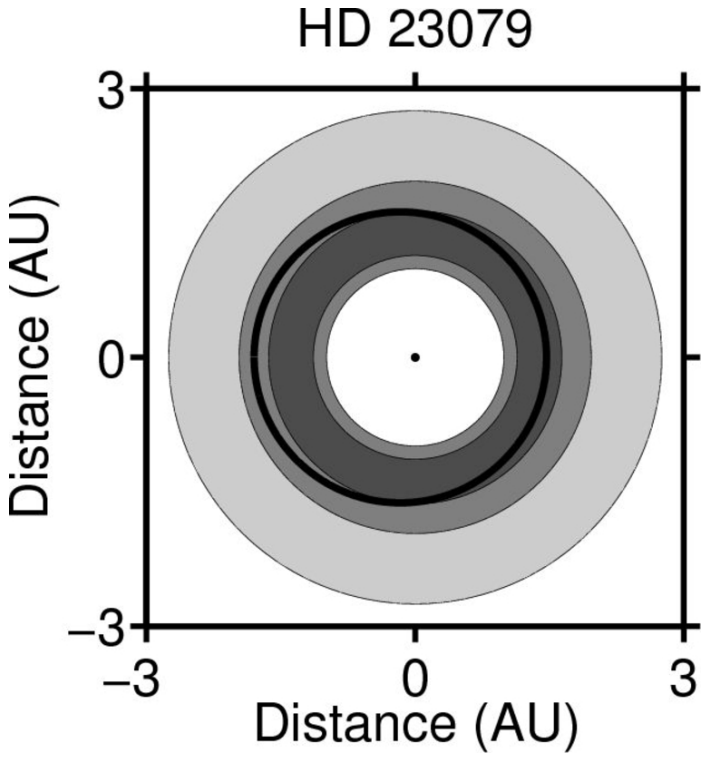

Figure 7.1. Extent of the HZ for HD 23079, defined by its conservative limits (dark gray) and generalized limits (medium gray). The outer limit of an extreme version of the generalized HZ (light gray) is depicted following the work by Mischna et al. (2000), although this limit may be unrealistic based on subsequent studies. The orbit of HD 23079 b, a Jupiter-type giant planet, is depicted by a thick solid line. Image Credit: Eberle et al. (2011) .

We point out that concerning the outer edge of habitability, even less conservative limits have been proposed in the meantime (e.g., Forget & Pierrehumbert 1997; Mischna et al. 2000). They are based on the assumption of relatively thick planetary CO_2 atmospheres and invoke strong back-warming that may further be enhanced by the presence of CO_2 crystals and clouds. However, as these limits, which can be as large as 2.4 AU in case of the Sun, depend on distinct properties of the planetary atmosphere, they are not relevant for our study. Nevertheless, we convey this type of limit for the sake of curiosity (see Figure 7.1), noting that it has properly been adjusted to 2.75 AU in consideration of the radiative conditions of the planetary host star, HD 23079. Moreover, the significance of this extreme limit has recently been challenged based on detailed radiative transfer simulations (Halevy et al. 2009).

7.3 Results and Discussion

7.3.1 Case Studies of Habitable Trojan Planets

An Earth-mass planed was considered in 144 total initial configurations where 13 survived at least 1 million years, 93 crossed the upper limit of the HZ, 28 crossed the lower limit of the HZ, and 10 collided or may have had a very close approach with the giant planet. Some of those who crossed the HZ at the lower or upper limit as first exit from the HZ may have had a very close approach with the giant planet, resulting in destruction while entering the Roche limit (Williams 2003) or in a collision with the giant planet, at a later time. Of the 13 survivors, 12 are Trojan types, that is they exist in stable orbits around the equilateral equilibrium positions much like that demonstrated in Dvorak et al. (2004).

One such simulation considers when the giant planet is placed at apastron with $a_p = 1.503$ AU, $e_p = 0.102$ and the Earth-mass planets placed at four different starting

angles (see Figure 7.2). The starting angles position the proposed Earth-mass planet as a Trojan exomoon and remain in the HZ for 10^6 yrs of simulation time. Since the Earth-mass Trojan planets resided near the "banana-shaped" area at L4 or L5, they experience minimal perturbations from the two larger masses ensuring stability. In addition the mass ratio ($\mu = 0.00212\ldots$) is sufficiently small (see Section 6.3) to host an Earth-mass planet at the equilateral equilibrium points.

For the sake of curiosity, I also evaluated various cases where the Earth-mass planet never had a chance of becoming habitable. Hence, I chose five cases of different semimajor axes and eccentricities for the giant planet. In all cases the giant planet started at the periastron position and the initial phase angle of the Earth-mass planet was chosen as 180°. The simulations are depicted in Figure 7.3. In Figure 7.3a, with $a_p = 1.503$ AU and $e_p = 0.102$, the system experiences a relatively long period during which the Earth-mass planet first exits the HZ at 48.4 yrs. This event is preceded by a close approach with the giant planet. The simulation is terminated at 195.9 yrs due to an expected collision with the giant planet.

Figures 7.3b to 7.3d are all based on $a_p = 1.596$ AU, but the depicted simulations assume different eccentricities for the giant planet, which are $e_p = 0.071$, 0.102, and 0.133, respectively. In Figure 7.3b, the system experiences a short period during which the Earth-mass planet first exits the HZ at 7.93 yrs. This event is again preceded by a close approach with the giant planet. The simulation is terminated at 9,112 yrs due to the expected collision with the giant planet. In Figure 7.3c, the system experiences a short period during which the Earth-mass planet first exits the HZ at 7.80 yrs. This event is preceded by a close approach with the giant planet. The simulation is terminated at 13,400 yrs considering that the Earth-mass planet is ejected from the system. Habitability is ultimately prevented as the Earth-mass planet becomes "free-floating". Free-floating planets have previously been observed

in case of the Trapezium cluster (Lucas & Roche 2000); note that planetary ejections due to orbital instabilities are an important candidate process for this finding.

In Figure 7.3d, with $a_p = 1.596$ AU and $e_p = 0.133$, this system experiences a short period during which the Earth-mass planet first exits the HZ at 7.82 yrs. It is reentering and exiting the HZ several times. However, the simulation is terminated at 54.60 yrs due to an expected collision with the giant planet. In case of Figure 7.3e, with $a_p = 1.689$ AU and $e_p = 0.102$, the system again experiences a short period during which the Earth-mass planet first exits the HZ at 4.78 yrs. This event is preceded by a close approach with the giant planet. Eventually, the planet also becomes free-floating; the simulation is terminated at about 7×10^4 yrs. Figure 7.3a and 7.3d show oscillatory behaviors regarding the orbital motion of the Earth-mass planet. Noting that the Earth-mass planet starts at a phase angle of 180°, it initially orbits the star. However, when it approaches the giant planet, its orbit is being perturbed causing the loops. Thus, the Earth-mass planet exits and re-enters the HZ multiple times until the end of the simulation.

7.3.2 On the Possibility of Habitable Moons

The set of model simulations considered reveal a variety in the dynamics of the Earth-mass planet. The most surprising case is the following: For $a_p = 1.596$ AU and $e_p = 0.133$ (see Figure 7.4) with the Jupiter-type planet initially placed at periastron position and the Earth-mass planet placed at 0°, it was found that the latter never crosses the inner or outer limit of the stellar HZ during the simulation time of 10^6 years. However, it is found to orbit the giant planet in a retrograde orbit (relative to the orbital motion of the giant planet about the star). In this case, the Earth-mass planet is captured by the giant planet and becomes a habitable moon, which occurs almost immediately after the start of the simulation.

The analysis of its orbital data shows that the moon's semimajor axis concerning its motion about the giant planet is $a_{\rm moon} \simeq 0.051$ AU. Its eccentricity is $e_{\rm moon} \simeq 0.8$ entailing a perigee and apogee of 0.0034 and 0.098 AU, respectively. Thus, with a uniform data sampling rate, the moon is most likely to be recorded at or near apogee. The existence of a habitable moon in the HD 23079 system is also consistent with the criterion of Hill stability as pointed out by, e.g., Donnison (2010). This study explores dynamic Hill stability for a large variety of three-body systems considering moon/planet mass ratios of 0.1, 0.01 and 0.001.

There is a persistent interest in the study of habitable moons with respect to extrasolar giant planets orbiting host stars in the stellar HZs. Previous studies of habitable moons in systems akin to HD 23079 have been given by Williams & Kasting (1997), Barnes & O'Brien (2002), and others. The study by Williams & Kasting (1997) did not include HD 23079b as this star-planet system was unknown at the time when this study was pursued. However, by targeting the companions of 16 Cyg B and 47 UMa, Williams & Kasting (1997) investigated appropriate orbital parameters of possible moons, and pointed out that the moons need to be large enough (i.e., $> 0.12\ M_{\oplus}$) to retain a substantial and long-lived atmosphere, and furthermore would need to possess a significant magnetic field to prevent its atmosphere from being sputtered away by the ongoing bombardment of energetic ions from the planet's magnetosphere, if existing. Another study of possible moons, which is fully applicable to the HD 23079 star-planet system, has been given by Barnes & O'Brien (2002). They concluded that Earth-like moons of a Jovian planet like HD 23079b would be able to exist for at least 5 Gyr considering that the stellar mass of HD 23079 exceeds $0.15\ M_{\odot}$.

7.4 Summary

The aim of our study was to add to the investigation of habitable Trojan planets in the HD 23079 star-planet system. This system consists of a main-sequence star slightly hotter than the Sun. Additionally, it contains a Jupiter-type planet with a minimum mass of 2.45 M_J that is orbiting the star in a slightly elliptical orbit that is positioned within the stellar HZ. The main goal of our study was to explore if Earth-mass habitable Trojan planets can exist in this system (Eberle et al. 2011).

As the centerpiece of our study, we calculated a total of 144 orbital stability simulations for the Earth-mass planet by choosing different starting positions (phase angle) as well as placing the Jupiter-type planet either at periastron or apastron position. The attainment of habitability solutions was found to critically depend on various parameters, which include the orbital parameters of the giant planet (semi-major axis, eccentricity) and the initial condition (phase angle) of the theoretical Earth-mass planet. We encountered a variety of different outcomes, which include (1) ejection of the Earth-mass planet from the system, (2) engulfment of the planet by the star (or possible destruction in accord with the Roche limit criterion), (3) capture of the planet, thus becoming an habitable moon, or (4) remaining within the stellar HZ. The latter case was only attained in models where the orbit of the giant planet had a relatively low eccentricity (but still within its observationally given uncertainty), which however may be partially due to the implemented choice of planetary starting positions. Concerning the latter case, there were also cases (not shown in detail) where the planet took short-term excursions (Eberle et al. 2011) from the HZ (i.e., considerably less than the orbital period of HD 23079b, which is about 730 d), which should be insufficient to nullify its habitability because the latter is expected to mainly depend on the average stellar flux received over an entire orbit, rather than the length of the time spent within the HZ (Williams & Pollard 2002), although the ultimate

effect of temporarily leaving the zone of habitability will still partially depend on the atmospheric thickness, structure and composition (e.g., Dressing et al. 2010).

Moreover, we note that our study is supplementing previous work by Schwarz et al. (2007) who concluded that a Trojan planet in the HD 23079 star-planet system will only spend 35% of its time in the stellar HZ. However, this estimation was based on a considerably narrower zone of habitability than used in the present study. Another, albeit minor, difference is that Schwarz et al. (2007) used slightly different orbital parameters for HD 23079b than in the current study. In conclusion, it can be argued that the system of HD 23079 is very well suited for the existence of habitable Earth-type Trojan planets, and thus deserves serious consideration in ongoing and future planetary search missions.

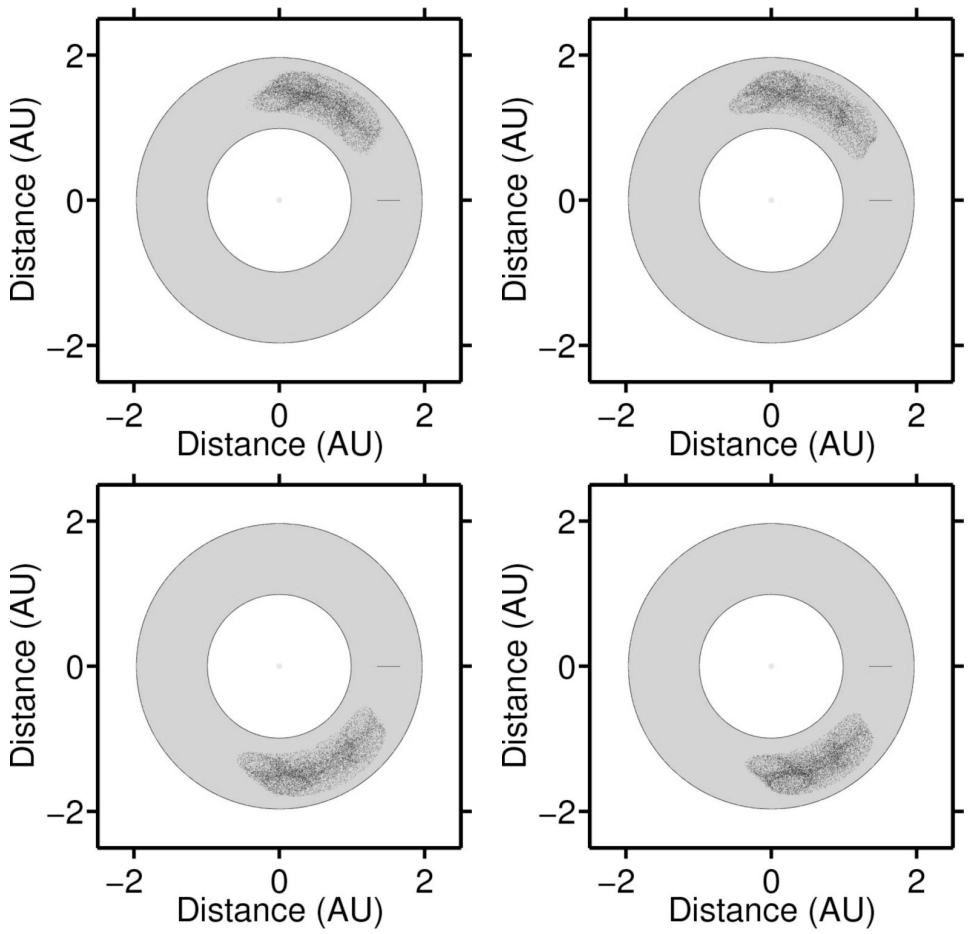

Figure 7.2. Orbital stability simulations with HD 23079 b initially placed at apastron with $a_p = 1.503$ AU, $e_p = 0.102$ and the Earth-mass planets placed at four different starting angles, which are: 45° (top left), 90° (top right), 270° (bottom left), and 315° (bottom right). Using a rotating coordinate system, HD 23079 b moves along the thin line. The Earth-mass Trojan planets, which give rise to the "banana-shaped" area at L4 or L5, remain within the HZ for at least 10^6 years. Image Credit: Eberle et al. (2011) .

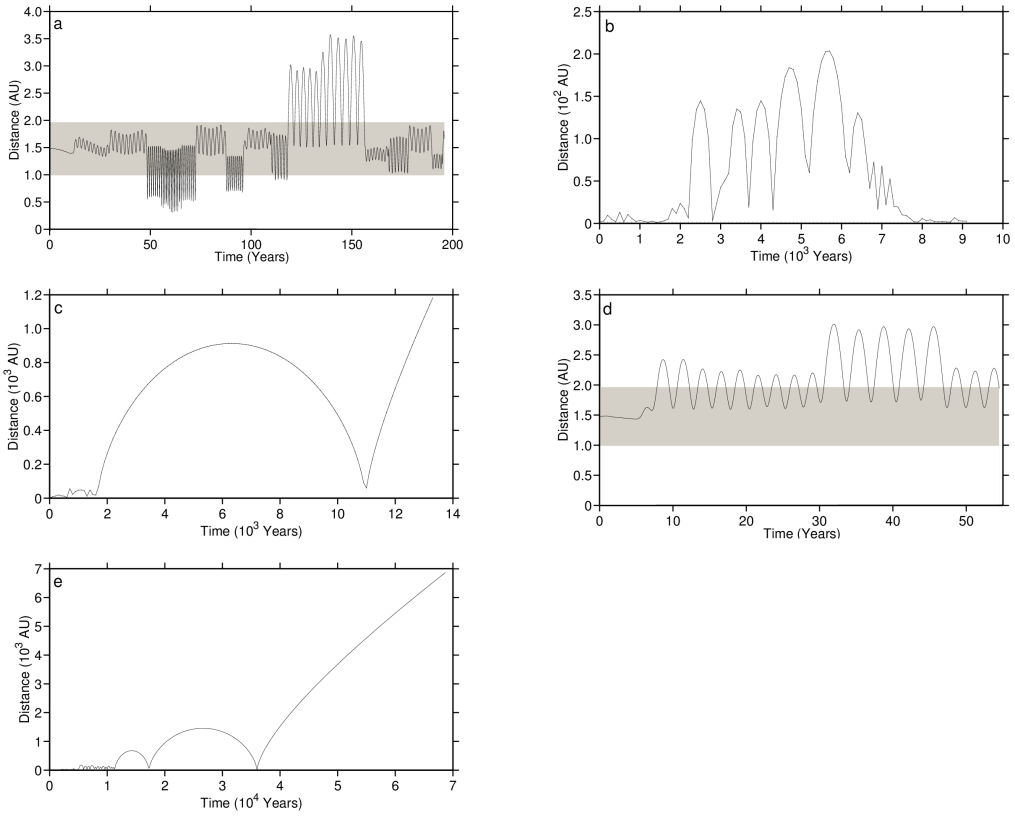

Figure 7.3. Orbital stability simulations with HD 23079 b initially placed at periastron for Earth-mass planets placed at starting angles of 180°. The model simulations differ regarding the selected values for the orbital parameters a_p and e_p of the giant planet HD 23079 b. The respective value pairs (a_p, e_p) are: (1.503, 0.102), (1.596, 0.071), (1.596, 0.102), (1.596, 0.133), and (1.689, 0.102) for panel a, b, c, d, and e, respectively, with a_p in AU. The gray domains (only visible in panel a and d) depict HD 23079's stellar HZ. Note the vast differences in the extent of the x and y-axes. .

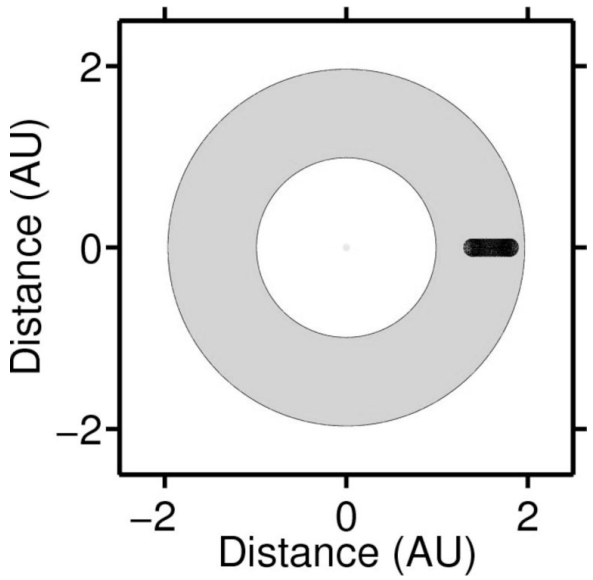

Figure 7.4. Orbital stability simulations with HD 23079 b initially placed at periastron with $a_p = 1.596$ AU, $e_p = 0.133$ and the Earth-mass planets placed at a starting angle of 0°. The Earth-mass planet remains within the HZ for at least 10^6 years. However, during that time it was captured by the giant planet and thus became a natural satellite (moon) of that planet, resulting in the small black area. Also note the absence of the "banana-shaped" area at L4 or L5. Image Credit: Eberle et al. (2011) .

CHAPTER 8

CONCLUSIONS AND FUTURE WORK

Mankind has sought to explain the motions of planets since written history began. To this end, theories have been developed and re-developed to explain the motion of the neighboring planets as well as establish natural laws which govern to some extent all known matter. This endeavor has taken millenia and is still not complete. With this dissertation I have produced scientific work to extend the knowledge of extrasolar planets through the perspective of orbital stability and habitability of such planets. Section 8.1 will describe in summary my contribution to this field. It will provide the essential details of what phenomena were discovered along with what predictions were made using the tools from chaos theory and theories of habitability. Section 8.2 will illustrate what I plan to accomplish to extend my dissertation and make my contribution to shape the paradigm of exoplanetary science.

8.1 Conclusions

This dissertation has described the steps taken to address problems in exoplanetary science concerning orbital stability theory, application, and habitability. In Chapter 3, I have developed a stability criterion for the CRTBP in the special case of the third mass, M_3, orbiting the more massive body, M_1. This stability criterion is based upon the method of Lyapunov exponents and uses the results of Lyapunov exponents to classify three different behaviors of motion namely bounded chaotic, unbounded chaotic, and stable orbits. I have shown that there does exist a critical value of the maximum Lyapunov exponent, $\log \lambda_{\max} = -0.82$, where systems that display

values higher than the critical value are classified as unbounded chaotic (Quarles et al. 2011). Values well below log $\lambda_{\max}$ describe systems that are stable against perturbations from the massive body, M_2. Systems with values near log $\lambda_{\max}$ are classified as bounded chaotic as they denote systems that have chaotic orbits which are induced by the perturbative mass, M_2, yet do not develop instabilities which lead to a close approach with one or body of the massive bodies, M_1 and M_2. These instabilities often involve a close encounter with the zero velocity contour. In addition, the maximum Lyapunov exponent has shown, as an indicator, the existence of a resonance plateau within the CRTBP. This dissertation has shown specifically a case of 3:1 resonance where $(\mu, \rho_0) = (0.30, 0.474)$.

In addition to developing a stability criterion with the maximum Lyapunov exponent, I have performed a study of resonances within the CRTBP. Studies of this type have only been performed previously for the cases where the mass ratio, μ, is akin to that of the Sun-Jupiter type systems. I have extended this analysis to include mass ratios up to $\mu = 0.5$. Through this analysis I have shown a number of resonances that can form in the CRTBP. Most notably I have shown that the 2:1 resonance occurs the most as a primary resonance and 3:1 occurs as a secondary resonance (Quarles et al. 2012c). Also I have used the concept of resonance overlap to indicate which resonances aid in destabilizing rather than stabilizing orbits. This study has demonstrated that the best mass ratio to look for resonant phenomena occurs when $\mu = 0.3$ because my survey of varying ρ_0 illustrates the greatest number of peaks in the maximum Lyapunov exponent.

By addressing the first two issues of a stability criteria along with resonance, I have been able to use my developed tools to probe the system of ν Octantis. Ramm et al. has proposed a Jupiter type planet to exist in this known binary and the proposal has met a great deal of controversy due to the putative planet residing

in a zone that is beyond previous calculated stability limits. I have furthered the hypothesis that the giant planet would exist in a retrograde orbit where the giant planet orbits in a direction opposite of the massive stars relative to the center of mass. In this study I have shown using the maximum Lyapunov exponent that a putative planet within ν Octantis would have a very small probability of existing for 10,000 yrs. However I also demonstrate that a substantial probability exists for the proposed planet to exist for at least 1,000 yrs in a retrograde configuration (Quarles et al. 2012a). To accomplish this I have performed simulations on a grid that covers the entire space of uncertainty in the observational measurements to develop a "landscape of survival." I also present an explanation for the occurrence of a proposed 5:2 resonance in the system that would account for a possible exoplanet in retrograde exhibiting bounded chaos.

In Chapters 6 and 7 I have addressed questions concerning habitability of 2 different systems Kepler-16 and HD 23079. In September 2011, Doyle et al. presented the discovery of the first circumbinary planet using the Kepler Space Telescope. This discovery has sparked a media frenzy concerning the analogous world of Tatooine from the *Star Wars* franchise. However open questions remained concerning the possibility of habitable worlds existing in the system of Kepler-16. I have investigated the possibility of Earth-mass planets existing inferior and superior to the discovered Saturnian planet within the range of the HZ and extended HZ (0.36 AU to 0.71(1.02) AU). I have revealed that Earth-mass planets inferior to the Saturnian mass in the HZ would be unstable due to perturbations from the Saturn-mass exoplanet, Kepler-16b. I also unveil that stable planetary-like (P-type) orbits exist starting at 0.95 AU from Kepler-16A in the extended HZ (Quarles et al. 2012b). However Earth-mass planets are not the only possibility for habitable worlds in the Kepler-16 system. I have also investigated the prospects of exomoons forming with the Saturnian exoplanet, being

captured by the Saturnian exoplanet, or existing as a Trojan-type exoplanet at the equilateral equilibrium positions L4 or L5 treating the binary stars as a point mass since the Saturnian orbit is almost circular. These three possibilities exist to provide for a habitable exomoon within the standard HZ and only further observations can determine which one (if any) are the most likely to occur.

Finally I have demonstrated through orbital stability that there does exist a possibility of Trojan-type planets and moons within the system of HD 23079. This case focuses on an already observed system of a Sun-like star that is slightly more massive than the Sun and a Jupiter-type planet that exists within the standard HZ. We show that Trojan-type planets that are at least an Earth mass can exist at either the L4 or L5 Lagrange points. I show specifically that Earth-mass planets inferior to the Jupiter-mass planet will exhibit perturbations that will force excursions from the standard HZ until ultimately being consumed by the giant planet or ejected from the system as a "free floating" planet (Eberle et al. 2011). In addition, we show conditions which the Earth-mass planet can be captured into a retrograde orbit around the Jupiter-mass planet for at least 10^6 yrs as an exomoon.

8.2 Future Work

This dissertation has provided results using the current numerical and theoretical tools of modern astronomy. Using these tools, I will extend the research concerning the system HD 23079. At the time of this writing (May 2012), I have already begun this endeavor by numerically determining stability limits for several different scenarios of possible habitable exomoons within HD 23079. I have considered a range of semimajor axes (a_p = 1.5030, 1.5495, 1.5960, 1.6425, 1.6890) and eccentricities (e_p = 0.0710, 0.0865, 0.1020, 0.1175, 0.1330) within the uncertainty parameters of HD 23079 b. Using this set of parameters, I am determining the stability limit of

possible satellite-like (S-type) exomoons within the HZ of HD 23079. A subset of the parameters (e_p, a_p) has been considered initially for 10^4 yrs by Dr. Eberle, I have begun simulations of the full set of parameters for a factor of 100 longer and utilized existing fitting formulas (Holman & Wiegert 1999; Domingos et al. 2006; Kaltenegger 2010) to estimate the stability limits for a mass ratio ($\mu = 0.00213$) commensurate with the HD 23079 system. This system has allowed us to establish an improved mathematical relationship for the stability limits as a function of the Hill radius, planet eccentricity, and moon eccentricity.

An additional goal is to transform the paradigm of habitability. Currently models of HZs are determined only for planetary systems with single stars. However, Raghavan et al. has previously shown that up to 33% of stars within our galaxy exist in binaries and an additional 7% exist in systems of higher stellar multiplicies. If these systems contain Sun-like stars, which has been shown for the case of Kepler-34 and Kepler-35, then there does exist a possibility of habitable planets and moons forming in such environments. My goal of future research is to generalize the model of habitability to include multi-stellar systems. This model will focus mainly upon binary stars as there are a substantial number of stellar candidates available for investigation. Parameters incorporated into such a model will include the semimajor axis, eccentricity, true anomaly, inclination, and other orbital elements of the binary. What makes scenarios of this type different is that a putative exoplanet/exomoon would experience a time-dependent source of photometric flux which necessitates the usage of the stellar orbital elements to account for what amount of time a planet would remain habitable. Also another layer of complexity exists in the possibilty of (de)stabilizing resonances that could form due to gravitational interactions between masses. My postdoctoral research will begin to unravel this unique and complex puzzle.

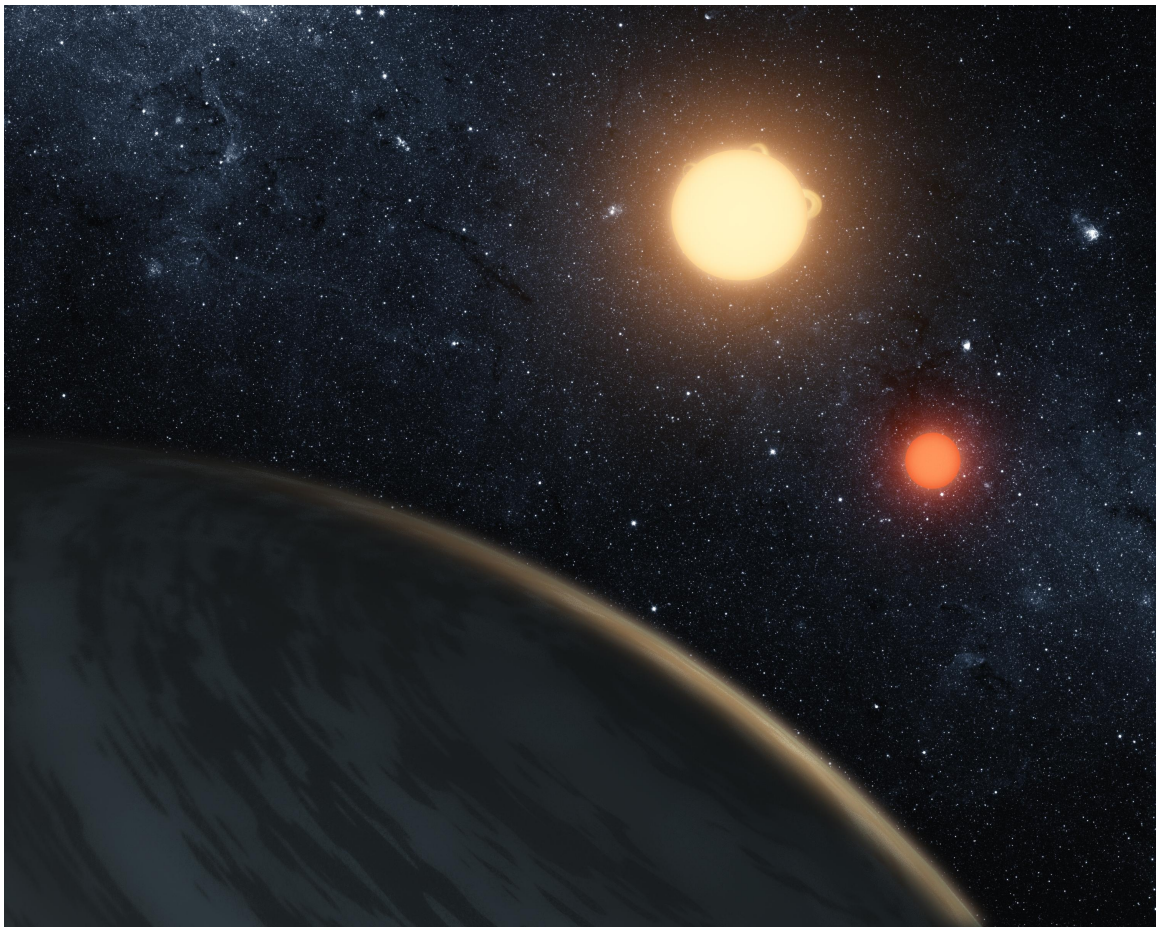

Figure 8.1. Artist's conception of Kepler-16b which has been definitely shown to orbit two stars. Image Credit: NASA/JPL-Caltech/T. Pyle.

Considering the almost daily discoveries being made by the Kepler space telescope the question "Is terrestrial life alone?" is most certainly beginning to be answered. Within the past year, Kepler has discovered more than a handful of planets with the HZs of their host stars. In addition many multi-planet systems have been discovered using techniques related to transit timing variations (TTV). The plethora of potential planetary candidates being considered by Kepler puts humankind in a unique position to begin from science fiction and now to science fact a trek among the stars.

APPENDIX A

DETERMINATION OF THE ORBITAL ELEMENTS FROM STATE VECTORS

The orbital elements $\{a, e, i, \Omega, \omega, f\}$ can be determined for any system relative to the central body which is the most massive body M_1 in the N body problem. Such elements are found via two different methods such as using Lagrange's Planetary equations of motion or through a transformation of the Cartesian state vectors from conventional integration methods. This appendix will discuss the latter rather than the former as this is the method that was most useful in determining the orbital elements for analysis within this dissertation.

A.1 Assumptions

Several assumptions need to be made to make the appropriate transformations to obtain the orbital elements. The first and foremost assumption is what is necessary to perform the transformation. The position state vector ($\mathbf{R}$), velocity state vector ($\mathbf{V}$), and gravitational parameter (GM_i) are the required known parameters at a given time where M_i is the mass of the central body. In terms of the general restricted three body problem (RTBP) the gravitational parameter is given as $GM\alpha$ where M represents the total mass and alpha is the larger of the two mass ratios (see Chapter 2). The value for G is chosen to be consistent with the value chosen for performing the simulations. For this dissertation, I have chosen $G = 4\pi$ with units of $M_\odot$, AU, and years. The coordinate system relative to the central body will be described by the Cartesian coordinates $\{x, y, z, \dot{x}, \dot{y}, \dot{z}\}$ as shown by Figure A.1 where the orbital plane, reference plane, and nodal intersection points have also been shown. For the sake of a more general perspective such as in the RTBP, this particular coordinates system could be constructed via translation (ie., $x_i = \xi_i - \xi_1$). Another assumption to be made is that the coordinates have appropriate units before the transformation. This follows from the assumption that the purpose of transforming state vectors to

orbital elements is to verify constants of motion in the 2 body problem or investigate osculating elements for the general N body problem.

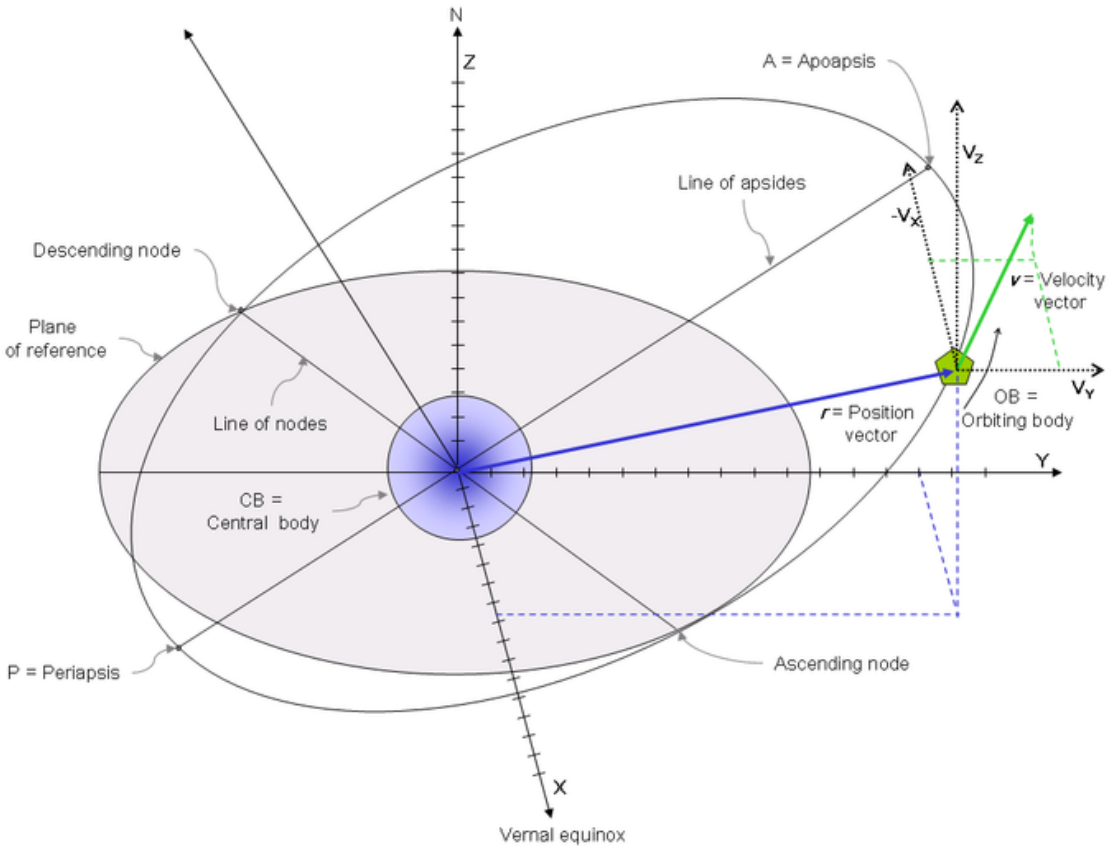

Figure A.1. Illustration of the determination of the orbital state vectors $\mathbf{R}, \mathbf{V}$ relative to a central body. Image Credit: Wikipedia.

The necessary assumptions are:

1. The only parameters to be known *a priori* are the orbital state vectors $(\mathbf{R}, \mathbf{V})$ and the appropriate gravitational parameter GM_i.
2. A coordinate system can be constructed such that the central body exists at the origin (ie., $x_i = \xi_i - \xi_1$).

3. A 2 body problem shall return the constants of motion of the system where a (N > 2) body problem will return the osculating elements.

A.2 Calculation

The orbital state vectors can be used to define a specific angular momentum vector **h** through the use of a cross product to find that $\mathbf{h} = \mathbf{R} \times \mathbf{V}$. Using this newly defined quantity I can determine directly the inclination of the orbit relative to the reference plane as

$$i = \frac{h_z}{|h|}. \tag{A.1}$$

Then a normal vector **n** can be determined through the cross product of the z-axis and the specific angular momentum to produce $\mathbf{n} = \hat{z} \times \mathbf{h}$ and scalar $n = |\mathbf{n}|$. The vector **n** will be utilized to explore all the possible cases to determine the ascending node, Ω. Using the normal vector, the following equations explore each different case as

$$\text{If } \mathbf{n} = \{0, 0, 0\} \qquad \text{then } \Omega = 0, \tag{A.2}$$

$$\text{If } \mathbf{n} > \{0, 0, 0\} \text{ and } n_y > 0 \qquad \text{then } \Omega = \cos^{-1}\left(\frac{n_x}{|n|}\right), \tag{A.3}$$

$$\text{If } \mathbf{n} > \{0, 0, 0\} \text{ and } n_y < 0 \qquad \text{then } \Omega = 2\pi - \cos^{-1}\left(\frac{n_x}{|n|}\right). \tag{A.4}$$

Next the orbital vectors, specific angular momentum, and the gravitational parameter can be used to determine the eccentricity vector whose magnitude produces the orbital element eccentricity. This is done by the using the following equations

$$\mathbf{e} = \frac{\mathbf{V} \times \mathbf{h}}{GM_1} - \frac{\mathbf{R}}{|\mathbf{R}|}, \tag{A.5}$$

$$e = |\mathbf{e}| \,. \tag{A.6}$$

Using the determined values for n and e I can introduce cases to determine the value of the argument of pericenter, ω. The following equations demonstrate the appropriate cases by

$$\text{If } n = 0 \text{ or } e = 0 \qquad \text{then } \omega = 0, \tag{A.7}$$

$$\text{If } n > 0 \text{ and } e_z > 0 \qquad \text{then } \omega = \frac{\mathbf{n} \cdot \mathbf{e}}{|\mathbf{n}|\,|\mathbf{e}|}, \tag{A.8}$$

$$\text{If } n > 0 \text{ and } e_z < 0 \qquad \text{then } \omega = 2\pi - \frac{\mathbf{n} \cdot \mathbf{e}}{|\mathbf{n}|\,|\mathbf{e}|}. \tag{A.9}$$

Using the orbital elements determined thus far the true anomaly f can be determined through different cases. The following equations demonstrate the appropriate cases by

$$\text{If } e = 0 \text{ and } (\mathbf{n} \times \mathbf{R})_z \geq 0 \qquad \text{then } f = \cos^{-1}\left(\frac{\mathbf{n} \cdot \mathbf{R}}{|\mathbf{n}|\,|\mathbf{R}|}\right), \tag{A.10}$$

$$\text{If } e = 0 \text{ and } (\mathbf{n} \times \mathbf{R})_z < 0 \qquad \text{then } f = 2\pi - \cos^{-1}\left(\frac{\mathbf{n} \cdot \mathbf{R}}{|\mathbf{n}|\,|\mathbf{R}|}\right), \tag{A.11}$$

$$\text{If } e > 0 \text{ and } \left(\frac{\mathbf{R} \cdot \mathbf{V}}{|\mathbf{R}|}\right) \geq 0 \qquad \text{then } f = \cos^{-1}\left(\frac{\mathbf{e} \cdot \mathbf{R}}{|\mathbf{e}|\,|\mathbf{R}|}\right), \tag{A.12}$$

$$\text{If } e > 0 \text{ and } \left(\frac{\mathbf{R} \cdot \mathbf{V}}{|\mathbf{R}|}\right) < 0 \qquad \text{then } f = 2\pi - \cos^{-1}\left(\frac{\mathbf{e} \cdot \mathbf{R}}{|\mathbf{e}|\,|\mathbf{R}|}\right). \tag{A.13}$$

Finally the semimajor axis can be determined through the relation

$$a = \frac{h^2}{GM_1(1-e^2)}, \tag{A.14}$$

where a negative value for semimajor axis would indicate that the orbital type is a hyperbola.

APPENDIX B

CALCULATION OF THE LYAPUNOV SPECTRUM

B.1 Circular Restricted Three-Body Problem

In the CRTBP I have used a rotating coordinate system which gives rise to Coriolis and centrifugal forces. The equations of motion of such a system are given by

$$\begin{aligned} \dot{x} &= u & \dot{u} &= 2v + x - \alpha\frac{x-\mu}{r_1^3} - \mu\frac{x+\alpha}{r_2^3}, \\ \dot{y} &= v & \dot{v} &= -2u + y - \alpha\frac{y}{r_1^3} - \mu\frac{y}{r_2^3}, \\ \dot{z} &= w & \dot{w} &= -\alpha\frac{z}{r_1^3} - \mu\frac{z}{r_2^3}, \end{aligned} \tag{B.1}$$

where

$$\begin{aligned} \mu &= \frac{m_2}{m_1+m_2} & r_1^2 &= (x-\mu)^2 + y^2 + z^2, \\ \alpha &= 1-\mu & r_2^2 &= (x+\alpha)^2 + y^2 + z^2. \end{aligned} \tag{B.2}$$

From these equations of motion I can define a set of 6 dimensional tangent vectors $\mathbf{x}_i$ and their derivatives $\dot{\mathbf{x}}_i$ where $i = 1, \ldots, 6$. This set of vectors are given as

$$\begin{aligned} \mathbf{x}_i &= \{x_i, y_i, z_i, u_i, v_i, w_i\}^T, \\ \dot{\mathbf{x}}_i &= \{u_i, v_i, w_i, \dot{u}_i, \dot{v}_i, \dot{w}_i\}^T. \end{aligned} \tag{B.3}$$

Also I can define a Jacobian matrix (see Section 2.2.3), $\mathbf{J}$, of the following form

$$\mathbf{J} = \begin{pmatrix} 0 & 0 & 0 & 1 & 0 & 0 \\ 0 & 0 & 0 & 0 & 1 & 0 \\ 0 & 0 & 0 & 0 & 0 & 1 \\ \frac{\partial \dot{u}}{\partial x} & \frac{\partial \dot{u}}{\partial y} & \frac{\partial \dot{u}}{\partial z} & 0 & 2 & 0 \\ \frac{\partial \dot{v}}{\partial x} & \frac{\partial \dot{v}}{\partial y} & \frac{\partial \dot{v}}{\partial z} & -2 & 0 & 0 \\ \frac{\partial \dot{w}}{\partial x} & \frac{\partial \dot{w}}{\partial y} & \frac{\partial \dot{w}}{\partial z} & 0 & 0 & 0 \end{pmatrix}. \tag{B.4}$$

B.2 Wolf method

Wolf et al. (1985) has established a method to determine the Lyapunov spectrum and here I will apply this to the CRTBP. The Wolf algorithm consists of three basic steps. The first step is to initialize a state vector of 6 elements with initial conditions. Then, the tangent vectors need to be initialized to some value. It has become convention to have all the tangent vectors to be unit vectors for simplicity. This means that the elements $\{x_1,\ y_2,\ z_3,\ u_4,\ v_5,\ w_6\} = 1$ and all other elements will equal 0.

The next step is to implement a loop in time that will use a standard integrator (Runge-Kutta, Gragg-Burlish-Stoer, etc.) to determine how the vectors (state & tangent) will change within a time step. This will continue for a arbitrary number of steps so that the tangent vectors can orient themselves along the flow. When this has been accomplished, the final step is to perform the Gram-Schmidt Renormalization (GSR) to orthogonalize the tangent space (see below). Thereafter, I can take the logarithm of the length of each tangent vector to obtain the Lyapunov exponents and continue the loop for the next time interval.

B.3 GSR & the Lyapunov Exponents

I use the first tangent vector, $\mathbf{x}_1$, to define a basis vector for the GSR process. The first step is to normalize this vector. I will denote vectors with $'$ to be the new orthonormal set of tangent vectors. The transformation to obtain these vectors is given by the following

$$\begin{aligned}
\mathbf{x}_1^{'} &= \frac{\mathbf{x}_1}{\|\mathbf{x}_1\|}, \\
\mathbf{x}_2^{'} &= \frac{\mathbf{x}_2 - \left\langle \mathbf{x}_2,\, \mathbf{x}_1^{'} \right\rangle \mathbf{x}_1^{'}}{\left\| \mathbf{x}_2 - \left\langle \mathbf{x}_2,\, \mathbf{x}_1^{'} \right\rangle \right\|}, \\
&\vdots \\
\mathbf{x}_6^{'} &= \frac{\mathbf{x}_6 - \left\langle \mathbf{x}_6,\, \mathbf{x}_5^{'} \right\rangle \mathbf{x}_5^{'} - \ldots - \left\langle \mathbf{x}_6,\, \mathbf{x}_1^{'} \right\rangle \mathbf{x}_1^{'}}{\left\| \mathbf{x}_6 - \left\langle \mathbf{x}_6,\, \mathbf{x}_5^{'} \right\rangle \mathbf{x}_5^{'} - \ldots - \left\langle \mathbf{x}_6,\, \mathbf{x}_1^{'} \right\rangle \mathbf{x}_1^{'} \right\|}.
\end{aligned} \tag{B.5}$$

From the new set of tangent vectors, the Lyapunov exponents can be calculated directly by using the lengths of each vector using this expression

$$\lambda_i = \frac{1}{\tau} \left[\lambda_{i-1} + \log \left\| \mathbf{x}_i - \sum_{j=1}^{i} \left\langle \mathbf{x}_i,\, \mathbf{x}_{j-1}^{'} \right\rangle \mathbf{x}_{j-1}^{'} \right\| \right] \tag{B.6}$$

where $\lambda_o = \mathbf{x}_o^{'} = 0$.

BIBLIOGRAPHY

Aarseth, S. J. 2003, Gravitational N-Body Simulations, ed. Aarseth, S. J.

Allende Prieto, C., & Lambert, D. L. 1999, *A&A* , 352, 555

Anderson, D. R., Hellier, C., Gillon, M., et al. 2010, *ApJ* , 709, 159

Asghari, N., Broeg, C., Carone, L., et al. 2004, *A&A* , 426, 353

Aughton, P. 2008, The Story of Astronomy (Quercus)

Baker, G. L., & Gollub, J. P. 1990, Chaotic dynamics. an introduction

Barnes, J., & Hut, P. 1986, *Nature* , 324, 446

Barnes, J. W., & O'Brien, D. P. 2002, *ApJ* , 575, 1087

Barnes, R., & Greenberg, R. 2008, in IAU Symposium, Vol. 249, IAU Symposium, ed. Y.-S. Sun, S. Ferraz-Mello, & J.-L. Zhou, 469–478

Barnes, R., Jackson, B., Greenberg, R., & Raymond, S. N. 2009, *ApJL* , 700, L30

Batalha, N. M., Borucki, W. J., Bryson, S. T., et al. 2011, *ApJ* , 729, 27

Benettin, G., Galgani, L., Giorgilli, A., & Strelcyn, J.-M. 1980, Meccanica, 15, 9

Beuermann, K., Hessman, F. V., Dreizler, S., et al. 2010, *A&A* , 521, L60

Beuermann, K., Buhlmann, J., Diese, J., et al. 2011, *A&A* , 526, A53

Bombardelli, C., & Peláez, J. 2011, Celestial Mechanics and Dynamical Astronomy, 109, 13

Bonavita, M., & Desidera, S. 2007, *A&A* , 468, 721

Butler, R. P., Wright, J. T., Marcy, G. W., et al. 2006, *ApJ* , 646, 505

Campbell, B., Walker, G. A. H., & Yang, S. 1988, ApJ, 331, 902

Canup, R. M., & Ward, W. R. 2006, *Nature* , 441, 834

Catanzarite, J., Shao, M., Tanner, A., Unwin, S., & Yu, J. 2006, *PASP* , 118, 1319

Charbonneau, D., Brown, T. M., Latham, D. W., & Mayor, M. 2000, ApJL, 529, L45

Cockell, C. S., Léger, A., Fridlund, M., et al. 2009, Astrobiology, 9, 1

Cooley, J. W., & Tukey, J. W. 1965, Mathematics of Computation, 19, pp. 297

Correia, A. C. M., Udry, S., Mayor, M., et al. 2009, *A&A* , 496, 521

Cuntz, M., Eberle, J., & Musielak, Z. E. 2007, *ApJL* , 669, L105

Cuntz, M., Roy, D., & Musielak, Z. E. 2009, *ApJL* , 706, L178

Cuntz, M., von Bloh, W., Bounama, C., & Franck, S. 2003, Icarus, 162, 214

Curiel, S., Cantó, J., Georgiev, L., Chávez, C. E., & Poveda, A. 2011, A&A, 525, A78

David, E.-M., Quintana, E. V., Fatuzzo, M., & Adams, F. C. 2003, *PASP* , 115, 825

Diacu, F. 1996, The Mathematical Intelligencer, 18, 66, 10.1007/BF03024313

Dole, S. H. 1964, Habitable planets for man

Domingos, R. C., Winter, O. C., & Yokoyama, T. 2006, MNRAS, 373, 1227

Donnison, J. R. 2010, *MNRAS* , 406, 1918

Doyle, L. R., Carter, J. A., Fabrycky, D. C., et al. 2011, Science, 333, 1602

Dressing, C. D., Spiegel, D. S., Scharf, C. A., Menou, K., & Raymond, S. N. 2010, *ApJ* , 721, 1295

Drilling, J. S., & Landolt, A. U. 2000, Normal Stars, ed. A. N. Cox, 381

Duquennoy, A., & Mayor, M. 1991, *A&A* , 248, 485

Dvorak, R. 1984, Celestial Mechanics, 34, 369

—. 1986, *A&A* , 167, 379

Dvorak, R., & Karch, M. 1988, Sterne und Weltraum, 27, 350

Dvorak, R., Pilat-Lohinger, E., Schwarz, R., & Freistetter, F. 2004, *A&A* , 426, L37

Dvorak, R., Schwarz, R., Süli, Á., & Kotoulas, T. 2007, *MNRAS* , 382, 1324

Eberle, J., & Cuntz, M. 2010a, *ApJL* , 721, L168

—. 2010b, *A&A* , 514, A19

Eberle, J., Cuntz, M., & Musielak, Z. E. 2008, *A&A* , 489, 1329

Eberle, J., Cuntz, M., Quarles, B., & Musielak, Z. E. 2011, International Journal of Astrobiology, 10, 325

Eberle, W. J. 2010, PhD thesis, University of Texas at Arlington, Arlington, TX

Eggenberger, A., & Udry, S. 2007, Planets in Binary Star Systems, ed. N. Haghighipour, Astrophysics and Space Science Library (Springer)

Eggenberger, A., & Udry, S. 2010, in Astrophysics and Space Science Library, Vol. 366, Astrophysics and Space Science Library, ed. N. Haghighipour, 19

Eggenberger, A., Udry, S., & Mayor, M. 2004, *A&A* , 417, 353

ESA. 1997, VizieR Online Data Catalog, 1239, 0

Fatuzzo, M., Adams, F. C., Gauvin, R., & Proszkow, E. M. 2006, *PASP* , 118, 1510

Ferraz-Mello, S. 1994, *AJ* , 108, 2330

Ferraz-Mello, S., & Dvorak, R. 1987, *A&A* , 179, 304

Fischer, D. A., Marcy, G. W., Butler, R. P., Laughlin, G., & Vogt, S. S. 2002, *ApJ* , 564, 1028

Forget, F., & Pierrehumbert, R. T. 1997, Science, 278, 1273

Fouchard, M., Lega, E., Froeschlé, C., & Froeschlé, C. 2002, Celestial Mechanics and Dynamical Astronomy, 83, 205

Fourier, J. B. J. 1822, Theorie analytique de la chaleur [microform] / par M. Fourier (F. Didot, Paris :), xxii, 639 p., [2] leaves of plates :

Frigo, M., & Johnson, S. G. 1998, in Proc. 1998 IEEE Intl. Conf. Acoustics Speech and Signal Processing, Vol. 3 (IEEE), 1381–1384

Frigo, M., & Johnson, S. G. 2005, Proceedings of the IEEE, 93, 216, special issue on "Program Generation, Optimization, and Platform Adaptation"

Froeschle, C. 1984, Celestial Mechanics, 34, 95

Froeschlé, C., & Lega, E. 2000, Celestial Mechanics and Dynamical Astronomy, 78, 167

Froeschlé, C., Lega, E., & Gonczi, R. 1997, Celestial Mechanics and Dynamical Astronomy, 67, 41

Funk, B., Schwarz, R., Pilat-Lohinger, E., Süli, Á., & Dvorak, R. 2009, *Planetary and Space Science* , 57, 434

Garcia, A. L. 2000, Numerical methods for physics

Gehman, C. S., Adams, F. C., & Laughlin, G. 1996, *PASP* , 108, 1018

Gonczi, R., & Froeschle, C. 1981, Celestial Mechanics, 25, 271

Goździewski, K. 2002, *A&A* , 393, 997

Gray, R. O., Corbally, C. J., Garrison, R. F., et al. 2006, *AJ* , 132, 161

Grazier, K. R., Newman, W. I., Varadi, F., Goldstein, D. J., & Kaula, W. M. 1996, in Bulletin of the American Astronomical Society, Vol. 28, AAS/Division of Dynamical Astronomy Meeting #27, 1181

Hadjidemetriou, J. D. 1993, Celestial Mechanics and Dynamical Astronomy, 56, 201

Haghighipour, N., Couetdic, J., Varadi, F., & Moore, W. B. 2003, *ApJ* , 596, 1332

Halevy, I., Pierrehumbert, R. T., & Schrag, D. P. 2009, Journal of Geophysical Research (Atmospheres), 114, 18112

Heideman, M., Johnson, D., & Burrus, C. 1984, ASSP Magazine, IEEE, 1, 14

Hilborn, R. 1994, Chaos and Nonlinear Dynamics: An Introduction for Scientists and Engineers (Oxford University Press)

Holman, M. J., & Wiegert, P. A. 1999, AJ, 117, 621

Houk, N., & Cowley, A. P. 1975, University of Michigan Catalogue of two-dimensional spectral types for the HD stars. Volume I.

Howard, A. W., Marcy, G. W., Johnson, J. A., et al. 2010, Science, 330, 653

Huang, S.-S. 1960, Scientific American, 202, 55

Jacob, W. S. 1855, MNRAS, 15, 228

Jefferys, W. H. 1974, *AJ* , 79, 710

Jefferys, W. H., & Yi, Z.-H. 1983, Celestial Mechanics, 30, 85

Ji, J., Kinoshita, H., Liu, L., & Li, G. 2003, *ApJL* , 585, L139

Jones, B. W., & Sleep, P. N. 2010, *MNRAS* , 407, 1259

Jones, B. W., Sleep, P. N., & Chambers, J. E. 2001, *A&A* , 366, 254

Jones, B. W., Sleep, P. N., & Underwood, D. R. 2006, *ApJ* , 649, 1010

Jones, B. W., Underwood, D. R., & Sleep, P. N. 2005, *ApJ* , 622, 1091

Kaltenegger, L. 2010, ApJL, 712, L125

Kasting, J. F., Whitmire, D. P., & Reynolds, R. T. 1993, Icarus, 101, 108

King, H. C. 1955, The history of the telescope

Kipping, D. M. 2011, The Transits of Extrasolar Planets with Moons (Springer)

Kipping, D. M., Fossey, S. J., & Campanella, G. 2009, MNRAS, 400, 398

Kley, W., D'Angelo, G., & Henning, T. 2001, ApJ, 547, 457

Lada, C. J. 2006, *ApJL* , 640, L63

Laskar, J., Froeschlé, C., & Celletti, A. 1992, Physica D Nonlinear Phenomena, 56, 253

Laskar, J., Joutel, F., & Robutel, P. 1993, *Nature* , 361, 615

Laskar, J., & Robutel, P. 1993a, *Nature* , 361, 608

—. 1993b, *Nature* , 361, 608

Lecar, M., Franklin, F., & Murison, M. 1992, *AJ* , 104, 1230

Lee, J. W., Kim, S.-L., Kim, C.-H., et al. 2009, *AJ* , 137, 3181

Lee, M. H., Butler, R. P., Fischer, D. A., Marcy, G. W., & Vogt, S. S. 2006, *ApJ* , 641, 1178

Lega, E., & Froeschlé, C. 2001, Celestial Mechanics and Dynamical Astronomy, 81, 129

Lin, D. N. C., Bodenheimer, P., & Richardson, D. C. 1996, *Nature* , 380, 606

Lissauer, J. J. 1993, *Ann. Rev. Astron. Astrophys.* , 31, 129

—. 1999, Nature, 398, 659

Lissauer, J. J., Barnes, J. W., & Chambers, J. E. 2011, in American Astronomical Society Meeting Abstracts, Vol. 218, 402.08

Lohinger, E., & Froeschle, C. 1993, Celestial Mechanics and Dynamical Astronomy, 57, 369

Lohinger, E., Froeschle, C., & Dvorak, R. 1993, Celestial Mechanics and Dynamical Astronomy, 56, 315

Lucas, P. W., & Roche, P. F. 2000, *MNRAS* , 314, 858

Luzum, B., Capitaine, N., Fienga, A., et al. 2011, Celestial Mechanics and Dynamical Astronomy, 110, 293, 10.1007/s10569-011-9352-4

Lyapunov, A. 1907, Annales de la facultè des sciences de Toulouse, 2:9, 203

Marcy, G. W., & Butler, R. P. 2000, *PASP* , 112, 137

Marcy, G. W., Butler, R. P., Fischer, D., et al. 2001, *ApJ* , 556, 296

Marcy, G. W., Butler, R. P., Fischer, D. A., et al. 2002, *ApJ* , 581, 1375

Mardling, R. A. 2008, in IAU Symposium, Vol. 246, IAU Symposium, ed. E. Vesperini, M. Giersz, & A. Sills, 199–208

MATLAB. 2011, version 7.12.0.635 (R2011a) (Natick, Massachusetts: The MathWorks Inc.)

Mayor, M., & Queloz, D. 1995, Nature, 378, 355

Menou, K., & Tabachnik, S. 2003, *ApJ* , 583, 473

Meyer, S. L. 1975, Data analysis for scientists and engineers

Milani, A., & Nobili, A. M. 1992, *Nature* , 357, 569

Mischna, M. A., Kasting, J. F., Pavlov, A., & Freedman, R. 2000, Icarus, 145, 546

Morais, M. H. M., & Correia, A. C. M. 2012, *MNRAS* , 419, 3447

Morbidelli, A., & Nesvorny, D. 1999, Icarus, 139, 295

Mudryk, L. R., & Wu, Y. 2006, *ApJ* , 639, 423

Mugrauer, M., & Neuhäuser, R. 2009, *A&A* , 494, 373

Murray, C. D., & Dermott, S. F. 1999, Solar system dynamics, ed. Murray, C. D. & Dermott, S. F.

Murray, N., & Holman, M. 2001, *Nature* , 410, 773

Musielak, Z. E., Cuntz, M., Marshall, E. A., & Stuit, T. D. 2005, *A&A* , 434, 355

Musielak, Z. E., Cuntz, M., & Roy, D. 2010, Highlights of Astronomy, 15, 680

Musielak, Z. E., & Musielak, D. E. 2009, International Journal of Bifurcation and Chaos, 19, 2823

Nesvorný, D., Ferraz-Mello, S., Holman, M., & Morbidelli, A. 2002, Asteroids III, 379

Nesvorný, D., & Morbidelli, A. 1998, *AJ* , 116, 3029

Noble, M., Musielak, Z. E., & Cuntz, M. 2002, *ApJ* , 572, 1024

North, J. 1995, The Norton history of astronomy and cosmology.

Novak, G. S., Lai, D., & Lin, D. N. C. 2003, in Astronomical Society of the Pacific Conference Series, Vol. 294, Scientific Frontiers in Research on Extrasolar Planets, ed. D. Deming & S. Seager, 177–180

Ozorio de Almeida, A. M. 1990, Hamiltonian Systems

Patience, J., White, R. J., Ghez, A. M., et al. 2002, ApJ, 581, 654

Pilat-Lohinger, E., & Dvorak, R. 2002, Celestial Mechanics and Dynamical Astronomy, 82, 143

Press, W. H., Flannery, B. P., & Teukolsky, S. A. 1986, Numerical recipes. The art of scientific computing

Ptolemy, C. 147, Almagest

Qian, S.-B., Liao, W.-P., Zhu, L.-Y., & Dai, Z.-B. 2010, *ApJL* , 708, L66

Quarles, B., Cuntz, M., & Musielak, Z. E. 2012a, *MNRAS* , 421, 2930

Quarles, B., Eberle, J., Musielak, Z. E., & Cuntz, M. 2011, *A&A* , 533, A2

Quarles, B., Musielak, Z. E., & Cuntz, M. 2012b, *ApJ* , 750, 14

—. 2012c, Astron. Nachr., 333, 551

Queloz, D., Anderson, D., Collier Cameron, A., et al. 2010, *A&A* , 517, L1

Quintana, E. V., Lissauer, J. J., Chambers, J. E., & Duncan, M. J. 2002, ApJ, 576, 982

Rabl, G., & Dvorak, R. 1988, *A&A* , 191, 385

Raghavan, D., Henry, T. J., Mason, B. D., et al. 2006, *ApJ* , 646, 523

Raghavan, D., McAlister, H. A., Henry, T. J., et al. 2010, *ApJS* , 190, 1

Ramm, D. J., Pourbaix, D., Hearnshaw, J. B., & Komonjinda, S. 2009, *MNRAS* , 394, 1695

Ribas, I., Solano, E., Masana, E., & Giménez, A. 2003, *A&A* , 411, L501

Roy, A. E. 2005, Orbital motion

Sato, B., Ando, H., Kambe, E., et al. 2003, *ApJL* , 597, L157

Schwarz, R., Dvorak, R., Süli, Á., & Érdi, B. 2007, *A&A* , 474, 1023

Schwarz, R., Gyergyovits, M., & Dvorak, R. 2004, Celestial Mechanics and Dynamical Astronomy, 90, 139

See, T. J. J. 1896, AJ, 16, 17

Selsis, F., Kasting, J. F., Levrard, B., et al. 2007, *A&A* , 476, 1373

Sherrill, T. J. 1999, Journal for the History of Astronomy, 30, 25

Shklovskii, I. S., & Sagan, C. 1966, Intelligent life in the universe

Slawson, R. W., Prša, A., Welsh, W. F., et al. 2011, *AJ* , 142, 160

Slonina, M., Gozdziewski, K., Migaszewski, C., & Rozenkiewicz, A. 2012, ArXiv e-prints

Smith, R. H., & Szebehely, V. 1993, Celestial Mechanics and Dynamical Astronomy, 56, 409

Szebehely, V. 1967, Theory of orbits. The restricted problem of three bodies, ed. Szebehely, V.

Szenkovits, F., & Makó, Z. 2008, Celestial Mechanics and Dynamical Astronomy, 101, 273

Tantardini, M., Fantino, E., Ren, Y., et al. 2010, Celestial Mechanics and Dynamical Astronomy, 108, 215

Tinney, C. G., Butler, R. P., Marcy, G. W., et al. 2002, *ApJ* , 571, 528

Touma, J., & Wisdom, J. 1993, Science, 259, 1294

Tsonis, A. A. 1992, Chaos: from theory to applications (New York: Plenum Press), 8–29,33–43

Udry, S., Bonfils, X., Delfosse, X., et al. 2007, *A&A* , 469, L43

Underwood, D. R., Jones, B. W., & Sleep, P. N. 2003, International Journal of Astrobiology, 2, 289

van de Kamp, P. 1969, AJ, 74, 757

van Leeuwen, F. 2007, *A&A* , 474, 653

Vela-Arevalo, L. V., & Marsden, J. E. 2004, Classical and Quantum Gravity, 21, 351

Vogt, S. S., Butler, R. P., Rivera, E. J., et al. 2010, *ApJ* , 723, 954

von Bloh, W., Cuntz, M., Franck, S., & Bounama, C. 2003, Astrobiology, 3, 681

Welsh, W. F., Orosz, J. A., Carter, J. A., et al. 2012, Nature, 481, 475

Williams, D. M., & Kasting, J. F. 1997, Icarus, 129, 254

Williams, D. M., & Pollard, D. 2002, International Journal of Astrobiology, 1, 61

Williams, I. P. 2003, Celestial Mechanics and Dynamical Astronomy, 87, 13, 10.1023/A:1026137401540

Winn, J. N., Johnson, J. A., Albrecht, S., et al. 2009, *ApJL* , 703, L99

Wisdom, J., & Holman, M. 1992, *AJ* , 104, 2022

Wolf, A., Swift, J. B., Swinney, H. L., & Vastano, J. A. 1985, Physica D Nonlinear Phenomena, 16, 285

Wolszczan, A., & Frail, D. A. 1992, *Nature* , 355, 145

Yeager, K. E., Eberle, J., & Cuntz, M. 2011, International Journal of Astrobiology, 10, 1

Yoshida, H. 1990, Physics Letters A, 150, 262

BIOGRAPHICAL STATEMENT

Billy Lee Quarles graduated from Whitesboro High School in May 2002 and began studying at Texas Christian University (TCU) in August 2002. Billy pursued a B.S. in Astronomy & Physics. During his senior year, Billy showcased his undergraduate research into the ultraviolet conditions of the early Earth at the Student Research Symposium held annually at TCU. He received the Best Undergraduate Poster award for his distinguished research entitled "Ultraviolet Radiation on the Early Earth." Thereafter Billy received his B.S. degree in May 2006.

Having just recently married his wife, Teresa, Billy began his graduate career in August 2006 at Stephen F. Austin State University. While at SFA Billy became involved in several research projects. First of which, he aided in the production of a computational model of asteroids which led him to expand into the realm of extrasolar planets. His graduate research involved numerically characterizing the orbits of extrasolar planets in TrES-1, TrES-2, and HD 189733b. In addition to his theoretical work, he performed photometric observations of these planets using the 41" telescope at the SFA Observatory to compare to his numerical results. Also, Billy developed a method to generate a photometric light curve using 3D rendering software called POV-Ray. Along with his graduate research, Billy aided in conducting a light pollution survey of Nacogdoches county. He produced a professional contour map of sky brightness to demonstrate the extent of where the sky was brightest relative to the city. Billy defended his Masters thesis to receive a M.S. in Physics in May 2008.

Continuing his graduate career, Billy began studies at the University of Texas at Arlington in August 2008. Since 2008, he has engaged in research involved in fur-

thering the development of celestial mechanics and astrobiology within the realm of extrasolar planets. His main focus of research includes the special case of binary stars with planets, as well as possible moons in single star-planet systems. Billy has authored 5 scientific papers that have been peer-reviewed and published in top journals such as the *Astrophysical Journal, International Journal of Astrobiology, Monthly Notices of the Royal Astronomical Society, Astronomische Nachrichten/Astronomical Notes,* and *Astronomy & Astrophysics*. In April 2012, Billy was presented with the Outstanding Physics Major award for his academic and research achievement.

After graduation, Billy would like to work at NASA Ames Research Center innovating the current theories involving the habitability of multi-stellar environments.